

Lamb-Dicke Spectroscopy of the $^1S_0 \rightarrow ^3P_0$ Transition in ^{24}Mg and Precise Determination of the Magic Wavelength



Von der QUEST-Leibniz-Forschungsschule der
Gottfried Wilhelm Leibniz Universität Hannover

zur Erlangung des Grades

Doktor der Naturwissenschaften
- Dr. rer. nat. -

genehmigte Dissertation

von

André Philipp Kulosa

geboren am 26.09.1984, in Alfeld/Leine

2015

Referent: Prof. Dr. Ernst M. Rasel
Institut für Quantenoptik, Leibniz Universität Hannover

Korreferent: Prof. Dr. Wolfgang Ertmer
Institut für Quantenoptik, Leibniz Universität Hannover

Korreferent: Prof. Dr. Kurt Gibble
Department of Physics, The Pennsylvania State University

Tag der Promotion: 19. Oktober, 2015

*Für meine Eltern,
Waltraut und Dieter*

Abstract

State-of-the-art optical clocks based on neutral atoms have already surpassed the world's best microwave atomic clocks in both accuracy and stability, paving the way to high-precision measurements of elementary aspects of nature, like the search for the drift of fundamental constants or the application of relativistic geodesy.

These clocks operate with ensembles trapped in an optical lattice. Normally, high-power trapping laser fields induce a large AC Stark shift on the clock's transition frequency, as the clock states have different polarizabilities. A key feature of lattice clocks is the *magic wavelength*, for which the atomic polarizabilities of the clock states are equal, therefore compensating a differential frequency shift on the clock transition.

In the periodic potential of the optical lattice, the energy spectrum of motional states features a band structure, analogous to electrons in a crystalline structure well-known from solid state physics. Within this band structure, atoms can tunnel between adjacent lattice sites. As a consequence from tunneling motion, the clock transition experiences a frequency shift and a broadening, which becomes pronounced in the *shallow lattice regime*.

This work presents the first demonstration of a ^{24}Mg optical lattice clock including the precise determination of the frequency of the clock transition, its magic wavelength and its second-order Zeeman shift. Furthermore, the effect of tunneling in an optical lattice for magnesium has been extensively studied via *optical spectroscopy of Bloch bands* and substantiated with theoretical models, that were initially developed for a strontium optical lattice clock.

Measuring lattice light induced frequency shifts of the clock transition for various lattice wavelengths and intensities, yielded a value of the magic wavelength of the $^1S_0 \rightarrow ^3P_0$ clock transition in ^{24}Mg of 468.463(207) nm. This value is in well agreement with a recent theoretical calculation of 468.45(23) nm, using a refined atomic structure model. The experimental value for the magic wavelength was independently verified with optical spectroscopy of Bloch bands carried out on the clock transition. Here, the AC Stark modified band structure is directly probed by a single frequency scan of the carrier resonance, featuring an asymmetric line shape, that is strongly dependent on the lattice wavelength. This technique demonstrates a novel method for the determination of the magic wavelength and could also be applied to other atomic species.

In bosonic isotopes of alkaline earth(-like) elements, like ^{24}Mg , optical dipole excitation of the spin-forbidden $^1S_0 \rightarrow ^3P_0$ clock transition can be enhanced, e.g. by applying an external magnetic field. While these bosons are insensitive to first-order Zeeman shifts, the second-order Zeeman effect displays a dominant contribution to the clock's error budget. In this thesis, the magnetic polarizability β is measured to be $-206.6(2.0)$ MHz/T², consistent with a theoretical calculation, and the clock transition frequency was found to be 655 058 646 691(101) kHz.

Key words: Optical atomic clocks, Magic wavelength, Optical spectroscopy of Bloch bands

Zusammenfassung

Hochmoderne, optische Uhren basierend auf Neutralatomen, haben die weltbesten Mikrowellenuhren hinsichtlich ihrer Genauigkeit und Stabilität bereits übertroffen und eröffnen damit die Möglichkeit, Grundaspekte der Natur in Hochpräzisionsexperimenten zu testen. Als Beispiele seien hier die Untersuchung der Drift von fundamentalen Naturkonstanten, sowie die Anwendung der relativistischen Geodäsie genannt.

Diese Uhren arbeiten mit Ensembles von Atomen, die in einem optischen Gitter gespeichert werden. Normalerweise induziert die dafür verwendete Laserstrahlung eine AC-Stark-Verschiebung in der Übergangsfrequenz des Atoms. Wird jedoch das optische Gitter bei der sogenannten *magischen Wellenlänge* betrieben, sind die atomaren Polarisierbarkeiten der beteiligten Uhrenzustände identisch und eine Frequenzverschiebung wird unterdrückt.

Im periodischen Potential eines optischen Gitters treten die Energien der Bewegungszustände in einer periodischen Bandstruktur auf, analog zu der Betrachtung des Elektrons in einer Kristallstruktur in der Festkörperphysik. Innerhalb dieser Bandstruktur können die Atome zwischen benachbarten Gitterplätzen tunneln. Diese Tunnelbewegung ruft eine Frequenzverschiebung sowie Verbreiterung des Uhrenübergangs hervor und tritt verstärkt im *Regime der flachen Gitter* auf.

Diese Arbeit beschreibt die erstmalige Demonstration einer optischen Gitteruhr mit ^{24}Mg . Im Rahmen dessen konnten die folgenden, atomaren Parameter präzise bestimmt werden: die Frequenz des Uhrenübergangs, sowie seine magische Wellenlänge und seine quadratische Zeeman-Verschiebung. Desweiteren wurden Tunneleffekte im optischen Gitter mit Hilfe von *optischer Spektroskopie der Blochbänder* untersucht und mit theoretischen Modellen untermauert.

Die magische Wellenlänge des $^1S_0 \rightarrow ^3P_0$ Uhrenübergangs in ^{24}Mg konnte zu 468.463(207) nm bestimmt werden und ist in guter Übereinstimmung mit einem kürzlich berechneten Wert von 468.45(23) nm. Eine unabhängige, experimentelle Bestätigung lieferte die optische Spektroskopie der Blochbänder der Uhrenzustände: die durch den AC-Stark-Effekt deformierte Bandstruktur äußert sich bei einer Spektroskopie des Trägerübergangs in einer Asymmetrie der Resonanzlinienform, die stark von der Gitterwellenlänge beeinflusst wird. Dieses Verfahren stellt eine neue Messmethode zur Bestimmung der magischen Wellenlänge dar und kann auch für andere, atomare Spezies eingesetzt werden.

Die optische Dipolanregung des doppelt verbotenen $^1S_0 \rightarrow ^3P_0$ Uhrenübergangs kann in bosonischen Isotopen, wie im Falle von ^{24}Mg , z.B. durch Anlegen eines externen Magnetfelds verstärkt werden. Obwohl Erdalkali-(ähnliche) Bosonen insensitive auf den linearen Zeeman-Effekt reagieren, liefert der quadratische Zeeman-Effekt einen dominanten Beitrag zum Unsicherheitsbudget der Uhr. In dieser Arbeit konnte die magnetische Polarisierbarkeit β zu $-206.6(2.0)\text{ MHz/T}^2$ bestimmt werden und ist konsistent mit theoretischen Berechnungen. Mit Kenntnis der Zeeman-Verschiebung wurde die Frequenz des Uhrenübergangs zu 655 058 646 691(101) kHz vermessen.

Schlagwörter: Optische Atomuhr, Magische Wellenlänge, Optische Spektroskopie der Blochbänder

CONTENTS

1	Introduction	1
2	Experimental setup	7
2.1	Vacuum apparatus	7
2.2	Magnetic fields	8
2.3	Detection of atoms	11
3	State preparation	15
3.1	Relevant level scheme of ^{24}Mg	15
3.2	Laser cooling of ^{24}Mg	17
3.2.1	The singlet-MOT at 285 nm	17
3.2.2	Optical transfer at 457 nm	19
3.2.3	The triplet-MOT at 383 nm	20
3.3	Optical trapping of ^{24}Mg	22
3.3.1	Continuous loading of an optical dipole trap at 1064 nm	23
3.3.2	Transfer to the optical lattice at 469 nm	24
3.4	Scheme for a bosonic clock with ^{24}Mg	25
3.4.1	Magnetic field enhanced spectroscopy	26
3.4.2	The clock laser at 458 nm	26
4	Theoretical discussion of Lamb-Dicke spectroscopy	29
4.1	Lamb-Dicke spectroscopy in harmonic confinement	33
4.1.1	Preparing the quantum mechanical tools	33
4.1.2	Atom-light interaction in harmonic confinement	35
4.1.3	Deduction of atomic temperature	40
4.2	Lamb-Dicke spectroscopy in a 1D optical lattice	40
4.2.1	The optical lattice potential	40
4.2.2	Excitation inhomogeneities I - The magic wavelength	42
4.2.3	Excitation inhomogeneities II - Atomic motion	44
4.3	Carrier spectroscopy and Bloch bands	48

4.3.1	Tunneling between adjacent lattice sites - The band structure	48
4.3.2	The effect of tunneling motion - Simulation of the carrier signal	50
4.3.3	Spectroscopy of Bloch bands close to the magic wavelength .	52
4.4	Conclusion	54
5	Lamb-Dicke spectroscopy of the $^1S_0 \rightarrow ^3P_0$ clock transition	57
5.1	Characterization of the optical lattice	57
5.2	Measurement of the magic wavelength for the clock transition . . .	60
5.3	Measurement of the 2nd order Zeeman shift	62
5.3.1	Measurement of the magnetic field dependence	63
5.3.2	Measurement of the clock transition frequency	63
5.4	Optical spectroscopy of Bloch bands	64
5.4.1	Spectroscopy in the shallow lattice regime	64
5.4.2	Spectroscopy of Bloch bands close to the magic wavelength .	69
5.5	Conclusion	72
6	Outlook	75
6.1	High-precision Lamb-Dicke spectroscopy	75
6.1.1	Increasing the lattice trap depth	76
6.1.2	Purification of the atomic ensemble	78
6.1.3	Towards an optical lattice clock with magnesium	79
6.2	Fermions vs. bosons	82
6.2.1	Challenges for fermionic isotopes	83
6.2.2	The fermionic ^{25}Mg	84
6.3	Prospects for optical spectroscopy of Bloch bands	85
A	Properties of a compact triplet-MOT	87
B	Fitting of the carrier line shape	91
C	Publications	93

Introduction

"But nobody measures anything to one part in 10^{17} . [...] The challenge is great and should occupy experimental physicists for some years."

Arthur L. Schawlow [1]

The development of atomic frequency standards

Being able to control the interaction of electro-magnetic radiation with matter in molecular spectroscopy, it was Isidor I. Rabi and co-workers who created the prerequisites for today's atomic clocks with their "Molecular Beam Resonance Method for Measuring Nuclear Magnetic Moments" in 1939 [2]. Only ten years later, Norman F. Ramsey, who was a former PhD student of Rabi, improved the beam resonance method by introducing two separated oscillatory fields for state interrogation, rather than a single field extending over the whole atomic distance of flight, thus enabling measurements with higher precision [3, 4]. Both, Rabi and Ramsey, have been awarded the Nobel prize in physics for their groundbreaking works in 1944 and 1989, respectively [5].

In 1955, Louis Essen and Jack V. L. Parry used Ramsey's method to interrogate the ground state hyperfine transition in cesium. They reported about the development of the world's first atomic frequency standard, being more accurate than any standard based on astronomical time [6]. In fact, these measurements were taken with an uncertainty better than 1×10^{-9} , representing the highest accurate measurement of a physical quantity so far. At that time, the second was defined as the fraction $1/86400$ of the mean solar day. Nevertheless, this definition

has been found to be dissatisfying as earth's rotation shows irregularities. During the 13th General Conference on Weights and Measures (GCPM¹) in 1967 [7], the second has been re-defined to be

"the duration of 9 192 631 770 periods of the radiation corresponding to the transition between the two hyperfine levels of the ground state of the ¹³³Cs atom",

referencing one of the fundamental units in physics to an object, ancient Greek philosophers already had considered to be "indivisible". Atoms are basic components of matter coming along in a rich diversity and -at the same time- can be kept extremely well under control in the world's laboratories.

As a consequence from the definition of the SI second, cesium clocks used for time-keeping had been established by national metrology institutions all over the world. With the invention of laser cooling [8, 9], existing Cs clocks based on a thermal beam of atoms were further improved in both uncertainty and instability. In *atomic fountain clocks*, a new type of interrogation geometry, laser-cooled atoms are launched onto a trajectory under the influence of gravity, thereby passing twice a microwave interrogation zone [10–12]. Today's best cesium clocks have reached statistical uncertainties close to 1×10^{-16} , which almost displays their fundamental limit [13–16].

From microwave to optical domain - A boost in stability

Atomic clocks are characterized by their instability and the uncertainty of their transition frequency. Instability is measured by the *Allan deviation*

$$\sigma_y(t) \sim \frac{\Delta\nu}{\nu_0} \frac{1}{S/N} \sqrt{\frac{T_c}{\tau}}. \quad (1.1)$$

Here, $\Delta\nu$ is the atomic transition linewidth, ν_0 is the unperturbed transition frequency, S/N is the signal-to-noise ratio, T_c is the clock's cycle time (i.e., the time required for atomic state preparation and determination of the line center) and τ is the total averaging time [10, 17]. The ratio $\nu_0/\Delta\nu$ is called the transition's quality factor Q or line- Q .

According to Eq. 1.1, the clock's instability could be further reduced, if transitions with higher frequencies ν_0 are used. Advancing into the optical frequency domain increases the transition frequency by four to five orders of magnitude and hence reduces the frequency instability by the same amount. Like for any other atomic clock, the measurement of optical frequencies needs to be referenced to the Cs atomic clock. However, this approach came together with an experimental challenge: microwave frequencies could easily be detected with RF electronics, but optical frequencies of a few 100 THz cannot.

¹*French*: Conférence générale des poids et mesures

Finally, the frequency of optical transitions had been determined by connecting the down-converted frequency of the optical oscillator with the up-converted microwave frequency of the Cs clock using optical frequency chains. In this way, Schnatz *et al.* demonstrated the first phase-coherent frequency measurement of an optical transition in the visible domain in 1996 at PTB (Physikalisch Technische Bundesanstalt), performed on the $^1S_0 \rightarrow ^3P_1$ intercombination line at 657 nm in laser-cooled ^{40}Ca [18]. In a comparable experiment, even frequency measurements in the ultraviolet regime had become accessible, like the spectroscopy of the $1S-2S$ transition at 121 nm in atomic hydrogen [19].

Operation of these phase-coherent frequency chains is a room-filling experiment, probably comparable to the early start of computers by Konrad Zuse or Alan M. Turing in the 1930s. If we have a look on the size of today's available desktop computers, the effort in measuring optical frequencies took the same remarkable improvement thanks to the invention of the *optical frequency comb*, a "ruler in frequency space" based on the Fourier spectrum of a mode-locked laser. This unique tool, allowing for direct optical frequency comparisons, had initially been proposed by Theodor W. Hänsch and co-workers [20, 21] and has been rewarded with the Nobel prize in physics in 2005, shared between John L. Hall, Theodor W. Hänsch and Roy J. Glauber [5]. As the early frequency combs featured an optical spectrum ranging from about $0.5\ \mu\text{m}$ to $1\ \mu\text{m}$ [22], a frequency comb spanning down to the ultraviolet domain was demonstrated in the same year of the Nobel prize award [23].

The commercial availability of optical frequency combs gave a real boost to the development of optical atomic clocks. The first optical clock to be reported was the $^{199}\text{Hg}^+$ ion clock at NIST (National Institute of Standards and Technology) in the group of D. J. Wineland [24]. Ions trapped in Paul or Penning traps [25] feature long storage times and therefore allow for the clock's Allan deviation to average down in equal measure. Furthermore, the trapping potential provided by the ion traps is in good approximation to the harmonic oscillator enabling a spatial confinement of the ions known as the *Lamb-Dicke regime* [26]. In this particular regime, clock spectroscopy can be performed being free of first-order Doppler shifts and photon recoil shifts, as the clock laser photon recoil is absorbed by the trapping potential. The energy of atomic motion in this trap is quantized by multiples of the trapping frequencies $\hbar\omega_{\text{Trap}}$ given by the harmonic potential [27], instead of the continuous energy spectrum absorbers exhibit in free-space. If the potential depth further satisfies the criterion, that the energy spacing between motional levels is larger than the natural linewidth of the clock transition, spectroscopy is carried out in the so-called *resolved sideband regime*, enabling active laser cooling to the zero-point energy of atomic motion [28].

However, the number of particles that can be trapped in an ion trap is limited to just a few tens of ions [29], hence limiting the available S/N ratio in Eq. 1.1. In optical clocks based on neutral atoms, ensembles composed of 10^3 to 10^4 particles

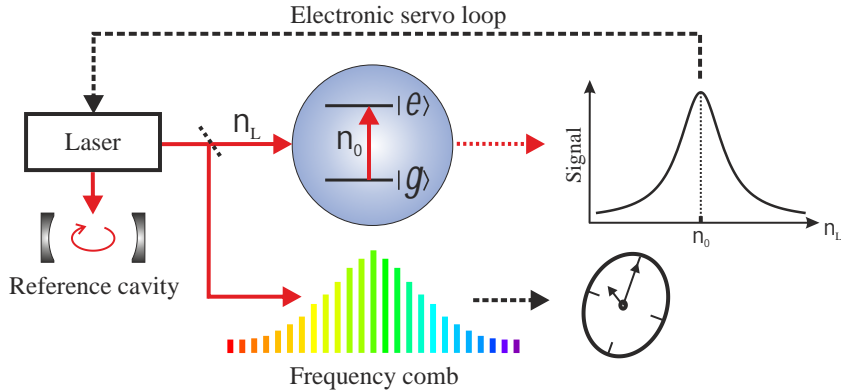


Figure 1.1: Principle of optical clocks. A narrow-linewidth laser, which is pre-stabilized to a frequency reference (e.g. a high-finesse optical cavity), interrogates the narrow clock transition in ions or neutral atoms. The detected absorption signal of the laser is converted into an error signal acting back on the laser frequency via an electronic servo loop. For determination of the optical frequency, the laser is compared against an optical frequency comb. In analogy to the traditional clock-face, a suitable device can display the "counted" clock frequency.

are confined in the interference pattern of a high-power standing wave realized by at least one pair of counter-propagating laser beams [30]. The spatial confinement of these *optical lattices* also satisfies the conditions for spectroscopy in the Lamb-Dicke regime, as has been demonstrated by Hidetoshi Katori and co-workers [31]. Furthermore, the wavelength of this optical lattice was chosen such, that the AC Stark shifts acting on the interrogated clock states canceled out in first order. This work led to the proposal of the *optical lattice clock*, where the strongly forbidden $^1S_0 \rightarrow ^3P_0$ transition is interrogated in alkaline earth(-like) elements confined to a *magic wavelength* optical lattice [32]. Possible atomic candidates for optical lattice clocks are Sr, Yb, Hg and Mg.

Optical clocks operating with ions or neutral atoms have the same basic working principle, as depicted in Figure 1.1: the narrow, optical transition of the absorber is probed by sweeping the frequency of an interrogation laser over the spectral resonance. To provide an intrinsic narrow laser linewidth, being able to resolve the atomic resonance, this laser needs to be pre-stabilized to an optical cavity with a high finesse [33] or to a narrow resonance in a crystalline structure obtained via spectral-hole burning [34]. If laser photons are absorbed by the atom or the ion, their spontaneously emitted fluorescence can be detected (using a CCD camera or a photo multiplier) for the generation of a dispersive error signal. Fed to an electronic feedback loop, this signal will act back on the laser frequency for keeping it resonant with the atomic line center. So far, this setup would be considered as *optical frequency standard* [35]. If the laser frequency is determined by means of an optical frequency comb and displayed with a suitable device, it will act as an *optical clock*.

Improvement of the world's optical clocks is continuously progressing, where ion and lattice clocks are having a close neck-and-neck race for the highest accuracies.

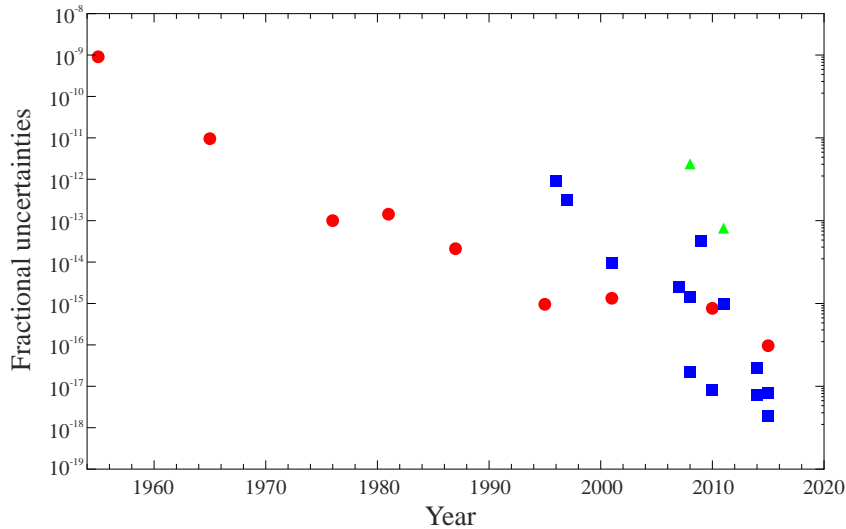


Figure 1.2: Fractional uncertainties of atomic frequency standards. Depicted are reported accuracies of Cs standards (red circles, [6, 12, 16, 42–47]) and optical frequency standards (blue squares, [18, 19, 38–40, 48–55]), including ion and neutral atom clocks. The green triangles denote the frequency measurements of the $^1S_0 \rightarrow ^3P_1$ intercombination line in ^{24}Mg [56, 57].

In any case, the performance of optical clocks in both accuracy and stability has already surpassed those of state-of-the-art cesium clocks. A systematic effect, that had limited the accuracies of Sr and Yb clocks for a long time, is given by the black body radiation (BBR) induced frequency shift for room temperature environment at 300 K. The uncertainty related to the BBR shift could finally be reduced by precisely measuring its static contribution [36, 37], the environmental temperature [38] or by operating the clock in cryogenic environment [39], therefore suppressing the BBR effects. So far, the most accurate optical clock that has recently been reported, is the Sr lattice clock in the group of Jun Ye at JILA (Joint Institute for Laboratory Astrophysics) with a fractional uncertainty of 2×10^{-18} [40]. Figure 1.2 gives an overview of several atomic frequency standards that were reported within the last 60 years, starting with Essen’s Cs clock in 1955 and ending with Ye’s Sr clock in 2015, showing a remarkable improvement of nearly nine orders of magnitude in between and finally proving Arthur L. Schawlow to be only halfway right [1]: the first optical clock to measure at the 10^{-17} accuracy level was again the $^{199}\text{Hg}^+$ ion clock at NIST, but it took at least 25 years to demonstrate [41].

The record demonstration of 2×10^{-18} accuracy enables the detection of differences in the gravitational potential on a very precise scale. If two identical clocks of this kind were placed with a difference in height of Δh , the upper clock will run slightly faster according to

$$\frac{\delta\nu}{\nu_0} = \frac{g\Delta h}{c^2}, \quad (1.2)$$

where $g \approx 9.81 \text{ m/s}^2$ is the local gravitational acceleration [58]. Consequently, two

of the world's most accurate Sr clocks would measure a clock shift corresponding to a gravitational red-shift, if placed with $\Delta h \approx 2$ cm. This level of precision suggests to "*ask no longer what time it is, better ask how high I am*" [59]. In fact, the development of optical clocks suggests, that these highly sensitive quantum sensors will improve measurements in relativistic geodesy, hence displaying a fundamental application [60–62].

Among the candidates for optical lattice clocks, Mg features a total sensitivity to BBR being an order of magnitude smaller as compared to Sr or Yb [63]. Although laser-cooling techniques are not as advanced as for the other clock species, which is mainly due to the narrow $^1S_0 \rightarrow ^3P_1$ intercombination line at 457 nm as well as the lack of adequate sub-Doppler cooling techniques, a *continuous loading scheme* for optical dipole traps [64, 65] enabled the transfer of cold magnesium atoms into an optical lattice for clock spectroscopy [66].

As in all bosonic alkaline earth(-like) isotopes, the $^1S_0 \rightarrow ^3P_0$ clock transition in ^{24}Mg is strongly forbidden. Optical dipole coupling of the two clock states can be enhanced through a homogeneous magnetic field being applied during clock interrogation [67–69]. Enabling $\sim \mu\text{Hz}$ linewidth, the clock transition in ^{24}Mg offers the largest line- Q among the candidates for optical lattice clocks.

The scope of this thesis

In the frame of this work, important atomic parameters for magnesium were determined: the magic wavelength of the $^1S_0 \rightarrow ^3P_0$ clock transition and its second-order Zeeman shift, both being fundamental for the realization of a future magnesium optical lattice clock. Furthermore, the determination of these parameters allowed a first direct spectroscopic measurement of the clock transition frequency.

This thesis is organized as follows: **Chapter 2** gives a short overview on the setup of the experiment. The techniques that are used for state preparation of atoms in the magic wavelength lattice are described in **Chapter 3**, followed by a brief introduction of the clock interrogation scheme using a magnetic field for enhancing the dipole coupling of the clock states. **Chapter 4** provides the theoretical background for spectroscopy in the Lamb-Dicke regime, starting out from the ideal potential of a harmonic oscillator. Introducing the potential of an optical lattice, several effects having an impact on lattice Lamb-Dicke spectroscopy are discussed. The experimental results on clock spectroscopy and systematic frequency shift studies are summarized in **Chapter 5**. This thesis concludes with an outlook on the next steps to be taken towards a frequency measurement in lattice-trapped magnesium in **Chapter 6**, including a perspective on future measurements.

Experimental setup

In this chapter, I will give a brief description on the setup of our vacuum apparatus (Section 2.1), the magnetic fields being available for experiments (Section 2.2) and how detection is carried out in our experiment (Section 2.3). For more detailed information on each of these sections, I recommend previous theses of our work group.

2.1 Vacuum apparatus

Experiments in atom optics are usually performed in ultra-high vacuum ($< 10^{-10}$ mBar) requiring special apparatuses for each individual application. Vacuum pumps therefore are responsible for providing a stable environment that reduces the interaction of atoms under investigation with foreign particles. In the Magnesium experiment, the main experimental chamber is separated from the source chamber containing an oven filled with solid slices of magnesium. These two chambers are connected through an aperture of 5 mm diameter showing the same effect as a differential pumping stage: while having a high vapor pressure in the source chamber, the pressure in the main chamber is about 2.9×10^{-9} mBar. Although this does not display an ultra-high vacuum in this case, this setup is sufficient for the applications in the Magnesium experiment that are described in this thesis.

The source chamber contains the oven for sublimating solid magnesium which has been designed in [70]. In principle it consists of a cylindrical steel reservoir being filled with metallic slices. Applying an electric voltage, this reservoir heats up to 450 °C. At this temperature the vapor pressure inside the source chamber enables sufficient loading rates into the magneto-optical traps and dipole traps. Magnesium atoms being in the gaseous phase may exit the steel cylinder through

tiny bores. The already above mentioned aperture between source and main chamber has the additional feature of forming a collimated, thermal beam of magnesium atoms. If necessary, the aperture can be closed via external computer control by means of a shutter for reducing the interaction of optically prepared ensembles with hot magnesium atoms.

The source chamber is connected to a metal bellow which is attached to the main chamber using a DN63CF flange. The main chamber, which has been designed and set up in [71], consists of a cylinder made of stainless steel with 210 mm diameter being oriented in the vertical plane. Opposite to the source chamber is another DN63CF adapter flange going to a cross with a turbomolecular pump, an ion getter pump, a vacuum sensor and a view port for irradiating the Zeeman slowing beam and the triplet-MOT repumping beams. Furthermore, there are two more DN63CF and eight DN40CF flanges attached horizontally to the chamber for optical access. Vertically, the chamber is closed with two DN200CF pot flanges allowing for the pair of Helmholtz coils being close to the atoms. Figure 2.1 shows a horizontal cut through the main chamber with the laser beams used for the experiments. Those view ports marked with an "M" are used for the magneto-optical traps at 285 nm and 383 nm, respectively. The remaining two DN63CF flanges are used for optical access of the optical dipole trap at 1064 nm, the magic wavelength lattice at 468 nm, the transfer laser at 457 nm and the clock laser at 458 nm. At the moment, these flanges are going conical to DN40CF flanges with vacuum windows being sealed with indium. As it has been observed in a previous dissertation, these vacuum windows were contaminated (most probably with residual magnesium condensing on the windows) from the vacuum side and thus limiting the maximum power in the optical lattice enhancement cavity [66]. The windows have been replaced in the frame of this thesis. New windows embedded in DN63CF flanges have been purchased offering less absorption at 1064 nm and thus less heating due to laser radiation as well as more space for optomechanics.

One of the remaining DN40CF view ports is used for fluorescence detection of atoms on a CCD¹ camera. The window being opposite could be optionally used for absorption detection of metastable atoms at 383 nm. The last window axis offers additional space for the implementation of a photomultiplier and an additional laser beam, respectively.

2.2 Magnetic fields

Magnetic fields play a major role in atom optics experiments, as they are used for controlling atomic states (e.g. as a permanent magnet used in a Zeeman slower, where atoms are kept on resonance with the applied slowing beam depending on their spatial position), for trapping atoms (magnetic trap) or for compensating

¹charge-coupled device

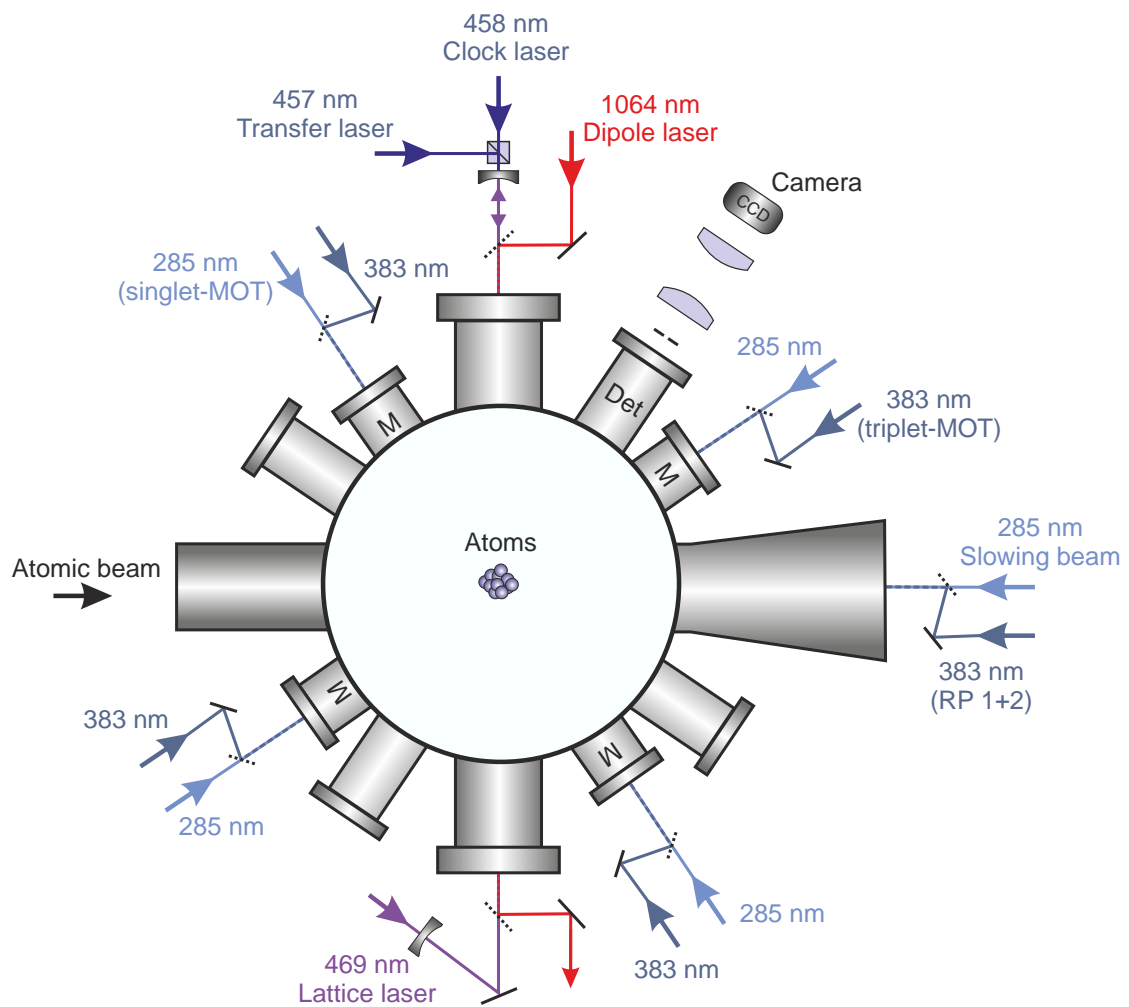


Figure 2.1: Horizontal cut through the experimental chamber. Depicted are the relevant laser beams for state preparation and optical trapping. View ports indicated with an "M" are used for the operation of the two UV magneto-optical traps. The fluorescence of atoms is detected with a camera located at the view port "Det". Not shown is the oven chamber, where solid magnesium is sublimated and formed into a thermal beam by means of an aperture.

parasitic fields like the earth's magnetic field. According to this, one finds several different magnetic field configurations in such an experimental chamber. In the case of the Magnesium experiment there are four types of magnetic fields that can be made use of and that shall be briefly described in the following.

Quadrupole field

To obtain a spatial enclosure for atoms, one needs -besides a near-resonant light field- a magnetic quadrupole field featuring a local minimum of field strength being ideally in the center of the experimental chamber. As the magnetic field minimum defines the position of the atoms, all laser beams used in the experiment are aligned with respect to it. The quadrupole field is generated with a pair of coils being arranged parallel to each other. If the direction of current flow is equal for both coils, one receives the so-called *Helmholtz configuration* generating a homogeneous magnetic field between the coils. In the case of counter-propagating current flow, one receives the already mentioned quadrupole field in *Anti-Helmholtz configuration*. The coils have been wound in [71] and consist of a tubular copper wire allowing for water cooling. As the coils are placed in the earlier described pot flanges, they are only 4 cm away from the position of the atoms. The coils are electrically connected in series to a power supply² giving a maximum current of about 200 A. The current flowing through the wires can be regulated within 30 μ s using an IGBT (*Insulated Gate Bipolar Transistor*), but the decay time of the magnetic field is much larger being 2 ms, as eddy currents are induced in the steel apparatuses preserving the magnetic field [72]. With a maximum current of 200 A, magnetic field gradients of 1.3 T/m (equivalent to 130 G/cm) can be achieved in the strong axis and 0.65 T/m (65 G/cm) in the weak axis, respectively [71].

Homogeneous magnetic field for optical spectroscopy

In the case of the bosonic isotope ^{24}Mg , an external homogeneous magnetic field is necessary for enhancing optical dipole excitation of the spin-forbidden $^1S_0 \rightarrow ^3P_0$ clock transition, as there is no natural coupling between the 3P_0 and 3P_1 states due to the lack of a nuclear spin. In the experiment, this field is created by switching the main coils of the quadrupole field from Anti-Helmholtz to Helmholtz configuration by means of four IGBTs in a so-called *H-bridge wiring*, whereas the lower coil is forming the bridge section.

Thus, we generate a magnetic field of 2.49(1) G/A, determined via optical Zeeman spectroscopy of the $^1S_0(m_J = 0) \rightarrow ^3P_1(m_J = \pm 1)$ transitions. A maximum current of 200 A therefore generates a maximum magnetic field of about 50 mT (500 G) which is sufficient for enabling clock spectroscopy in magnesium. The coils have been calibrated by means of a current probe being attached to the wire

²6682A, Hewlett Packard

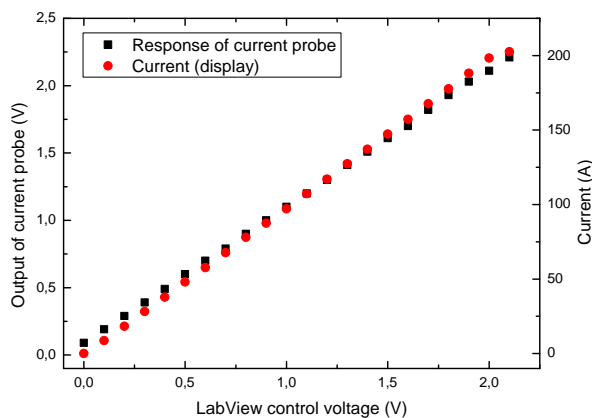


Figure 2.2: Calibration of the magnetic field coils. The current flowing through the coils (red dots) as well as the response of a current probe (black squares) have been measured as a function of computer control voltage.

going to the upper coil. The absolute current value was read on the display of the power supply. As can be seen from Figure 2.2, the magnetic field strength grows linearly, even at high currents of 200 A.

Homogeneous magnetic field for state selection

Another homogeneous magnetic field with amplitude of 1.05 G/A ($105 \mu\text{T}/\text{A}$) can be applied to the apparatus through windings around the two DN200CF pot flanges. The maximum current is limited to 4 A due to heating inside the coils [64]. This magnetic field is suitable for lifting the degeneracy of the $^3P_1 m_J$ substates by means of the Zeeman effect and thus a controlled excitation of a certain magnetic sub component.

Homogeneous fields for compensation of stray fields

To avoid perturbations induced by the earth's magnetic field or by stray fields arising from the ion getter pump, a cubic arrangement of each a pair of coils in Helmholtz configuration per cubic axis is attached around the main chamber [73]. The center of this coil arrangement is identical with the position of the atoms, generating a magnetic field of maximum 1 G ($100 \mu\text{T}$).

2.3 Detection of atoms

Besides the preparation and manipulation of atoms in precision experiments, detection plays an enormous role, giving knowledge about properties like number of

atoms, atomic density and temperature of atoms. Atoms being in an excited state (as a result of laser light interaction or a comparable suitable energy input) can be detected through the spontaneous emission of photons, as they decay back to a lower state. These photons can then be detected with a camera or a photomultiplier, so one would talk of *fluorescence detection* in this case. Another method of detection is given by *absorption detection*, where atoms are resonantly illuminated with laser light casting the atomic cloud on the camera chip. In the Magnesium experiment, we are focussing on fluorescence detection, which shall be described in more details in the following section.

Theoretical setting

To correctly determine the number of atoms, it is important to know the number of photons being emitted during the detection process. Looking for a theoretical description, atom-light interaction for a two-level atom is well described by the stationary solution of the *Optical Bloch Equations*. According to them, the excited state fraction is given by

$$\rho_{\text{excited}} = \frac{\Omega^2/4}{\delta^2 + \Omega^2/2 + \gamma^2/4}, \quad (2.1)$$

with Ω being the Rabi frequency of the transition, γ being the natural linewidth and scattering rate, respectively, and δ is the detuning relative to the resonance frequency of the transition [74]. Introducing the so-called *resonant saturation parameter*

$$s_0 \equiv \frac{I}{I_{\text{sat}}} = \frac{2\Omega^2}{\gamma^2} \quad (2.2)$$

together with the *saturation intensity* of the transition of choice,

$$I_{\text{sat}} = \frac{\pi}{3} \frac{hc}{\lambda^3 \tau}, \quad (2.3)$$

where λ is the wavelength and $\tau = 1/\gamma$ is the lifetime of the transition, Eq. 2.1 evolves into

$$\rho_{\text{excited}} = \frac{1}{2} \frac{s_0}{s_0 + 1 + \frac{4\delta^2}{\gamma^2}}. \quad (2.4)$$

Eq. 2.4 gives an intuitive dependence on the intensity I of the pumping laser. If the laser is exactly tuned to the atomic resonance frequency and operated with an intensity $I = I_{\text{sat}}$, one will find a fraction of 0.25 of atoms being in the excited state. For large laser intensities ($s_0 \gg 1$) the system will reach a steady-state equilibrium with an excited state fraction of $\rho_{\text{excited}} \rightarrow 1/2$. As the excited state decays with γ and the excitation rate equals the decay rate in the case of a steady-state equilibrium, the total photon scattering rate γ_{ph} results to

$$\gamma_{\text{Ph}} = \gamma \rho_{\text{excited}} = \frac{\gamma}{2} \frac{s_0}{s_0 + 1 + \frac{4\delta^2}{\gamma^2}} \quad (2.5)$$

with an equilibrium value of $\gamma/2$ for $s_0 \gg 1$ [75].

As the photon scattering rate is proportional to the linewidth of the atomic transition, it is profitable to use cooling transitions with a linewidth of several MHz for optical detection. In the experiment, usually the MOT beams are applied to the atoms.

Optomechanical setup and digital processing

The fluorescence being emitted by the photons is detected on a CCD camera at the viewport "Det" (see Figure 2.1). An iris located in front of the viewport can be used for regulation of the detection solid angle and thus the level of illumination of the camera chip. Furthermore, a lens system of two lenses with identical focal length, which is placed between main chamber and camera, allows for original size imaging of the atomic clouds. A computer controlled mechanical shutter is used for regulating the illumination time of the CCD chip.

The recorded camera pictures are forwarded to the laboratory computer and can be analyzed using various kinds of software. A specific Mathematica code has been developed in [66] for distinguishing weak atomic signals, as they occur during lattice measurements, from typical background noise. First, several pictures taken from small atomic clouds are averaged before the same pictures are taken with no atoms being present, but obviously are containing residual stray light etc. (background pictures). As a next step, a kind of "model mask" is calculated, containing the averaged cloud pictures and background pictures, before it is compared with any freshly taken picture through a least square fit for calculation of the number of atoms.

State preparation

This chapter treats the experimental procedures and challenges of atomic state preparation as a prerequisite for clock spectroscopy. The relevant level scheme and atomic properties of magnesium are discussed in Section 3.1. Section 3.2 treats the two ultraviolet magneto-optical traps we are using for laser-cooling of ^{24}Mg . The experimental scheme for loading cold atoms into optical traps is described in Section 3.3. As the $^1S_0 \rightarrow ^3P_0$ clock transition is strongly forbidden for bosonic isotopes, Section 3.4 discusses a scheme for operating a lattice clock with bosonic ^{24}Mg , based on magnetically enhanced dipole coupling of the two clock states.

3.1 Relevant level scheme of ^{24}Mg

Magnesium belongs to the group of alkaline-earth metals that are categorized in Group 2 of the periodic table of elements, as they possess two valence electrons in their outer shell. The presence of two electrons, whose relative spin orientation can be parallel (total spin $S = 1$) or anti-parallel (total spin $S = 0$), comes together with a variety of electronic transitions. Those with changing multiplicity $2S + 1$ are forbidden at a first glance due to general selection rules [76] and thus result in a very narrow transition linewidth. They are referred to as *intercombination lines* and are of high interest in frequency metrology for the development of optical frequency standards.

Besides magnesium, there are the other alkaline earth metals calcium and strontium as well as the alkaline earth-like elements ytterbium (lanthanide) and mercury (transition metal) being object of scientific research on optical frequency standards with neutral atoms as they all have similar properties e.g. like the level structure.

Naturally occurring magnesium shows a mixture of three stable isotopes: the bosonic isotopes ^{24}Mg and ^{26}Mg with a natural abundance of 78.99% and 11.01%, respectively, and the fermionic isotope ^{25}Mg with a natural abundance of 10% [77].

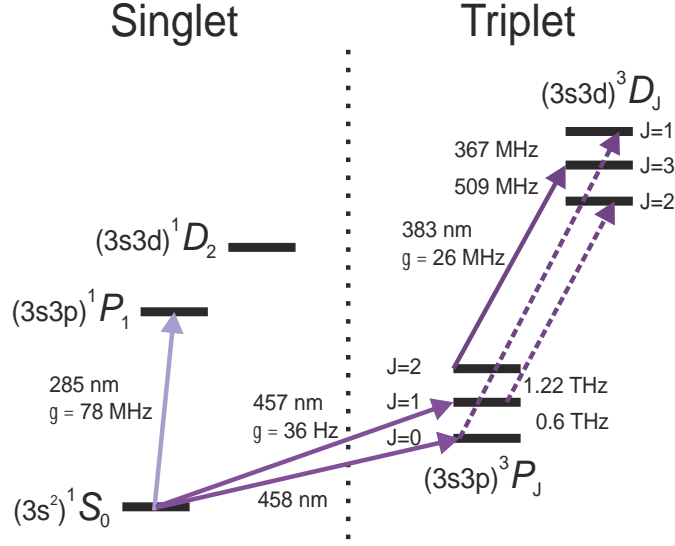


Figure 3.1: Relevant level scheme of ^{24}Mg . Linewidths are given in $\Gamma/2\pi$.

Isotopes of a certain atomic species feature all the same proton number Z , which is equivalent to the atomic number in the periodic table of elements, but differ in the number of their neutrons N . The sum of protons and neutrons forms the totality of core particles and is defined as nucleon number (or mass number) A of an isotope [78]. For even Z and N , as it is the case for ^{24}Mg and ^{26}Mg with $Z = 12$, isotopes have a vanishing nuclear spin $|\mathbf{I}| = 0$. Accordingly, for odd nucleon numbers, isotopes have half-integer nuclear spins (^{25}Mg : $|\mathbf{I}| = 5/2$). The interaction between nuclear spin \mathbf{I} and total angular momentum \mathbf{J} finally leads to an energy splitting for each energy level $E_{n,l,j}$ into the respective *hyperfine components*, by introducing the total angular momentum $\mathbf{F} = \mathbf{I} + \mathbf{J}$ [79].

Experiments described in this thesis have been carried out on bosonic ^{24}Mg , having a relative atomic mass of 23.98504 [80]. As the two valence electrons of magnesium occupy the third atomic shell (M shell), the electronic ground state of ^{24}Mg is $(3s^2)^1S_0$. The nomenclature of term symbols $^{2S+1}L_J$ goes back to LS coupling (also called Russell-Saunders coupling) and includes information about the total spin of the two electrons, the total orbital angular momentum L and the total electronic angular momentum J of a given state [74]. In the following, I will restrict myself in the description of atomic states to just the term symbol without the atomic orbitals.

Figure 3.1 shows an excerpt of the ^{24}Mg level scheme with the transitions being relevant for this work. The first magneto-optical trap (MOT) cooling stage is carried out on the 78 MHz broad $^1S_0 \rightarrow ^1P_1$ transition at 285 nm (and referred to as "*singlet-MOT*"). In magnesium, the 1D_2 state is energetically higher than the 1P_1 state. This is advantageous, as there is no natural decay channel from the 1P_1 state to the $^3P_{1,2}$ states via 1D_2 , as e.g. in strontium. In essence, the singlet-MOT

cooling transition displays a closed cycle therefore needing just a single laser for stable MOT operation.

The pre-cooled atoms are then optically pumped to the triplet manifold via the $^1S_0 \rightarrow ^3P_1$ intercombination line at 457 nm. A second-stage MOT is realized on the 26 MHz broad $^3P_2 \rightarrow ^3D_3$ transition at 383 nm. Here, parasitic excitations to the $^3D_{1,2}$ states may occur that decay to the $^3P_{0,1}$ states. Hence, two repumping lasers are needed to close the cooling cycle of this MOT (referred to as "*triplet-MOT*"). Finally, a continuous loading scheme for an optical dipole trap at 1064 nm allows for the accumulation of cold 3P_0 atoms [64, 65]. As it has been demonstrated in a previous work, these atoms can be further transferred to an optical lattice at the predicted magic wavelength of 469 nm [66].

3.2 Laser cooling of ^{24}Mg

In this section, I will discuss the essential experimental steps as well as the main characteristics of laser cooling of ^{24}Mg . A detailed description can be found in previous dissertations of our group [64, 66, 70–72] and shall not be repeated in the scope of this thesis. For a theoretical treatment of laser cooling I refer to standard works in atom optics of [74, 75].

As already mentioned in the previous section, laser cooling in the Magnesium experiment is carried out in the ultraviolet regime of the electromagnetic spectrum. Although the simple level structure of bosonic ^{24}Mg in principle is advantageous, laser operation at 285 nm and 383 nm, respectively, displays a more complex experimental effort, as laser diodes at these wavelengths are not commercially available yet. A well established method of generating UV radiation is the resonant second harmonic generation (SHG) in a cavity, going along with high-power laser systems at 570 nm (1140 nm) and 766 nm.

Another challenge to the experiment is given by the linewidths of the cooling transitions in ^{24}Mg : the rather broad transitions in the singlet and the triplet manifold limit the application of laser cooling to approximately 1 mK Doppler temperature, whereas the $^1S_0 \rightarrow ^3P_1$ intercombination line is not suitable for MOT operation. According to Eq. 2.5, only 6 photons would be scattered per second in this case.

3.2.1 The singlet-MOT at 285 nm

In our experiment, laser radiation at 285 nm is generated with SHG of the output of a commercial laser system at 570 nm¹. This laser unit consists of a diode laser in ECDL (*External Cavity Diode Laser*) configuration at 1140 nm which is

¹DL-RFA-SHG Pro, Toptica

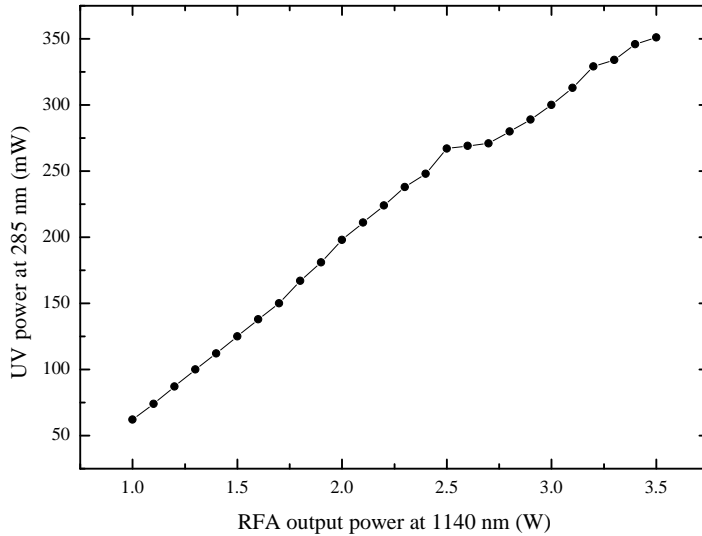


Figure 3.2: Generated laser power at 285 nm as a function of the quadruple fundamental at 1140 nm of the RFA. The maximum output power in the UV is approximately 350 mW.

further amplified using a Raman fiber amplifier (RFA) and, as a next step, frequency doubled via SHG to 570 nm with a maximum optical laser power of 3 W. A detailed documentation on this laser system can be found in [66]. For frequency stabilization, we apply a Doppler-free polarization spectroscopy, similar as in [81], by sending a small amount of yellow laser light through a polarization maintaining (PM) fiber to an iodine spectroscopy setup. Further details on this locking scheme as well as the used hyperfine transition in the R115(20-1) iodine line are given in [64]. In general, an achieved laser linewidth of a few MHz would be sufficient for addressing the 78 MHz broad $^1S_0 \rightarrow ^1P_1$ cooling transition.

Laser light at 285 nm is generated using a self-built SHG cavity in *bow tie*² configuration [82]. The cavity length is stabilized using the *Pound-Drever-Hall* (PDH) technique [33], while the maximum output power is about 350 mW at 285 nm (see Figure 3.2). As UV radiation acts quite aggressively on optical coatings, thereby causing degradation of the SHG crystal surfaces, we operate the cavity in the experiment with a maximum output power of 100 mW. The output beam is split into two parts using an acousto-optical modulator (AOM): One part is needed for Zeeman slowing (0th diffraction order), while approximately 50 mW are needed for the singlet-MOT (-1st diffraction order, corresponding to a detuning of -78 MHz, which is $-\gamma$). The cooling light is further split into the six MOT beams using

²The name "*bow tie*" is related to the four-mirror-setup the laser light is traveling along during the SHG process.

polarizing beam splitters (PBS) and is guided to the main chamber in counter-propagating beam pairs for each direction in space. The Zeeman slowing beam passes another AOM with a detuning of -220 MHz and is guided through a viewport of the main chamber being opposite to the oven.

Operating the singlet-MOT with a loading time of 3 s, we trap about 3×10^9 magnesium atoms at a temperature of 3 mK, which is slightly above the theoretical Doppler-limit of 1.9 mK [71]. In the same work, the singlet-MOT life time has been determined to 4.7 s.

3.2.2 Optical transfer at 457 nm

In magnesium, atoms being in the 1P_1 state cannot decay to the metastable 3P states³. This means, in our experiment, metastable atoms can only occur via laser excitation of the 36 Hz narrow $^1S_0 \rightarrow ^3P_1$ transition at 457 nm. As already mentioned in the previous subsection, singlet-MOT cooled atoms have a temperature of 3 mK, thus one would expect a Doppler broadening [83] of the natural linewidth of the intercombination line to ~ 5 MHz, according to

$$\delta\omega_D = \frac{\nu_0}{c} \sqrt{\frac{8k_B T \ln 2}{m}}. \quad (3.1)$$

The laser system for this blue transition consists of a commercial ECDL at 914 nm, which is amplified using a tapered amplifier and subsequently frequency doubled to 457 nm in a SHG cavity⁴. As the $^1S_0 \rightarrow ^3P_1$ intercombination line had been used as clock transition in previous works [56, 57, 72], intrinsic narrow laser linewidths had been required. A well-established method in this case is the frequency stabilization of the laser to an optical cavity using the PDH technique. Here, the cavity is made of ULE (*Ultra Low Expansion*) glass being coated for 457 nm. ULE features a low thermal expansion of the resonator at room temperature and hence reduces its influence on laser frequency stability. The stabilized laser linewidth could be estimated to be below 1 kHz [56].

The typical output power of the laser is 200 mW at 457 nm. A small amount of laser light is used for the above mentioned frequency stabilization to the ULE cavity. Therefore, the light passes a double-pass AOM and is fiber-guided to the resonator setup. The main part of the laser light passes a control-AOM operated at 79 MHz and is fiber-guided to the experimental main chamber. Here, 30 mW of optical power in the blue are available for optical pumping the atoms from the electronic singlet to the triplet manifold.

³In the case of strontium, the 1D_2 state has less energy than the 1P_1 state, hence atoms can undergo parasitic decays via the former to the metastable states.

⁴TA-SHG-110, Toptica Photonics

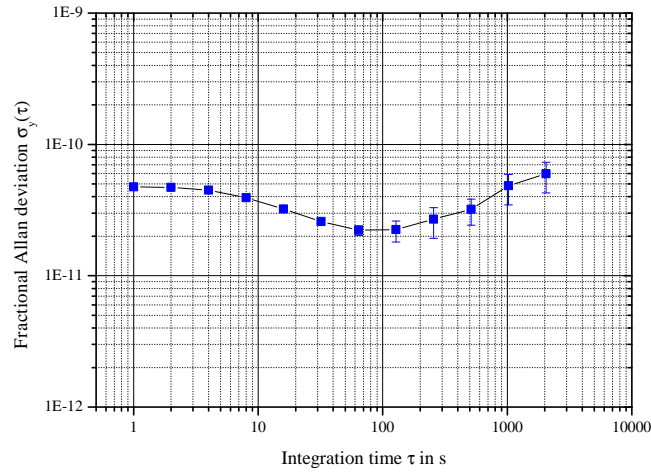


Figure 3.3: Fractional frequency instability of the beat note between the triplet-MOT cooling laser and RP 2, with both laser frequencies being locked to the transfer cavity.

3.2.3 The triplet-MOT at 383 nm

Contrary to the singlet-MOT, which is operated on a closed transition, three lasers are necessary for a metastable MOT (triplet-MOT) operated on the $^3P_2 \rightarrow ^3D_3$ cooling transition at 383 nm (see. Figure 3.1). After the application of the 457 nm pumping laser, the short-lived 3P_1 state needs to be depopulated, otherwise atoms would decay back to the ground state within a few ms [84]. A repumping laser (RP 1) driving the $^3P_1 \rightarrow ^3D_2$ transition finally transfers 3P_1 atoms to the 3P_2 state, where the cooling laser is applied. As excitation to the 3D_1 state, with subsequent relaxation to 3P_0 , is very likely due to the small energy spacing of the upper 3D_J states, a second repumping laser (RP 2), operating on the $^3P_0 \rightarrow ^3D_1$ transition, closes the MOT cooling cycle.

Each of the three triplet-MOT lasers is a MOPA (*Master Oscillator Power Amplifier*⁵) of identical setup with 1 W optical power at 766 nm, but their frequencies differ by more than 1 THz (corresponding to the metastable transitions at 383 nm). They are stabilized to a Doppler-free saturation spectroscopy of ^{39}K at 766 nm via a transfer cavity. At first, the transfer cavity length is locked to the ^{39}K probe laser. Afterwards, the triplet-MOT lasers are stabilized to a cavity resonance⁶ using the PDH technique (diode current modulation).

The locking performance of the transfer cavity was determined in the time

⁵A MOPA combines an ECDL seeding a tapered amplifier.

⁶Usually, the frequency distance between two longitudinal modes of a cavity corresponds to the free spectral range (FSR), if the cavity is aligned to the optimum. For a cavity length of 7 cm this would be ~ 2 GHz. However, clever alignment generates higher order modes with separation of 112 MHz only. Read [64, 85, 86] for more information.

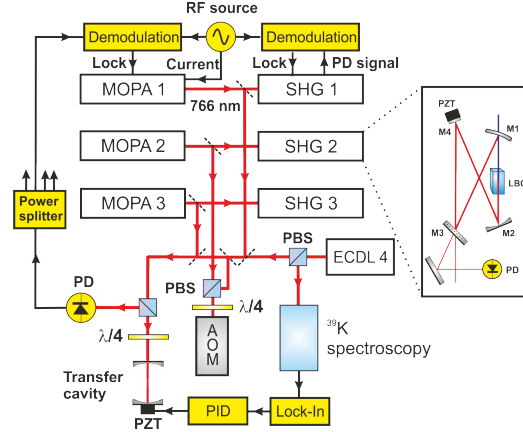


Figure 3.4: Reduced schematic setup of the laser system at 383 nm. The locking scheme is shown in detail only for MOPA 1 for clarity. Not depicted are the control-AOMs for the UV light as well as the fiber guiding optics. Blow-up: Bow tie cavity design for SHG. (PZT: piezo-electric transducer, PBS: polarising beam splitter, PD: photo diode)

domain by comparing the triplet-MOT cooling laser with RP 2, while being locked to adjacent modes of the cavity. Their frequency difference was 200 MHz and the locking servo bandwidth was a few 100 kHz. The beat signal of the lasers was recorded with a photo diode and fed to a frequency counter with zero dead time (gate time 1 s). From the time series, the corresponding Allan deviation was calculated and is depicted in Figure 3.3. The relative frequency instability reaches a flicker floor of $\sigma_y \approx 2 \times 10^{-11}$ at 100 s integration time resulting from jitters in the laser frequency servo loop.

The generation of UV light at 383 nm is realized in three independent SHG bow tie cavities, whose lengths are stabilized to the incident red light at 766 nm using the PDH locking scheme. Here, the same modulation frequency, that has been imprinted on the corresponding laser diode current, is used for the deduction of the SHG locking error signal. Each SHG cavity generates about 100 mW optical output power. Figure 3.4 shows a reduced schematic of the laser system. Further details on this laser system can be found in [64, 72, 87].

The 383 nm cooling laser passes a control-AOM before being split into six paths using PBSs with fiber coupling to the experimental main chamber. There, the 383 nm light is overlapped with the 285 nm light for each MOT direction in space and irradiated to the atoms. At the position of the atoms, each triplet-MOT beam has an optical power of about 1.5 mW. The alignment of the beams is optimized to a maximum spatial overlap between triplet-MOT and the optical dipole trap at 1064 nm. The result is a very compact and highly fluorescent triplet-MOT featuring life times of more than 1 s (see Appendix A for the corresponding measurements). Both UV repumpers are guided to the experiment sharing the same optical fiber, after each passing a control-AOM for fast switching of the laser light. The lasers are irradiated through one optical view port only (the same port

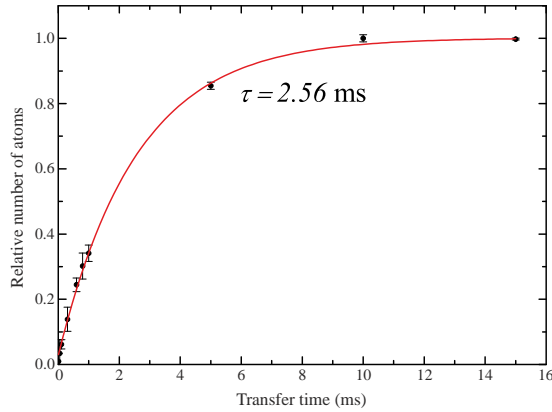


Figure 3.5: Loading curve of the triplet-MOT as a function of 457 nm irradiation time and a time constant of $\tau = 2.56$ ms. The maximum number of atoms is 1.6×10^8 .

used for Zeeman slowing), both having an optical power of about 5 mW at 383 nm.

The typical, experimental sequence for loading of the triplet-MOT is as follows: The singlet-MOT is being loaded for 1 s with all 383 nm lasers being irradiated (excitation to the metastable states does not yet occur), followed by a pumping phase where the 457 nm transfer laser is applied. Finally, a pure triplet-MOT sequence of 10 ms duration takes place, where no singlet atoms are present anymore.

Figure 3.5 shows the number of atoms being captured by the triplet-MOT as a function of 457 nm transfer pulse time. The loading rate of the triplet-MOT is 6.3×10^{10} atoms/s. Hence, the pulse time is chosen to be 15 ms in the experiment, where we capture about 1.6×10^8 atoms in the triplet-MOT.

3.3 Optical trapping of ^{24}Mg

The presence of broad cooling transitions as well as the lack of adequate sub-Doppler cooling techniques in ^{24}Mg define an experimental challenge for a future, lattice-based frequency standard with magnesium. Compensating these disadvantages, a *continuous loading scheme* for an optical dipole trap has been implemented [64, 65], which shall be briefly discussed in the following subsection, before I will describe the setup as well as the loading procedure of the magic wavelength lattice.

3.3.1 Continuous loading of an optical dipole trap at 1064 nm

Laser light for the 1064 nm optical dipole trap is provided by an ytterbium doped fiber laser⁷ with 48 W maximum output power. The laser is focused down to a beam waist of 72 μm , hence we achieve a maximum trap depth of $U/k_B = -142 \mu\text{K}$. The dipole trap beam is spatially overlapped with the triplet-MOT, while the latter one has been optimized for ideal mode-matching, as already mentioned in the previous section.

As it has been demonstrated in [64, 65], light-assisted two-body collisions limit the triplet-MOT density and hence the transfer efficiency to the optical dipole trap, as only the coldest atoms, whose kinetic energy is smaller than the potential depth, can accumulate in the trap. This is the case, if the triplet-MOT is operated as described in Subsection 3.2.3. As a consequence, only 1,000 atoms being in the 3P_2 state will be captured in the dipole trap.

However, if a loss channel for cold atoms is introduced to the 3P_0 state by turning off the corresponding repumping laser (RP 2), those atoms are not returned to the cooling cycle of the MOT. Irradiating every other laser (285 nm singlet-MOT, 457 nm transfer laser, 383 nm cooling laser, 383 nm RP 1 and 1064 nm dipole laser), continuously pumps pre-cooled singlet atoms from a quasi-infinite reservoir to the triplet manifold. The dipole potential now serves as energy filter for 3P_0 atoms, as they are released from the cooling cycle. With this scheme, we were able to increase the number of atoms in the optical dipole trap by two orders of magnitude to 10^5 atoms at a temperature of 100 μK .

There are related schemes like the continuous loading of a dipole trap with ground state calcium atoms via spatially selective optical pumping [88], as well as the continuous loading of a magic wavelength lattice with strontium atoms [89]. In the latter case, the lattice has a trap depth of 200 μK and is directly applied to the mK-hot singlet-MOT. Through selective optical pumping to the metastable states, a loading rate of $\sim 10^5$ atoms/s has been achieved. However, there are two reasons why a direct loading of a magic wavelength lattice is impossible so far in our experiment:

- (i) To load the lattice directly from the 3 mK-hot singlet-MOT, high trap depths are required. As an example, for the generation of a 250 μK deep trap at the magic wavelength, 24 W at 468 nm would have to be applied and focused down to a waist of 79 μm . Here, the challenge is given by laser light generation.
- (ii) The continuous loading scheme, as described further above for the optical dipole trap, cannot be applied to the magic wavelength lattice (even for a

⁷YLM, IPG Photonics

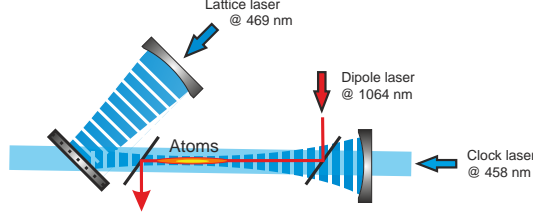


Figure 3.6: Schematic of the lattice setup. The clock laser is transmitted by the dichroitic mirror. Two more dichroics are used to guide in (out) the dipole laser. All optics are located outside the vacuum.

shallow trap requiring less laser power), as a lattice photon carries enough energy to cause photo ionization of atoms being in the 3D_J states.

As a consequence, the continuous loading scheme for the dipole trap is applied for a duration of 1 s to 3P_0 atoms, which are afterwards optically pumped to the 3D_2 state and decay to the electronic ground state via 3P_1 . After this, the 1D optical lattice, which is spatially overlapped with the dipole trap, is adiabatically switched on before the dipole trap is rapidly switched off.

3.3.2 Transfer to the optical lattice at 469 nm

The lattice light is generated by a frequency-doubled titanium-sapphire⁸ (Ti:Sa) laser giving 230 mW optical output power at 469 nm, which was an *ab-initio* calculation for the magic wavelength of the clock transition in ^{24}Mg [90]. To generate sufficient laser power for optical trapping of magnesium atoms, the "magic" light needs to be further enhanced to several watts of power using a 1D horizontal build-up cavity passing through the vacuum chamber. The cavity length is stabilized to the incident light field using the PDH technique. The mandatory modulation is applied to the blue laser by means of an electro-optical modulator (EOM) after exiting the commercial SHG stage⁹. The intra-cavity power of the optical lattice is stabilized using a photo diode detecting light leaking out of the optical cavity. A servo loop gives feedback to an AOM before the fiber coupling. After passing all optics, including the AOM and EOM, 160 mW at 469 nm remain for fiber coupling to the vacuum apparatus with an efficiency of $\sim 60\%$.

We use a folded resonator design with a dichroic mirror (469 nm HR, 458 nm HT) for reasons of impedance matching of the cavity (see Figure 3.6). Two more dichroics inside the resonator are used for spatially overlapping the 1064 nm dipole trap with the optical lattice. Reaching a cavity enhancement factor of about 25, we obtain a maximum circulating intra-cavity power of $\sim 2.5\text{ W}$ with 100 mW input power, being mostly limited by the Ti:Sa output power (and degrading pump

⁸TIS-SF-07, Tekhnoscan

⁹SHG Pro, Toptica

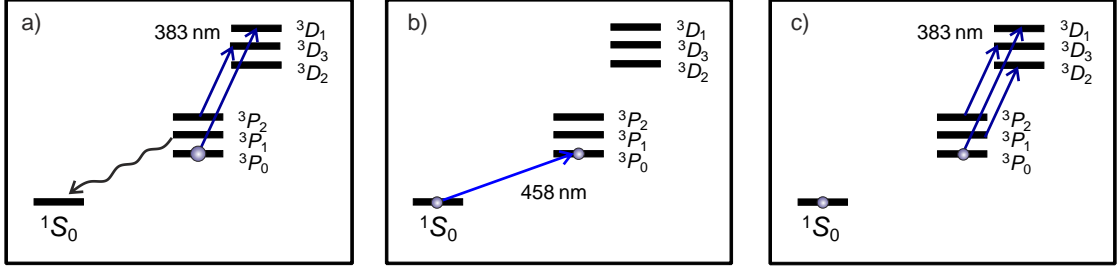


Figure 3.7: Interrogation of the clock transition in ^{24}Mg . (a) Atoms in the 3P_0 state, that have been captured by the optical dipole trap, are optically pumped to the 3D_2 state and decay to the 1S_0 ground state via 3P_1 . (b) Ground state atoms are transferred to the optical lattice and interrogated on the magnetic field enhanced clock transition. (c) The excited state fraction is detected using the triplet-MOT.

laser¹⁰ power, respectively). Together with a lattice waist of $79\ \mu\text{m}$, we achieve a maximum trap depth of about $14.5 E_R$ (or $U/k_B = -26.3\ \mu\text{K}$), where E_R is the recoil energy of a lattice photon.

After the atoms have been transferred from the dipole trap to the optical lattice, we adiabatically ramp down the lattice intensity within 100 ms to a few E_R for removing the hottest atoms out of the trap (purification sequence). Hence, we create the same initial temperature conditions for the atoms in each measurement cycle. Afterwards, the lattice intensity is ramped up again to the final trap depth within 100 ms.

More detailed information on the setup of the lattice laser, the build-up cavity as well as the locking schemes can be found in previous works of our group [66, 91].

3.4 Scheme for a bosonic clock with ^{24}Mg

In the frame of this work, clock spectroscopy is performed starting out with atoms in the 1S_0 ground state followed by laser excitation to 3P_0 (see Figure 3.7). The excited state fraction is detected with the triplet-MOT, as this scheme allows background-free detection of metastable atoms with a sensitivity to a few tens of atoms [57, 65]. So far, normalization of the number of atoms is not executed yet, as the current detection scheme using the CCD camera is too slow¹¹ for taking a second picture of the ground state fraction of atoms, that have not been excited by the clock laser.

In the following, I will briefly discuss the mechanism of magnetic field enhanced spectroscopy together with typical parameters used for the experiments presented in this thesis. This chapter closes with a description of the clock laser setup.

¹⁰Verdi V-10, Coherent

¹¹The camera has a data processing time of approximately 500 ms.

3.4.1 Magnetic field enhanced spectroscopy

If treated as a three-level system, optical dipole excitation of the strongly forbidden $^1S_0 \rightarrow ^3P_0$ clock transition can be enhanced by applying a homogeneous magnetic field that couples the 3P_0 state to 3P_1 with Rabi frequency Ω_B [67]. In addition, the clock laser couples the weakly-allowed dipole transition $^1S_0 \rightarrow ^3P_1$ (natural linewidth is γ) with Rabi frequency Ω_L . The Rabi frequency for dipole excitation of the clock transition is then given by

$$\Omega_{\text{clock}} = \frac{\Omega_L \Omega_B}{\Delta}, \quad (3.2)$$

where Δ is the frequency splitting between 3P_0 and 3P_1 . As a consequence of the magnetic field induced admixture of the 3P_1 state to the excited 3P_0 clock state, as well as power broadening induced by the clock laser intensity I , the forbidden clock transition will feature a linewidth of

$$\gamma_{\text{clock}} \sim \gamma \frac{\Omega_L^2/4 + \Omega_B^2}{\Delta^2}. \quad (3.3)$$

However, this excitation scheme is paid at the expense of a clock laser induced AC Stark shift

$$\Delta_L = \kappa I = \frac{\Omega_L^2}{4\Delta} \quad (3.4)$$

and a second-order Zeeman shift

$$\Delta_B = \beta \mathbf{B}^2 = \frac{-\Omega_B^2}{\Delta}, \quad (3.5)$$

where κ and β are the respective shift coefficients. Combining the constant terms in a prefactor α , Eq. 3.2 turns into

$$\Omega_{\text{clock}} = \alpha \sqrt{I} |\mathbf{B}| \cos \theta, \quad (3.6)$$

where θ denotes the angle between the linearly polarized clock laser field \mathbf{E} and the magnetic field \mathbf{B} .

For increasing the dipole coupling of 1S_0 and 3P_0 , we operate the MOT coils in Helmholtz configuration, as described in Section 2.2. We normally use a magnetic field of 249 G, which yields a predicted linewidth of 8.07 μHz and a Rabi frequency of $\Omega_{\text{clock}}/2\pi = 205 \text{ Hz}$.

3.4.2 The clock laser at 458 nm

Clock spectroscopy is carried out with a home-built ECDL in Littman configuration, stabilized to an ultrastable ULE cavity with finesse $\mathcal{F} \approx 600,000$ at 916 nm,

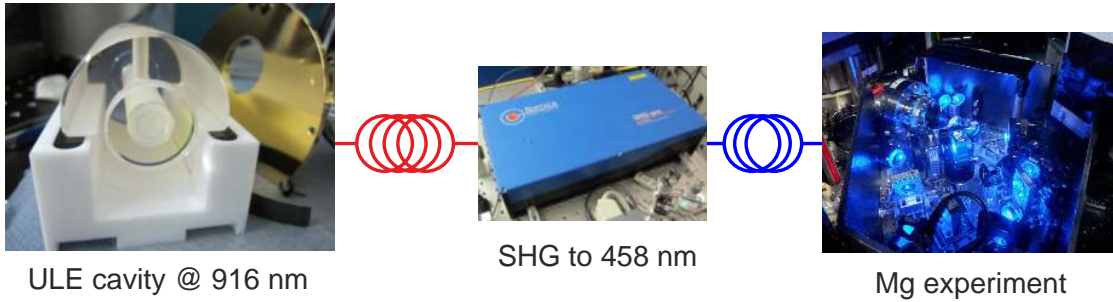


Figure 3.8: Schematic of the clock laser setup. The clock laser is stabilized to a high-finesse ULE cavity at 916 nm. Laser light is fiber-guided from the resonator laboratory to the Magnesium laboratory using a 30 m PM optical fiber link. There, the laser is amplified and frequency-doubled to 458 nm and further fiber-coupled to the experimental apparatus.

similar to [92, 93]. The infra-red light is fiber-guided to the spectroscopy setup, a tapered amplifier chip, and a commercial SHG stage¹² using a PM optical fiber link of 30 m length (see Figure 3.8). The system generates 10 mW of 458 nm light at the position of the atoms. Spectroscopy is performed by irradiating the atoms for 100 ms with a pulsed, Gaussian shaped laser beam that is aligned collinearly with the optical lattice beam. It has a waist of $300\ \mu\text{m}$ and a peak intensity of $7.07\ \text{W}/\text{cm}^2$. Up to 1,000 atoms are resonantly excited to 3P_0 , which are detected with 80 ms of fluorescence from the triplet-MOT. The line center and profile of the atomic transition are obtained by recording the number of excited atoms as the frequency of the 916 nm laser is stepped. Initial drifts of the clock laser are determined via spectroscopy of the clock transition’s carrier frequency and compensated using a feedforward of an AOM that shifts the laser frequency with respect to a resonance of the ultrastable ULE cavity.

¹²SHG pro, Toptica

Theoretical discussion of Lamb-Dicke spectroscopy

From free-space to bound states

The precision in frequency spectroscopy has increased tremendously within the last decades. A valuable measure is the *line quality factor* Q (line- Q) of the atomic transition of choice. As can be seen from Eq. 1.1, $Q = \nu_0/\Delta\nu$ is defined as the ratio of the resonance frequency ν_0 and the observed full width at half-maximum (FWHM) linewidth $\Delta\nu$ [35]. As Eq. 1.1 suggests, the smaller the Allan deviation of a frequency standard, the more stable it is, the ultimate goal of spectroscopy is to increase the line- Q as much as possible. The first big step towards a large Q has been made by choosing optical transitions for spectroscopy, rather than microwave transitions, therefore automatically increasing the Q by at least four orders of magnitude simply due to the higher resonance frequency ν_0 . As this, at some point, cannot be increased further, one has to start reducing the transition linewidth $\Delta\nu$.

As mentioned in Section 2.1, atoms are usually prepared in an oven, where solid materials have to be sublimated. Hence, the atomic vapor exiting the oven is often more than 600 K hot, thus facing an enormous Doppler broadening on each atomic transition (see Eq. 3.1). However, in early experiments on optical clocks, people overcame this problem by collimating the atomic vapor to a thermal beam traveling in just one direction of space. As the atomic resonance frequency is Doppler-shifted ($\delta\nu_D \sim \mathbf{k}\mathbf{v}$) only for laser interrogation having a component $\mathbf{k} = (k_x, k_y, k_z)$ along the direction of atomic velocity, this shift goes to zero if the atoms are probed transversely. Unfortunately, the interaction time between the applied interrogation laser and the atoms is finite, as the atomic beam is continuously traveling. Thus, the corresponding frequency spectrum shows a finite homogeneous FWHM

linewidth $\sim 0.9/\tau$ [94]. The implementation of a Ramsey sequence [4] or, similarly, a Ramsey-Bordé interferometer in the optical domain [95] lifts the requirement on long interrogation times as the single pulse has been replaced by interaction zones.

The first frequency measurement of the $^1S_0 \rightarrow ^3P_1$ transition in ^{24}Mg has been carried out on a thermal beam of magnesium atoms being probed in a Ramsey-Bordé sequence [56]. The achieved uncertainty of this measurement was 2.5×10^{-12} being limited by residual first-order Doppler effects. After the successful demonstration of laser cooling at 285 nm [96, 97], the same frequency measurement could be repeated for laser-cooled atoms featuring a total uncertainty of 7×10^{-14} (or 47 Hz in absolute values, respectively) [57]. As the atoms are transversely probed during free-fall, it is the imperfection of the clock laser's wavefront curvatures and a mismatch of the beams themselves as well as power imbalances, that still induce a residual Doppler shift on the clock transition frequency. As this was, in our case and also in other experiments [98, 99], the limiting contribution to the clock uncertainty budget, the question was, how to eliminate the first-order Doppler effect for further improvement of the clock accuracy.

Scattering in free-space

As the most relevant process in optical clock spectroscopy is the optical pumping itself, I will briefly specify the significant aspects in free-space interrogation and the resulting limitations. In principle, optical pumping always comes along with a change in temperature of a specific degree of freedom in the atom, that can either be heating or cooling: For each scattering event, the atom receives a momentum kick $\hbar\mathbf{k}$ during absorption. Accordingly, this will lead to a change of atomic velocity $\Delta\mathbf{v} \cong \hbar\mathbf{k}/m_a$, where m_a is the atomic mass [100]. The atomic absorption and emission frequencies are given through

$$\omega_{\text{abs}} = \omega_0 + \mathbf{k}_{\text{abs}}\mathbf{v} - \frac{1}{2}\omega_0\beta^2 + E_{\text{Rec}}/\hbar, \quad (4.1)$$

$$\omega_{\text{em}} = \omega_0 + \mathbf{k}_{\text{em}}\mathbf{v}' - \frac{1}{2}\omega_0\beta^2 - E_{\text{Rec}}/\hbar. \quad (4.2)$$

Here, $\omega_0 = 2\pi\nu_0$, $|\mathbf{k}_{\text{abs}}| = \omega_{\text{abs}}/c$, $|\mathbf{k}_{\text{em}}| = \omega_{\text{em}}/c$, \mathbf{v} (\mathbf{v}') is the atomic velocity in the ground (excited) state, $\beta = |\mathbf{v}|/c$ and $E_{\text{Rec}} = (\hbar k)^2/2m_a$ is the photon recoil energy. The second term on each right-hand side of above equations is the first-order Doppler shift, the third term is the second-order Doppler shift (also referred to as *time dilation shift*) and the last one is the recoil shift. In the following, the situation shall be treated in the non-relativistic approximation, therefore the second-order Doppler term may be neglected. Furthermore, it is well known that spontaneous emission has a random direction [101], thus, by averaging over all possible directions, the first-order Doppler term in Eq. 4.2 may also be excluded.

The average change in energy of a photon per resonant spontaneous scattering event results to the difference of above equations [100]:

$$\Delta E_{\text{photon}} = \hbar(\omega_{\text{em}} - \omega_{\text{abs}}) = -\hbar\mathbf{k}_{\text{abs}}\mathbf{v} - 2E_{\text{Rec}}. \quad (4.3)$$

As energy and momentum have to be conserved in the overall process, the atom will feel a change in kinetic energy according to

$$\Delta E_{\text{atom}} = -\Delta E_{\text{photon}} = \hbar\mathbf{k}_{\text{abs}}\mathbf{v} + 2E_{\text{Rec}}. \quad (4.4)$$

Drawing a first conclusion, free-space scattering is always related to changes in the atom's kinetic energy. Even at zero velocity, the atom's energy at least has to change by the recoil energy.

Recoil-free scattering in the Lamb-Dicke regime

Facing the fact that the Doppler effect directly results from the recoil momentum, R. H. Dicke postulated in 1953 a recoil-free regime for spectroscopy, if the atom could be confined to a region with spatial extent being smaller than the confining wavelength λ [26].

Here, he assumed atoms to be confined in a 1D square potential of width a . From quantum mechanical point of view, any atom hence possesses two types of energy: *internal energy* (corresponding to the internal electronic states) and *external energy*, which is the quantized vibrational energy of the atom's center-of-mass motion in the potential. If the atom undergoes a transition as a consequence of photon absorption or emission, both the internal and external states may change. The photon frequency can hence be written as

$$\nu_{nm} = \nu_0 + [h/(8m_a a^2)](n^2 - m^2), \quad (4.5)$$

with n and m being integer numbers, indicating the vibrational states. Now, two facts have to be considered: First, vibrational states will always be present as long as the confining potential is alive. Second, as the atom possesses thermal energy, several atomic energy levels may be occupied due to a Maxwell-Boltzmann distribution, hence a frequency spectrum with several lines ν_{nm} can be observed. Only for low zero-point energies ($\ll k_B T$, see Subsection 4.1.1) of atomic oscillation in the potential well, the degenerate frequency $\nu = \nu_{nn}$ is emitted with highest intensity.

Coming back to the original idea of R. H. Dicke to create a recoil-free regime for spectroscopy, he gives the probability for the photon recoil to interact with the potential wall, rather than with the atom (see Eq. 4.4), as follows [26]:

$$\frac{\sin^2(\pi a/\lambda)}{(\pi a/\lambda)^2}. \quad (4.6)$$

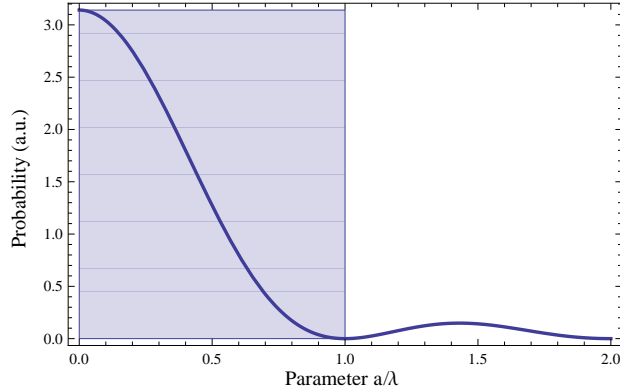


Figure 4.1: Illustration of the Lamb-Dicke regime. The probability for the photon recoil to be absorbed by the potential, rather than by the atom, is plotted as a function of the parameter a/λ . If the confining potential is of smaller extent than the wavelength λ , the probability is enhanced that excitation of external atomic motion is suppressed (shaded region).

Figure 4.1 illustrates this probability as a function of the parameter a/λ . If the potential width is smaller than the wavelength λ , photon recoils tend to be absorbed very likely by the potential walls. An intuitive understanding for this fact is given by comparing the vibrational frequency in Eq. 4.5 with the photon's recoil frequency, which is the further above introduced recoil energy E_{Rec} reduced by Planck's constant h :

$$h/(8m_a a^2) = h/(2\lambda^2 m_a).$$

If we want the probe photon not to excite vibrational states of the atom, the vibrational frequency has to be larger than the photon recoil frequency, thus the potential width has to fulfill the condition $a < \lambda/2$. This particular regime has been named the *Lamb-Dicke regime*.

Early experiments on trapped particles in the Lamb-Dicke regime have been performed on the $^{198}\text{Hg}^+$ ion at NIST in the group of D. J. Wineland [27]. The trapping potential provided by the Paul trap is in good approximation with that of a harmonic oscillator [102]. Wineland and co-workers have created a broad framework of theory and experiments concerning Lamb-Dicke spectroscopy, I will mainly refer to in the following section. Understanding the importance of this framework, it is no surprise that D. J. Wineland has been awarded the Nobel Prize in physics in 2012 "for ground-breaking experimental methods that enable measuring and manipulation of individual quantum systems" [5].

The first optical clock was the $^{199}\text{Hg}^+$ ion clock at NIST [24]. Having again a look at Eq. 1.1, although single-ion clocks feature a poor S/N ratio, they definitely benefit from long storage times lasting up to several days. But is there any perspective for neutral-atom frequency standards featuring a large ensemble of N atoms on the one hand and spectroscopy in the Lamb-Dicke regime on the other?

It was already known that neutral atoms can be trapped in so-called *optical lattices* [30], a configuration of retro-reflected laser beams causing the dipole potential to interfere. The result is a "box of eggs-like" potential (see a detailed discussion on this in Sec. 4.2). H. Katori and co-workers were the first to demonstrate Lamb-Dicke spectroscopy on laser-cooled Sr atoms being trapped in such an optical lattice [31]. However, this dipole potential usually causes a large differential AC Stark shift on the clock transition frequency as the polarizabilities of the clock states differ. Nevertheless, atomic polarizabilities are wavelength-dependent. It was also H. Katori suggesting in 2003 to use an "*engineered light shift trap*" for the atoms [32], where the differential AC Stark shift vanishes at a particular lattice wavelength. That was the hour of birth of the *magic wavelength optical lattice clock*.

This chapter is structured as follows: In Sec. 4.1, I will discuss the basic features of Lamb-Dicke spectroscopy in an ideal harmonic potential. Sec. 4.2 treats lattice-based Lamb-Dicke spectroscopy. As in reality, potential depths are finite, several effects influencing clock spectroscopy will be discussed, in particular the tunneling-related Doppler effect on the spectroscopy signal, as referred to in Sec. 4.3.

4.1 Lamb-Dicke spectroscopy in harmonic confinement

4.1.1 Preparing the quantum mechanical tools

The harmonic oscillator is probably one of the purest systems in quantum mechanics and a good approximation of the trapping regime described in the previous section. The center-of-mass motion of a harmonically bound atom is described by the following Hamilton operator

$$\hat{H} = \frac{\hat{p}^2}{2m_a} + \frac{m_a \omega^2 \hat{x}^2}{2}, \quad (4.7)$$

where ω is the oscillator's frequency and \hat{p} and \hat{x} are the momentum and position operators, respectively. Introducing non-Hermitian and adjoint operators \hat{a} and \hat{a}^\dagger as a function of \hat{p} and \hat{x} , the above Hamiltonian transforms into

$$\hat{H} = \hbar\omega \left(\hat{n} + \frac{1}{2} \right), \quad (4.8)$$

with \hat{n} being the *number operator* $\hat{n} = \hat{a}^\dagger \hat{a}$. In return, the position and momentum operators are given by

$$\hat{x} = x_0(\hat{a} + \hat{a}^\dagger), \quad \hat{p} = -ix_0 m_a \omega (\hat{a} - \hat{a}^\dagger), \quad (4.9)$$

with the zero-point amplitude $x_0 = \sqrt{\hbar/(2m_a\omega)}$ (similarly for y and z) [100, 103]. Suppose $|n\rangle$ being an eigenstate of the number operator, the following equations can be proven to be valid:

$$\hat{n}|n\rangle = n|n\rangle, \quad \langle n|m\rangle = \delta_{n,m}, \quad (4.10)$$

$$\hat{a}^\dagger|n\rangle = \sqrt{n+1}|n+1\rangle, \quad (4.11)$$

$$\hat{a}|n\rangle = \sqrt{n}|n-1\rangle. \quad (4.12)$$

Eqs. 4.11 and 4.12 visualize, why \hat{a}^\dagger and \hat{a} are called the *raising* and *lowering* operators. According to Eq. 4.8, $|n\rangle$ is not only an eigenstate of the number operator \hat{n} , it is furthermore an eigenstate of the Hamilton operator of the harmonic oscillator. Following the Schrödinger equation

$$\hat{H}|n\rangle = E_n|n\rangle, \quad (4.13)$$

directly gives the eigenenergies

$$E_n = \hbar\omega \left(n + \frac{1}{2} \right), \quad n = 0, 1, 2, \dots \quad (4.14)$$

of the quantum harmonic oscillator, which is a discrete energy spectrum of vibrational states with equidistant separation $\hbar\omega$. In the classical treatment, the harmonic oscillator (being a spring feather or a pendulum) will have its lowest energy at rest

$$E = 0, \quad p = 0, \quad x = x_0,$$

while in the quantum mechanical treatment, the *zero-point energy* is different from zero [100, 103]:

$$E_0 = \frac{\hbar\omega}{2}. \quad (4.15)$$

This fact suggests a pure quantum mechanical treatment of bound atoms in harmonic confinement. Doing so, the following assumptions will now be made [100]:

- (i) Atoms are harmonically bound in all three dimensions with oscillation frequencies ω_x , ω_y and ω_z with $\omega_i \ll \omega_0$ for $i = x, y, z$. In the following, I will restrict myself to the z direction, as for the remaining ones the situation can be deduced analogously.
- (ii) Motion in these three dimensions is independent from each other.
- (iii) The time required for the atomic kinetic energy to thermalize with the outside environment is extremely long (equivalent to a long vacuum-limited life time).

- (iv) The internal atomic level structure features a two-level system with $E_e - E_g \ll k_B T$, where E_e (E_g) is the excited (ground) state energy.
- (v) The relaxation rate γ (natural linewidth) of the excited state shall be small compared to the trap frequencies: $\gamma \ll \omega_i$.
- (vi) Incident radiation interacting with the atoms is highly monochromatic (spectral width $\ll \gamma$) and its intensity is well below the saturation level of the transition.
- (vii) The total Hamilton operator of the system is composed of a free Hamiltonian \hat{H}_0 and an interaction Hamiltonian \hat{V} : $\hat{H} = \hat{H}_0 + \hat{V}$ (interaction transformation) [104].

4.1.2 Atom-light interaction in harmonic confinement

If an incident plane wave, that is irradiated along the z axis with $|\mathbf{k}| = k_z$, interacts with an atom being confined according to the assumptions of the previous subsection, the atom will see the light in its own rest frame with

$$\mathbf{E} = \mathbf{E}_0 \sin(kz - \omega t), \quad (4.16)$$

where z is the atomic position coordinate and k and ω are the wave vector and frequency of the incident light field. As the atom is bound in a potential, its position z will oscillate with

$$z = z_a \sin(\omega_z t + \phi_z), \quad (4.17)$$

with z_a being the oscillation amplitude and ϕ_z is a phase factor. Setting $\phi_z = 0$ and combining Eqs. 4.16 and 4.17, results in

$$\mathbf{E} = \mathbf{E}_0 \sin[kz_a \sin(\omega_z t) - \omega t]. \quad (4.18)$$

The atom will see the incident light field being frequency modulated at frequency ω_z with modulation index kz_a [100]. Eq. 4.18 can be expanded into a series of Bessel functions $J_m(kz_a)$ featuring a radiation spectrum of equidistant lines (see Fig. 4.2). In tight confinement, the spectral feature on resonance $\omega = \omega_0$ will have the highest intensity. Here, assumption (v) of Subsection 4.1.1 plays an important role: as the linewidth γ of the excited state is much smaller than the trap frequency ω_z , the sidebands are clearly resolved and could be addressed with a narrow-line laser. Hence, this situation is called the *strong binding regime* or the *resolved sideband regime* [28].

For the quantum mechanical treatment, the total Hamiltonian of the system (assumption (vii)) can be re-written as

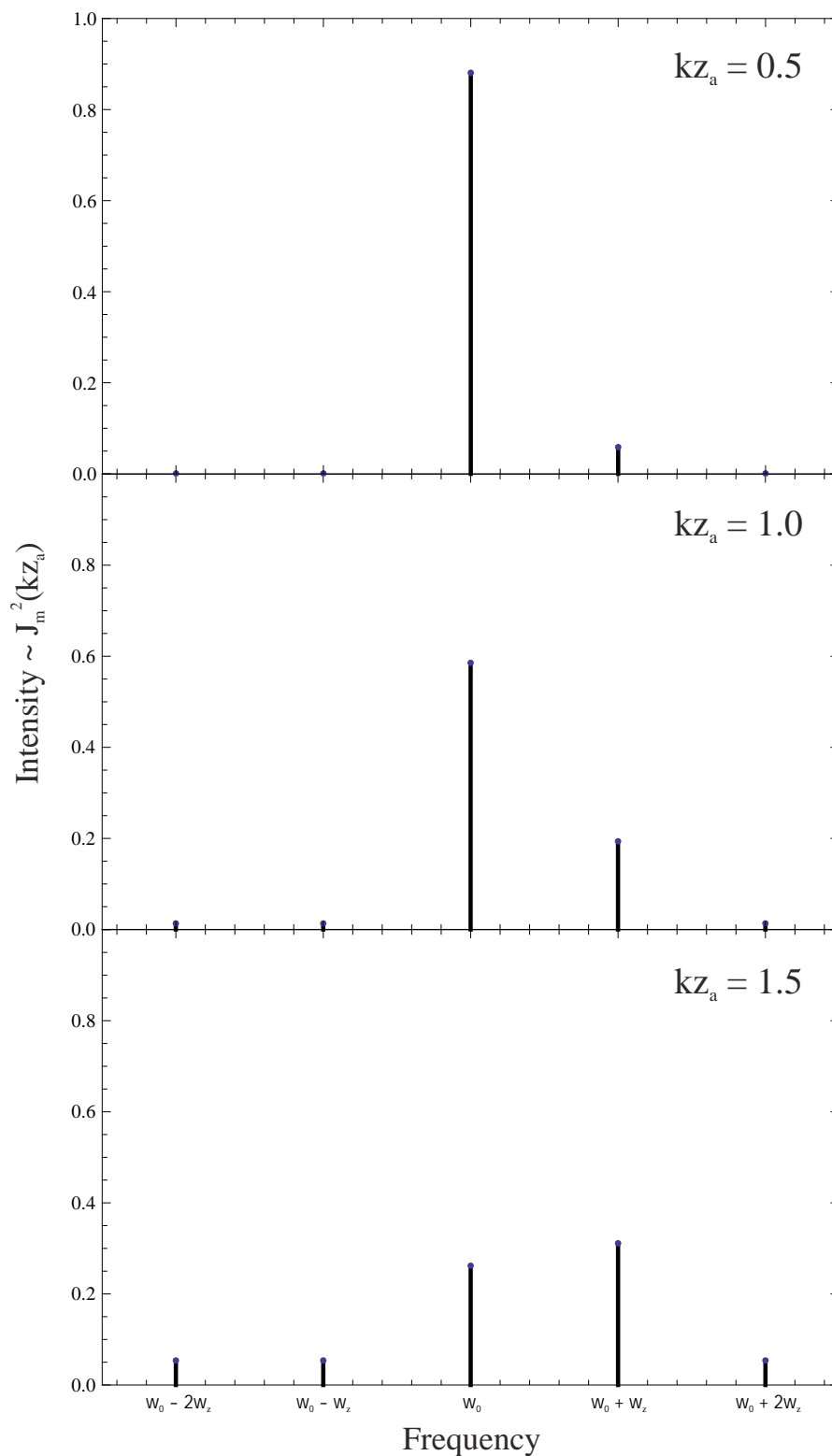


Figure 4.2: The radiation spectrum in harmonic confinement features a carrier transition on resonance $\omega = \omega_0$ and multiple sidebands separated by $m\omega_z$ ($m = \pm 1, \pm 2, \dots$). The smaller the modulation index kz_a , the more the sideband intensities will be suppressed featuring a higher carrier intensity.

$$\hat{H} = \hat{H}^{(m)} + \hat{H}^{(e)} + \hat{H}^{(\text{int})}, \quad (4.19)$$

with $\hat{H}_0 = \hat{H}^{(m)} + \hat{H}^{(e)}$ and $\hat{V} = \hat{H}^{(\text{int})}$. $\hat{H}^{(m)}$ is the motional Hamilton operator along a certain trap axis as given by Eq. 4.8. $\hat{H}^{(e)}$ describes the internal two-level structure of the atom and is of the form

$$\hat{H}^{(e)} = \hbar \frac{\omega_0}{2} (|e\rangle \langle e| - |g\rangle \langle g|), \quad (4.20)$$

where $\omega_0 = \omega_e - \omega_g$ [104]. The interaction Hamiltonian is given by

$$\hat{H}^{(\text{int})} = \hbar \frac{\Omega}{2} (|e\rangle \langle g| e^{ik\hat{z}} + H.c.), \quad (4.21)$$

where Ω is the Rabi frequency of the atomic transition [102]. As it has already been mentioned in the introduction of this chapter, absorption and emission of photons is related with momentum kicks $\hbar k_z$ acting on the atomic momentum. This effect is now described via the operators $e^{\pm ik\hat{z}}$. Written in the basis of vibrational states $|n\rangle$, this is equivalent to transitions $|n\rangle \rightarrow |m\rangle$, whose probability amplitudes are defined through the Franck-Condon factors

$$F_{n \rightarrow m} = |\langle m | e^{ik\hat{z}} | n \rangle|. \quad (4.22)$$

This means [102], a given ground state $|g, n\rangle$ will be coupled to several excited states $|e, m\rangle$ with Rabi frequencies $\Omega F_{n \rightarrow m}$ and transition frequencies

$$\omega_{m-n} = \omega_0 + (m - n)\omega_z. \quad (4.23)$$

Using the expression of the position operator in Eq. 4.9, above transition's Rabi frequencies can be written as [100, 105]

$$\Omega_{n,m} = \Omega F_{n \rightarrow m} = \Omega |\langle m | e^{ik\hat{z}} | n \rangle| = \Omega |\langle m | e^{ikz_0(\hat{a} + \hat{a}^\dagger)} | n \rangle|, \quad (4.24)$$

Here, $\eta = kz_0$ is the *Lamb-Dicke parameter*. Confinement in the Lamb-Dicke regime is given for the criterion $\eta \ll 1$, hence

$$\eta = kz_0 = k\sqrt{\hbar/(2m\omega_z)} = \sqrt{E_{\text{Rec}}/(\hbar\omega_z)} = \sqrt{\omega_{\text{Rec}}/\omega_z} \ll 1, \quad (4.25)$$

or, equivalently, $\omega_{\text{Rec}} \ll \omega_z$ putting a constraint on the required trap depth in comparison to the recoil frequency of the probe light (see introduction to this chapter). This means in particular, the exponential function in Eq. 4.24 may be Taylor-expanded in first order as $e^{i\eta} \simeq 1 + i\eta$ [106], giving

$$\begin{aligned} \Omega_{n,m} &\simeq \Omega |\langle m | 1 + i\eta(\hat{a} + \hat{a}^\dagger) | n \rangle| \\ &= \Omega [|\langle m | 1 | n \rangle| + \eta (|\langle m | \hat{a} | n \rangle| + |\langle m | \hat{a}^\dagger | n \rangle|)]. \end{aligned} \quad (4.26)$$

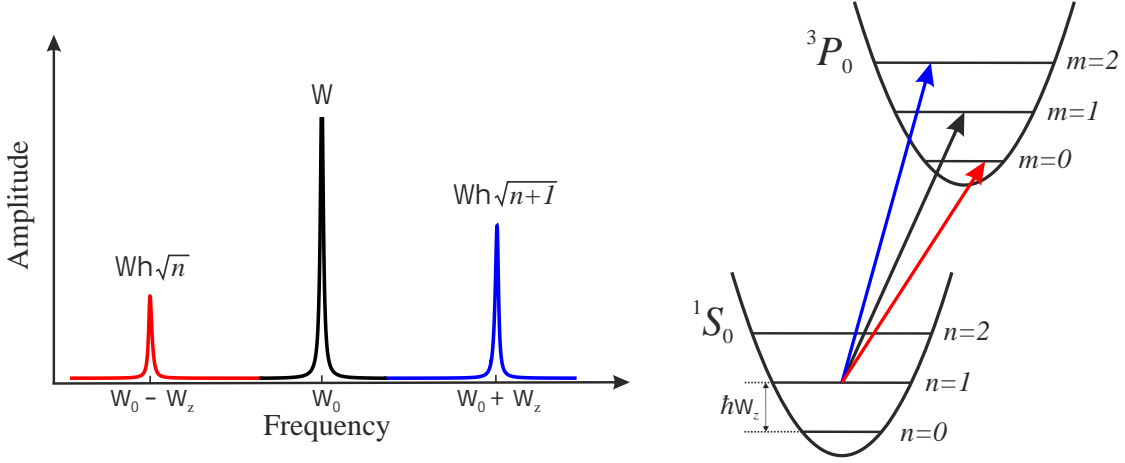


Figure 4.3: Possible transitions in the Lamb-Dicke regime. (Left) The expected frequency spectrum features a strong carrier transition and sidebands being separated from the first by the trap frequency ω_z . Due to the transition strengths, the first blue sideband is of larger amplitude than the first red sideband. (Right) Scheme of the harmonic potential of the ground and excited states of the clock transition. Optical excitation can be purely internal or include a change in the motional quantum number. In both pictures, the carrier transition is indicated in black, as well as the red and the blue sidebands in their respective colors.

Using Eqs. 4.10, 4.11 and 4.12, as well as operating to the right, this expression further simplifies to

$$\Omega_{n,m} \simeq \Omega(\delta_{m,n} + \eta\sqrt{n}\delta_{m,n-1} + \eta\sqrt{n+1}\delta_{m,n+1}). \quad (4.27)$$

Due to the nature of the Kronecker delta, it is clearly visible that only one term will survive during each transition $|n\rangle \rightarrow |m\rangle$, hence the following types of transitions are of particular interest: those, being purely internal without influencing the motional quantum number ($m = n$), are called *carrier* transitions. Resonances with $m = n - 1$ are called the *first red sideband*, contrary, transitions increasing the motional quantum number ($m = n + 1$) are called the *first blue sideband* [104]. According to Eq. 4.27, their Rabi frequencies are given by

$$\Omega_{n,n} = \Omega, \quad (4.28)$$

$$\Omega_{n,n-1} = \Omega\eta\sqrt{n}, \quad (4.29)$$

$$\Omega_{n,n+1} = \Omega\eta\sqrt{n+1}. \quad (4.30)$$

Figure 4.3 summarizes the features of transitions $|n\rangle \rightarrow |m\rangle$ if atoms are localized in the Lamb-Dicke regime. The left part shows the expected frequency spectrum with the carrier transition (black curve) and the resolved sidebands (red and blue curves) being separated from the carrier by the trap frequency ω_z . This plot also demonstrates that the blue sideband has a slightly stronger amplitude

than the red sideband, which is a consequence of Eqs. 4.29 and 4.30. The right part of Figure 4.3 shows the harmonic potential with bound states for each the ground and the excited state of the clock transition. The carrier is indicated with a black arrow, the red and blue sidebands in their respective colors. In principle, above described transitions are possible starting from every bound state being occupied. One exception is the absolute ground state $n = 0$ featuring only a carrier transition and a blue sideband.

So far, $|n\rangle \rightarrow |m\rangle$ transitions have been treated for the Lamb-Dicke criterion being satisfied and Eq. 4.26 was obtained throughout a first-order Taylor expansion of Eq. 4.24. Coming to the end of this subsection, I would like to comment on the more general situation with η being arbitrary. Using the appropriate operator formalism¹, the exponential function in Eq. 4.24 turns into

$$e^{i\eta(a+a^\dagger)} = e^{-\frac{1}{2}\eta^2} e^{i\eta\hat{a}^\dagger} e^{i\eta\hat{a}},$$

hence

$$\Omega_{n,m} = \Omega e^{-\frac{1}{2}\eta^2} |\langle m | e^{i\eta\hat{a}^\dagger} e^{i\eta\hat{a}} | n \rangle|. \quad (4.31)$$

As $\hat{a}^l |n\rangle = \sqrt{n!/(n-l)!} |n-l\rangle$, the exponential function expressed in its Taylor series acts like

$$e^{i\eta\hat{a}} |n\rangle = \sum_{l=0}^{\infty} \frac{(i\eta)^l}{l!} \sqrt{\frac{n!}{(n-l)!}} |n-l\rangle. \quad (4.32)$$

Operating in Eq. 4.31 to the right with $e^{i\eta\hat{a}}$ and to the left with $e^{i\eta\hat{a}^\dagger}$ results to

$$\Omega_{n,m} = \Omega e^{-\frac{1}{2}\eta^2} \sqrt{\frac{n!}{m!}} (i\eta)^{\Delta n} \sum_{l=0}^{n_{<}} \frac{(-1)^l \eta^{2l}}{l!(l+\Delta n)!(n_{<}-l)!}, \quad (4.33)$$

with $\Delta n = |m-n|$ and $n_{<}$ is the lesser of n and m [100]. Finally, using the expression for the generalized Laguerre polynomial,

$$L_n^\alpha(X) = \sum_{l=0}^n (-1)^l \binom{n+\alpha}{n-l} \frac{X^l}{l!},$$

the generalized Rabi frequency becomes

$$\Omega_{n,m} = \Omega |\langle m | e^{ik\hat{z}} | n \rangle| = e^{-\frac{1}{2}\eta^2} (i\eta)^{\Delta n} \sqrt{\frac{n_{<}!}{(n_{<}+\Delta n)!}} L_{n_{<}}^{\Delta n}(\eta^2). \quad (4.34)$$

¹ $e^{A+B} = e^A e^B e^{-[A,B]/2}$

4.1.3 Deduction of atomic temperature

For trapped atoms, the minimum kinetic energy is often given in terms of the mean occupation number $\langle n \rangle$ of the harmonic oscillator state. If the atoms are at temperature T , one can assume $\langle n \rangle$ to be Boltzmann distributed:

$$\langle n \rangle = 1/(e^{\hbar\omega_z/(k_B T)} - 1). \quad (4.35)$$

If $\langle n \rangle \ll 1$, the atom's energy in the potential well equals $\hbar\omega/2$, the zero-point energy [104, 106]. In the Lamb-Dicke limit, $\langle n \rangle = \sqrt{n}$, hence, the amplitude ratio of the first blue and red sidebands is given by $(\langle n \rangle + 1)/\langle n \rangle$. Using Eq. 4.35, the temperature T of atoms is given by

$$T = \frac{\hbar\omega_z}{k_B} \ln \left(\frac{\langle n \rangle + 1}{\langle n \rangle} \right)^{-1}. \quad (4.36)$$

In the experiment, the temperature can be measured by recording the frequency spectrum ranging from the first red to the first blue sideband, giving rise to the trap frequency ω_z and the ratio of the sideband amplitudes.

4.2 Lamb-Dicke spectroscopy in a 1D optical lattice

In this section, I will turn to more "realistic", optical potentials as they occur in experiments on optical lattice clocks. "Realistic" in essence means here that potential wells are not of infinite depth, hence, the ideal situation of a harmonic potential with equidistant energy levels does not fully apply to the potential of an optical lattice. Nevertheless, the harmonic oscillator still is a valid approximation for the coldest atoms occupying the ground state of the trap. This section is structured as follows: First, I will give the potential of an optical lattice featuring the main characteristics important for Lamb-Dicke spectroscopy in Subsection 4.2.1. In an optical lattice, several effects may cause inhomogeneities on the spectroscopy signal. In Subsection 4.2.2, lattice wavelength dependent inhomogeneities are treated and the term of the magic wavelength is derived. Subsection 4.2.3 deals with inhomogeneities induced by atomic motion.

4.2.1 The optical lattice potential

An optical lattice is a *standing-wave trap*, in the 1D simplest case formed by a retro-reflected laser beam conserving the wave front curvatures and beam polarization [107]. If the beam is directed along the z axis, the lattice potential is given by

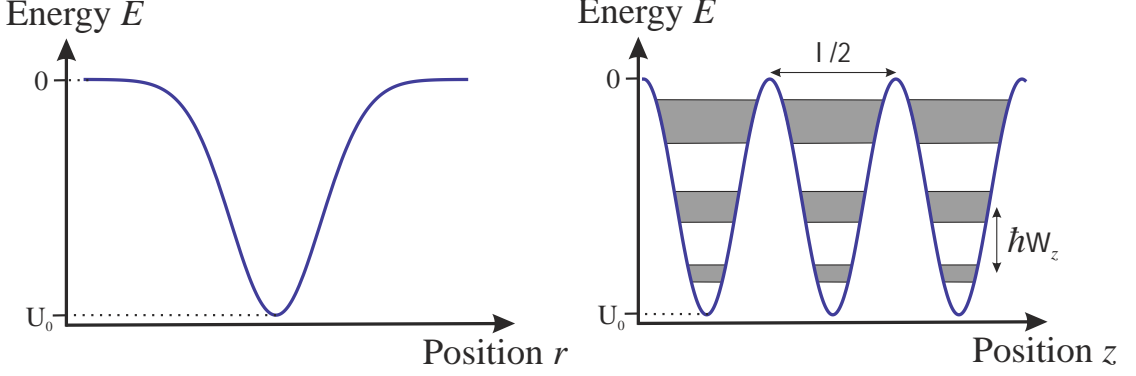


Figure 4.4: Optical lattice potential. In the radial direction, the atoms exhibit a weak confinement occurring due to the Gaussian trapping beam (*left*), whereas the axial confinement is much stronger, typically in the Lamb-Dicke regime (*right*). Grey-shaded parts indicate the presence of vibrational bands rather than states, as a consequence of finite well depths.

$$U(z, r) = -U_0 \cos^2(k_L z) e^{-2r^2/w_0^2}, \quad (4.37)$$

$$U_0 = 4\alpha(\lambda_L)P/(\pi c \epsilon_0 w_0^2), \quad (4.38)$$

where U_0 is the well depth as a function of atomic polarizability $\alpha(\lambda_L)$, P and w_0 are the lattice power and waist [108]. $r = \sqrt{x^2 + y^2}$ denotes the radial distance from the lattice axis, z is the axial position coordinate and $k_L = 2\pi/\lambda_L$ is the lattice wave number [109]. One can see from Eq. 4.37 and Figure 4.4 (*right*), the lattice potential is of period $\lambda_L/2$. Hence, atoms are strongly confined in the axial direction of the lattice, being trapped in the "pancake-shaped" anti-nodes, but exhibit a weak confinement in the radial direction which is related to the Gaussian profile of the lattice beam (Figure 4.4, *left*).

As the single site potential is not separable into independent coordinates, Blatt *et al.* [109] introduce a quartic distortion while approximating the axial trapping potential as a 1D harmonic oscillator. Taylor series expansion of both functions in Eq. 4.37 in first order gives

$$U(z, r) \simeq U_0 \left(-1 + k_L^2 z^2 + \frac{2}{w_0^2} r^2 - \frac{k_L^4 z^4}{4} - \frac{2k_L^2}{w_0^2} r^2 z^2 \right). \quad (4.39)$$

First-order perturbation theory guides them to eigenstates $|n\rangle = |n_x, n_y, n_z\rangle$ with energy spectrum

$$E_n/\hbar \simeq \omega_z \left(n_z + \frac{1}{2} \right) + \omega_r (n_x + n_y + 1) - \frac{\omega_R}{2} \left(n_z^2 + n_z + \frac{1}{2} \right) - \omega_R \frac{\omega_r}{\omega_z} (n_x + n_y + 1) \left(n_z + \frac{1}{2} \right), \quad (4.40)$$

introducing the axial and radial trap frequencies from the harmonic approximation as

$$\omega_z = 2\omega_R \sqrt{\frac{U_0}{E_R}} \quad (4.41)$$

and

$$\omega_r = \sqrt{\frac{U_0}{m_a \pi^2 \omega_0^2}}. \quad (4.42)$$

Here, ω_R and E_R are the lattice recoil frequency and energy, respectively. Unlike the ideal situation of a harmonic oscillator, where the axial frequency spectrum is given by Eq. 4.23, the quartic distortion of the lattice potential leads to an axial frequency separation of

$$\begin{aligned} \gamma(n_z) &= (E_{n_x, n_y, n_z+1} - E_{n_x, n_y, n_z})/\hbar \\ &= \omega_z - \omega_R(n_z + 1) - \omega_R \frac{\omega_r}{\omega_z} (n_x + n_y + 1). \end{aligned} \quad (4.43)$$

As $\omega_r \ll \omega_z$, typically by almost three orders of magnitude, the third term in above Eq. 4.43 is negligible for ground state transitions. The measured axial trap frequency is then $\gamma(n_z)/2\pi \approx (\omega_z - \omega_R)/2\pi$ instead of the expected $\omega_z/2\pi$ [109].

4.2.2 Excitation inhomogeneities I - The magic wavelength

If atoms are exposed to a trapping light field with electric field amplitude \mathcal{E} , their transition energy can be written as

$$\hbar\omega = \hbar\omega_0 - \frac{1}{4}\Delta\alpha(\mathbf{e}, \omega_L)\mathcal{E}^2 - \frac{1}{64}\Delta\gamma(\mathbf{e}, \omega_L)\mathcal{E}^4 - \mathcal{O}(\mathcal{E}^6), \quad (4.44)$$

where $\Delta\alpha$ and $\Delta\gamma$ are the differential AC polarizability and hyperpolarizability of the clock states, respectively, and \mathbf{e} is the unit polarization vector of the light field [32].

As the atomic polarizability is wavelength-dependent, it is obvious to choose a particular, "magic" lattice wavelength satisfying $\Delta\alpha(\mathbf{e}, \omega_L) = 0$, as the polarizabilities of the two clock states cancel each other. For completeness, the AC polarizability consists of the electric dipole polarizability α_{E1} , the magnetic dipole polarizability α_{M1} and the electric quadrupole polarizability α_{E2} :

$$\alpha(\mathbf{e}, \omega_L) = \alpha_{E1}(\mathbf{e}, \omega_L) + \alpha_{M1}(\mathbf{e}, \omega_L) + \alpha_{E2}(\mathbf{e}, \omega_L), \quad (4.45)$$

where α_{E1} clearly is the dominant effect for light-induced energy displacements of the atomic states.

Depending on which transition has been chosen as clock transition, its magic wavelength can have a different value. In ^{24}Mg , the $^1S_0 \rightarrow ^3P_1$ ($m_J = 0$) and $^1S_0 \rightarrow ^3P_0$ are possible clock transitions. Focusing on the latter one, offering the

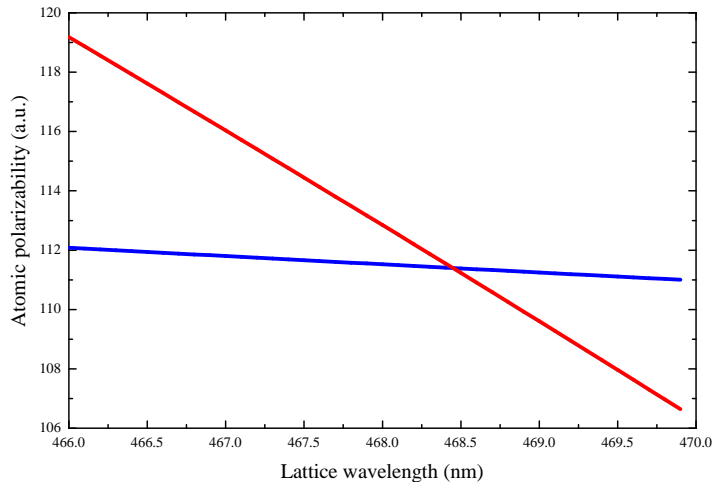


Figure 4.5: Polarizabilities of the clock states in magnesium as a function of lattice wavelength. The 3P_0 polarizability (red curve) crosses the 1S_0 polarizability (blue curve) at 468.45(23) nm, fulfilling the condition for the magic wavelength. Polarizabilities are given in atomic units having the dimension of volume in units of a_0^3 , where a_0 is the Bohr radius. The conversion factor to SI units is given by $4\pi\epsilon_0 a_0^3$ [110].

larger line- Q and being independent on lattice light polarization, there have been several theoretical predictions on the value of the magic wavelength ranging from 432 to 470 nm [64, 71, 111–113]. The most recent calculation has been performed using two different methods: The first uses state-of-the-art relativistic approach combining configuration interaction (CI) and all-order linearized coupled-cluster methods (CI+all-order) [110]. Furthermore, the magic wavelength has been estimated via combination of CI with second-order many-body perturbation theory (CI+MBPT), not including all-order corrections to the effective Hamiltonian, but using experimental atomic parameters instead of theoretical ones. Using this refined model, the magic wavelength of the $^1S_0 \rightarrow ^3P_0$ clock transition in ^{24}Mg is estimated to be 468.45(23) nm, where the uncertainty is given by the difference of the above method's values. Figure 4.5 shows the calculated atomic polarizabilities as a function of lattice wavelength with crossing point at the magic wavelength. The estimated magic wavelength is red-detuned compared to relevant resonances that introduce a light shift and the lattice therefore is an attractive potential. Higher-order light-induced energy perturbations of the clock states are unpreventable, as the atoms are trapped in the anti-nodes of the lattice with highest intensity [17].

However, a more crucial effect arises, if the optical lattice is not exactly tuned to the magic wavelength. The result will be an energy mismatch for carrier transitions $\Omega_{n,m}$ ($n = m = 0, 1, 2, \dots$) due to a differential AC Stark-shifted energy spectrum of the ground and excited state, respectively [114]. Assuming the occupation of vibrational states to be Boltzmann distributed with *Boltzmann factor* (see Eq. 4.36)

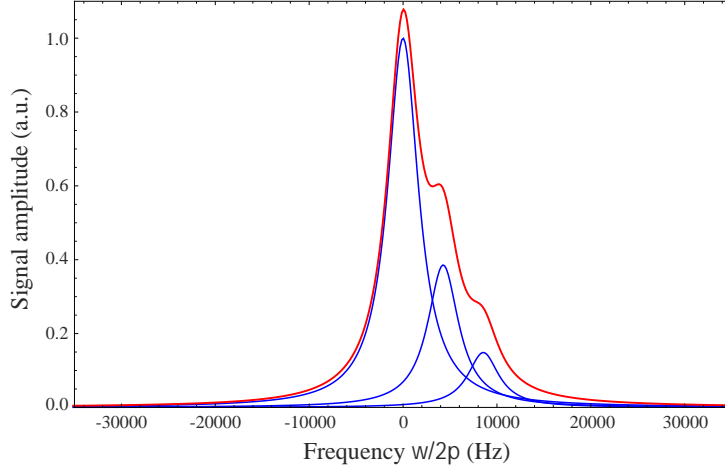


Figure 4.6: Inhomogeneous broadening of the carrier transition due to a lattice AC Stark shift. Carrier transitions $\Omega_{n,n}$ (here $n = 0, 1, 2$, blue curves) sum up to an envelope featuring an asymmetry (red curve).

$$f_B = (\langle n \rangle + 1) / \langle n \rangle = e^{-\hbar\omega_z / (k_B T)}, \quad (4.46)$$

the - under "magic" conditions degenerate - carrier spectrum will show an inhomogeneously broadened line shape

$$\mathcal{L}(\delta, d\omega) \propto \sum_{n=0}^{N_z} \left(\frac{(f_B)^n}{(\delta - \omega_0 + nd\omega)^2 + \Delta\omega^2} \right), \quad (4.47)$$

consisting of several Lorentzian profiles belonging to $\Omega_{n,m}$ ($n = m = 0, 1, 2, \dots$) carrier transitions, weighted by the Boltzmann factor. Here, N_z is the maximum number of occupied axial vibrational states², δ is the frequency detuning, ω_0 is the center frequency, $d\omega$ is the differential AC Stark shift and $\Delta\omega$ is the Lorentz linewidth [108]. Figure 4.6 shows the expected carrier spectrum for the magnesium clock transition featuring an AC Stark shift of ~ 4 kHz at a trap depth of $U_0 = 27.5 E_R$ for $20 \mu\text{K}$ cold atoms. The linewidth of each carrier transition $\Omega_{n,n}$ (here $n = 0, 1, 2$) has been fixed at 2 kHz. However, tuning the lattice wavelength allows for the determination of the magic wavelength depending on the asymmetry of the carrier envelope [108, 114, 115]. A method of preventing multiple vibrational carrier transitions would be the purification of higher vibrational states via state-selective optical pumping (see Chapter 6).

4.2.3 Excitation inhomogeneities II - Atomic motion

Another type of inhomogeneity arises due to the non-zero atomic temperature and hence the atom's motion in the trap. Having a look at Figure 4.4 (*left*), radially

²Note that $N_z \simeq \frac{U_0}{\hbar\omega_z} = \sqrt{\frac{U_0}{4\hbar\omega_R}}$ and $N_r \simeq N_z \frac{\omega_z}{\omega_r}$ [109].

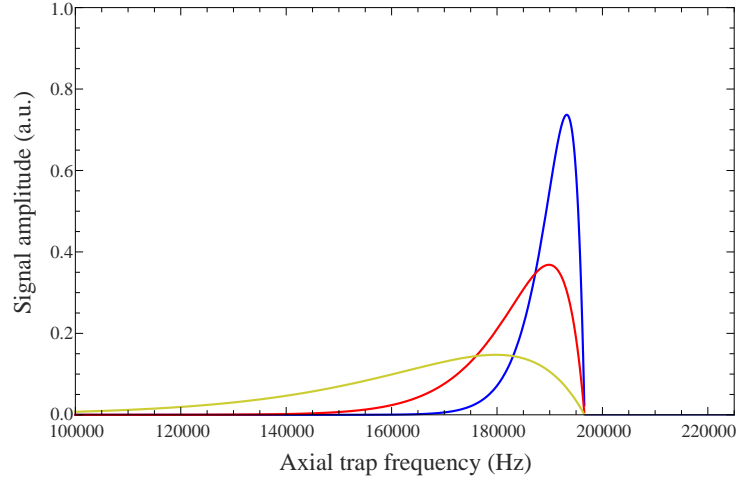


Figure 4.7: Effect of radial motion on the blue sideband. Assuming a trap depth of $9.5 E_R$, the expected trap frequency (including quartic distortion of the lattice potential) is 196 kHz. Sideband spectra are plotted for radial temperatures of $T_r = 1 \mu\text{K}$ (blue), $T_r = 2 \mu\text{K}$ (red) and $T_r = 5 \mu\text{K}$ (green).

oscillating atoms experience shallower well depths, the more they move away from the radial center (the lattice axis). As a consequence, they exhibit different lattice intensities and therefore different axial trap frequencies. The variety of resulting Rabi frequencies (Eq. 4.24) leads to inhomogeneities on the vibrational sidebands as well as on the carrier transition.

Focussing first on the blue sideband, the clock transition includes a motional transition given by $|n\rangle = |n_x, n_y, n_z\rangle \rightarrow |m\rangle = |n_x, n_y, n_z + 1\rangle$ with a corresponding frequency difference given by Eq. 4.43. The radial motional distribution now defines the shape of the blue sideband in terms of amplitude for a certain clock laser detuning: any motional state (n_x, n_y) will shift the axial sideband frequency due to the $r^2 z^2$ coupling term in Eq. 4.39. Blatt *et al.* give an approximate line shape as a function of detuning δ from the carrier frequency and radial temperature T_r [109]:

$$\sigma_{\text{blue}}^{n_z}(\delta) = \frac{\alpha^2}{\tilde{\gamma}(n_z)} \left[1 - \frac{\delta}{\tilde{\gamma}(n_z)} \right] e^{-\alpha[1-\delta/\tilde{\gamma}(n_z)]} \Theta[\tilde{\gamma}(n_z) - \delta], \quad (4.48)$$

where $\alpha = [\tilde{\gamma}(n_z)/\omega_R] \hbar \omega_z / (k_B T_r)$ and $\tilde{\gamma}(n_z) = \omega_z - \omega_R(n_z + 1)$ is the uncoupled axial frequency separation and Θ is the Heaviside function. Main feature of this line shape is the exponential slope falling towards the carrier, taking care of the coupling between radial and axial degrees of freedom. Summing over all possible, axial states, the thermally averaged blue sideband absorption cross section is given by

$$\sigma_{\text{blue}}(\delta) \propto \sum_{n_z=0}^{N_z} e^{-E_{n_z}/(k_B T_z)} \sigma_{\text{blue}}^{n_z}(\delta), \quad (4.49)$$

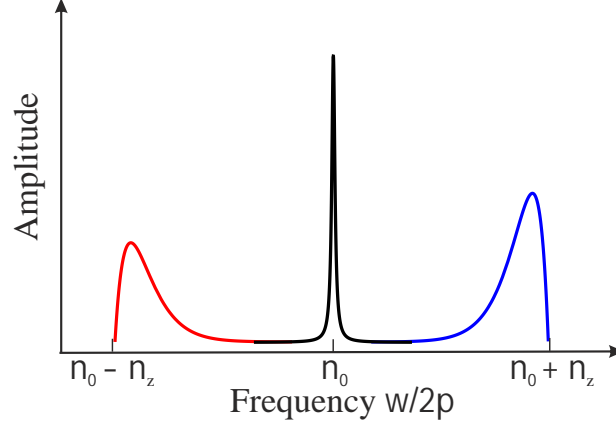


Figure 4.8: Effective frequency spectrum in lattice Lamb-Dicke spectroscopy. The first axial sidebands wash out towards the carrier, as they are inhomogeneously broadened due to radial motion of the atoms.

with the axial temperature T_z . Assuming a $9.5 E_R$ deep trap for magnesium atoms, Figure 4.7 shows expected blue sideband spectra plotted for different radial temperatures T_r using Eq. 4.49. One clearly sees the inhomogeneous broadening being present even for low radial temperatures ($1 \mu\text{K}$, blue curve) and increasing dramatically for higher temperatures ($5 \mu\text{K}$, green curve) coming together with a loss in signal amplitude.

Derivation of the red sideband's line shape is done analogously. Taking the influence of radial motion on the sideband spectra, the expected frequency spectrum (Fig. 4.3, *left*) for a harmonic oscillator has to be revised for lattice spectroscopy. Figure 4.8 shows the expected frequency spectrum for lattice-based Lamb-Dicke spectroscopy. Furthermore, being not indicated in the revised frequency spectrum, radial sidebands exist with a frequency separation of ω_r from the carrier. Typically, their amplitudes are suppressed if the clock laser is perfectly co-aligned with the lattice axis. If the radial trap frequency is known, a measurement of the axial sideband spectrum gives a full characterization of trap parameters including well depth U_0 and waist w_0 in Eq. 4.41 [109].

Blatt *et al.* further investigated the effect of radial motion on the carrier transition. Therefore, they assumed harmonic oscillator states and energies and approximated the clock probe beam to be a plane wave over the extent of a lattice site, with a transverse shape function describing its intensity profile. Choosing a small tilt $\Delta\theta$ of the probe axis relative to the lattice axis such that $\mathbf{k}_{\text{clock}} \simeq k_{\text{clock}}(\mathbf{e}_z + \Delta\theta\mathbf{e}_x)$, they obtain a Rabi frequency (according to Eq. 4.34) of

$$\Omega_{n_x, n_z} \simeq \Omega e^{-\eta_x^2/2} e^{-\eta_z^2/2} L_{n_x}(\eta_x^2) L_{n_z}(\eta_z^2), \quad (4.50)$$

with

$$\eta_z = \frac{1}{\lambda_{\text{clock}}} \sqrt{\frac{\hbar}{2m_a \omega_z}} \quad (4.51)$$

and

$$\eta_x = \frac{\Delta\theta}{\lambda_{\text{clock}}} \sqrt{\frac{\hbar}{2m_a \omega_r}}. \quad (4.52)$$

For a trap depth of $10 E_R$, we expect Lamb-Dicke parameters in ^{24}Mg of $\eta_z \simeq 0.4$ and $\eta_x \simeq \Delta\theta \times 11.8$. Compared to strontium [109], the carrier transition in magnesium is hence expected to be almost a factor of four times more sensitive to misalignments in the transverse direction.

Evaluating how the carrier Rabi frequency is affected by radial motion, Blatt *et al.* give the excited state probability for a motional state $|n\rangle$, detuning δ and pulse time t (neglecting any decoherences, such as trap lifetime) as

$$p_e(n, \delta, t) = \frac{\Omega_{n_x, n_z}^2}{\Omega_{n_x, n_z}^2 + \delta^2} \sin^2[\pi t \sqrt{\Omega_{n_x, n_z}^2 + \delta^2}]. \quad (4.53)$$

Summing over each vibrational state, the total excited state population results to

$$P_e(\delta, t) = \sum_{n_x, n_z} q_{n_x}(T_r) q_{n_z}(T_z) p_e(n, \delta, t), \quad (4.54)$$

with normalized Boltzmann weights q_{n_x} (q_{n_z}) corresponding to radial (axial) temperature T_r (T_z):

$$\begin{aligned} q_{n_x} &= (1 - z_x) z_x^{n_x}, & z_x &\equiv e^{-\hbar\omega_r/(k_B T_r)}, \\ q_{n_z} &= (1 - z_z) z_z^{n_z}, & z_z &\equiv e^{-\hbar\omega_z/(k_B T_z)}. \end{aligned} \quad (4.55)$$

Eq. 4.54 can be further simplified, if it is assumed that the atoms are at low (axial) temperatures, such that only the axial ground state $n_z = 0$ will be occupied. The excited state population can then be approximated as

$$P_e(t) \simeq \frac{1}{2} + \frac{1 - z_x z_x \cos[\phi(1 - \eta_x^2)] - \cos\phi}{2(1 + z_x^2 - 2z_x \cos(\phi\eta_x^2))}, \quad (4.56)$$

where $\phi = 2\pi t \Omega e^{-\eta_x^2/2} e^{-\eta_z^2/2}$ [109]. Assuming a trap depth of $10 E_R$ and above given Lamb-Dicke parameters, Figure 4.9 shows the calculated excited state fraction of 3P_0 atoms in ^{24}Mg using Eq. 4.56 and expected Rabi frequency $\Omega/2\pi = 145$ Hz from Eq. 3.6. In the first case (*left*), the tilt between the probe beam and the lattice axis is assumed to be $\theta = 10$ mrad. For relatively cold motion of $1 \mu\text{K}$ in radial direction (blue curve), the excited state population damps out towards steady-state population quite fastly, but still showing multiple Rabi flops. At a radial temperature of $7 \mu\text{K}$, which is the more realistic case in our experiment, one barely expects a few Rabi flops for small pulse times. In Figure 4.9 (*right*) the

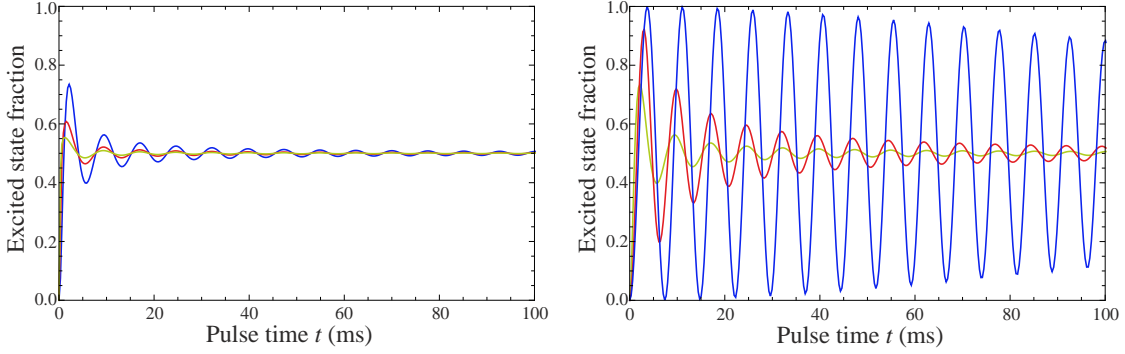


Figure 4.9: (*Left*) Excited state population for radial temperatures of $1 \mu\text{K}$ (blue curve), $3 \mu\text{K}$ (red curve) and $7 \mu\text{K}$ (green curve). The estimated trap depth is $10 E_R$ and a tilting angle of $\theta = 10 \text{ mrad}$ of the probe beam relative to the lattice axis is assumed. (*Right*) Excited state population for a fixed radial temperature of $1 \mu\text{K}$ and tilting angles of $\theta = 1 \text{ mrad}$ (blue curve), $\theta = 5 \text{ mrad}$ (red curve) and $\theta = 10 \text{ mrad}$ (green curve). The estimated trap depth is $10 E_R$.

radial temperature is assumed to be $1 \mu\text{K}$ while the tilting angle has been varied. For almost no tilt ($\theta = 1 \text{ mrad}$, blue curve) the influence of radial motion on the carrier transition decreases.

4.3 Carrier spectroscopy and Bloch bands

As it has already been mentioned in the previous section, the picture of harmonic oscillator states does not hold anymore for the potential of an optical lattice. In fact, taking into account the energy dispersion for lattice-trapped atoms, which is in close analogy to electrons in a solid-state crystal, this system features a band structure of eigenstates: the formation of energy bands gives rise to atomic inner-band tunneling between adjacent lattice sites.

In this section I will show, based on a theoretical prediction by P. Lemonde and P. Wolf [116], that is briefly summarized in Subsection 4.3.1, that tunneling motion is expected to influence the carrier transition such that its signal amplitude will decrease under specific circumstances and will lead to a new line shape related to tunneling motion of the atoms (see Subsection 4.3.2). To the end, Subsection 4.3.3 gives a more generalized treatment for arbitrary lattice wavelengths.

4.3.1 Tunneling between adjacent lattice sites - The band structure

Considering atoms being trapped in an optical lattice and probed on its clock transition, the total Hamiltonian as given in Eq. 4.19 can be used, if Eq. 4.8 is replaced by the Hamiltonian for a standing wave potential

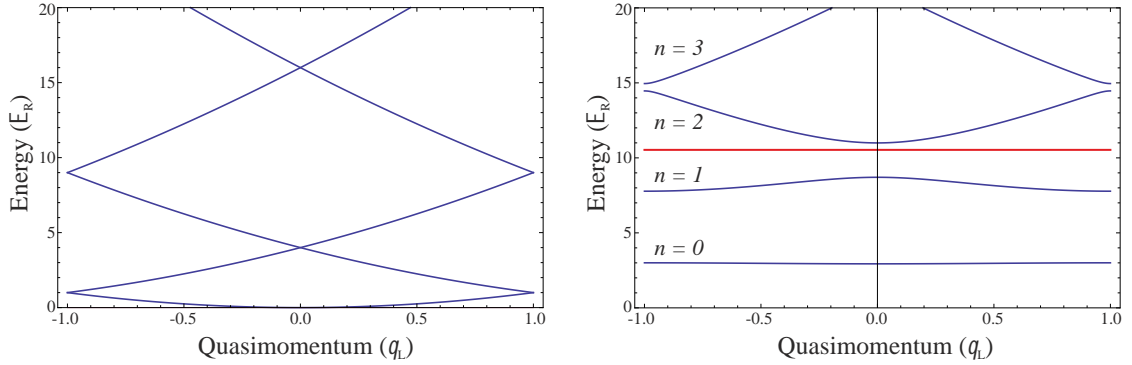


Figure 4.10: Energy dispersion as a function of lattice quasimomentum with restriction to the first Brillouin zone. In the case of a free particle, the well-known energy parabola $E = p^2/2m$ is folded back on itself (*left*). At a trap depth of $10.5 E_R$ (red line), one already sees the formation of energy bands, whereas the lowest two motional states will be trapped in the lattice (*right*).

$$\hat{H}^{(m)} = \frac{\hbar^2 \hat{\kappa}^2}{2m_a} + \frac{U_0}{2} [1 - \cos(2k_L \hat{z})], \quad (4.57)$$

where $\hbar \boldsymbol{\kappa}$ is the atomic momentum. It is further assumed, that the optical lattice is operated at the magic wavelength, so above Hamiltonian acts identical on the ground and excited states of the clock transition.

According to the Bloch theorem [117], the Hamilton operator in Eq. 4.57 has eigenstates $|n, q\rangle$ and corresponding eigenenergies $\hbar\omega_{n,q}$ owing two quantum numbers: the band index n and the quasimomentum q . As an optical lattice, just as its counterpart in solid state physics, is a periodic potential, the eigenstates are also periodic in q with period $2k_L$. Hence, studies on lattice bands are usually restricted to the first Brillouin zone ($q \in [-k_L, k_L]$) [116]. For atomic plane waves with wave vector $\boldsymbol{\kappa}$,

$$\hat{H}^{(m)} |\boldsymbol{\kappa}\rangle = \left(\frac{\hbar^2 \boldsymbol{\kappa}^2}{2m_a} + \frac{U_0}{2} \right) |\boldsymbol{\kappa}\rangle - \frac{U_0}{4} (|\boldsymbol{\kappa} + 2k_L\rangle + |\boldsymbol{\kappa} - 2k_L\rangle), \quad (4.58)$$

having the shape of a tridiagonal Toeplitz matrix [118]. Diagonalization of this gives the eigenenergies and eigenvectors as a linear combination of plane waves, known as the Bloch vectors:

$$\begin{aligned} \hat{H}^{(m)} |n, q\rangle &= \hbar\omega_{n,q} |n, q\rangle, \\ |n, q\rangle &= \sum_{i=-\infty}^{\infty} C_{n,\kappa_i,q} |\kappa_{i,q}\rangle, \end{aligned} \quad (4.59)$$

where $\kappa_{i,q} = q + 2ik_L$. Each quasimomentum q thus features a discrete set of energies $\hbar\omega_{n,q}$ and coefficients $C_{n,\kappa_i,q} \in \mathbb{R}$ with $\sum_i C_{n,\kappa_i,q}^2 = 1$.

Figure 4.10 visualizes the atom's energy as a function of lattice quasimomentum. Free particles with energy $E = p^2/2m_a$ experience a continuous energy

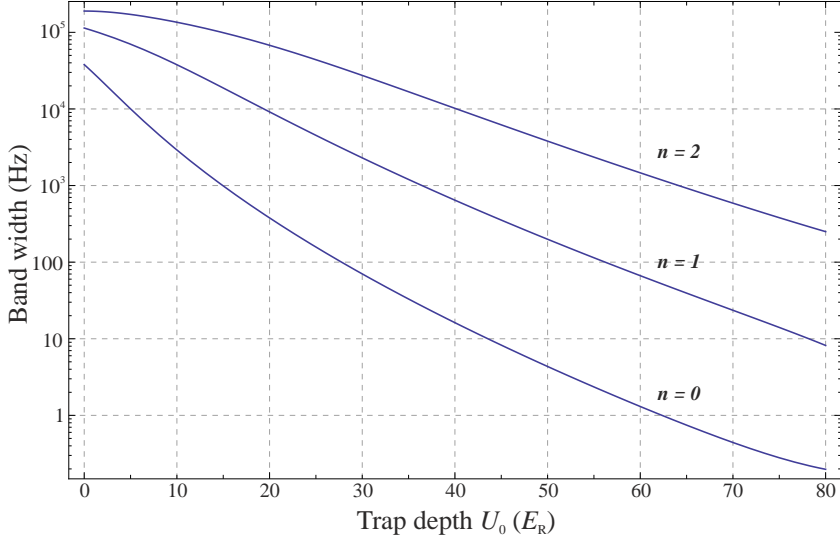


Figure 4.11: Band widths for the lowest three motional bands as a function of trap depth.

dispersion (*left*). For increasing trap depths, the energy parabola splits up to the forming of energy bands (*right*) (see also Fig. 4.4, *right*). Calculated for a well depth of $10.5 E_R$, the two lowest motional bands will be trapped in the lattice. Due to the finite depth of the lattice, the energy bands show a deformation throughout the first Brillouin zone. Hence, one can define the band widths by

$$\Delta E = |\hbar(\omega_{n,k_L} - \omega_{n,0})|. \quad (4.60)$$

Each motional band width decreases for increasing trap depth, as depicted in Fig. 4.11. In magnesium, high laser powers are required to generate sufficient deep traps: Featuring a lattice waist of $79 \mu\text{m}$, a circulating power of 11 W would be necessary to reduce the lowest band width below 1 Hz at a trap depth of $63.5 E_R$.

4.3.2 The effect of tunneling motion - Simulation of the carrier signal

If atoms undergo a transition $\Omega_{n,m}$ (see Eq. 4.34), the time behavior of this two-level system is described via the *Bloch equations* [119]:

$$\begin{aligned} i\dot{a}_{n,q}^g &= \sum_m \frac{(\Omega_q^{m,n})^*}{2} e^{i\Delta_q^{m,n}t} a_{m,q+k_{\text{clock}}}^e, \\ i\dot{a}_{n,q+k_{\text{clock}}}^e &= \sum_m \frac{\Omega_q^{n,m}}{2} e^{-i\Delta_q^{n,m}t} a_{m,q}^g, \end{aligned} \quad (4.61)$$

where $\Omega_q^{n,m} = \Omega \sum_i C_{m,\kappa_{i,q}} C_{n,\kappa_{i,q+k_{\text{clock}}}}$ and $\Delta_q^{n,m} = \omega - \omega_0 + \omega_{m,q} - \omega_{n,q+k_{\text{clock}}}$ [116]. In essence, the action of the probe laser in momentum space $e^{ik_{\text{clock}}\hat{z}}$ couples a state

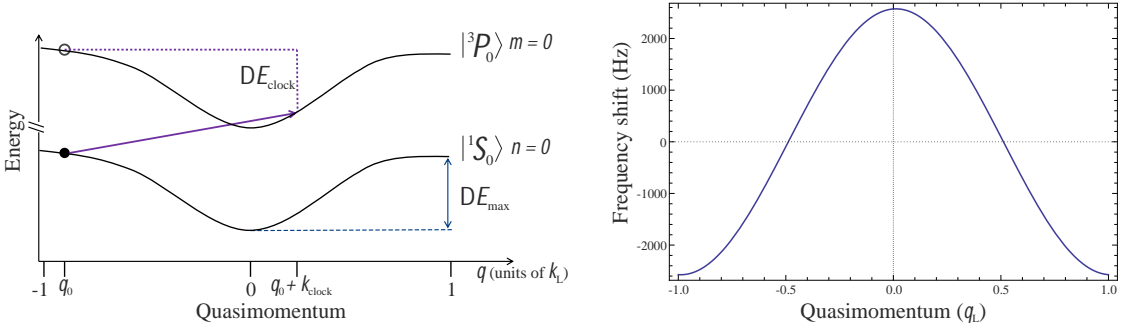


Figure 4.12: (Left) Scheme of optical spectroscopy of Bloch bands. Atoms are excited on the $^1S_0 \rightarrow ^3P_0$ clock transition at 458 nm starting from the lowest motional band without changing the vibrational quantum number. As the clock pulse is applied, the photon momentum adds to the initial atomic momentum causing a net energy difference. (Right) Calculated frequency shift as a function of initial lattice quasimomentum at a trap depth of $10.5 E_{\text{clock}}$. Depending on the initial quasimomentum, the tunneling frequency shift can be negative, positive or equal to zero.

$|n, q\rangle$ to $|m, q + k_{\text{clock}}\rangle$ thereby causing a frequency shift of $\Delta E_{\text{clock}}/\hbar = \omega_{m, q+k_{\text{clock}}} - \omega_{n, q}$ with respect to the atomic resonance, as illustrated in Fig. 4.12: as the lattice is assumed to be at the magic wavelength, the motional bands of the ground and excited states are identical (left). Hence, for clock excitation without momentum transfer, the band energy at initial quasimomentum q_0 is equal for both ground and excited state. Consequently, the visualization of the energy mismatch ΔE_{clock} reduces to the comparison of band energies at momentum positions q_0 and $q_0 + k_{\text{clock}}$ in the excited state band. Depending on the initial quasimomentum q_0 of the atom, this frequency shift may be either negative, zero or positive. Fig. 4.12 (right) shows the expected frequency shift as a function of initial quasimomentum, calculated for a trap depth of $10.5 E_R$. The expected width of the lowest vibrational band at this well depth is $\simeq 2.5$ kHz and, as can be seen, the frequency shift due to the band structure is of the order of the ground state band width. Furthermore, it is periodic in q with two possible initial momenta $q_0 \simeq \pm 0.5 q_L$ resulting in a zero frequency shift. Nevertheless, in the case of magnesium, $\lambda_L = 469 \text{ nm} > \lambda_{\text{clock}} = 458 \text{ nm}$ and consequently $k_L < k_{\text{clock}}$, thus the maximum possible frequency shift (the maximum band width) should never be observed.

However, a frequency shift directly affects the clock transition. Solving the Bloch equations 4.61 gives the excitation probability on the clock transition. Assuming the ground state band to be uniformly populated, all initial quasimomenta q_0 should participate to the spectroscopy signal, if the laser is swept over the carrier resonance frequency [120]. The expected frequency spectrum is plotted in Fig. 4.13 for different lattice trap depths. The Rabi frequency has been chosen to be $\Omega/2\pi = 145 \text{ Hz}$ according to Eq. 3.6 and the pulse time hence equals a $\pi/2$ -pulse. For shallow lattices, the signal amplitude of the carrier transition drops, giving rise to a resonance structure featuring two shifted maxima. Lemonde and Wolf designate this shift away from the unperturbed resonance frequency to a "Doppler effect

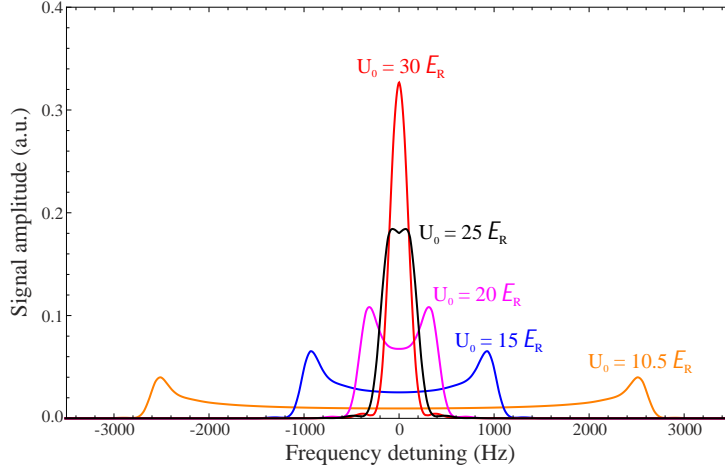


Figure 4.13: Simulation of the carrier spectrum being modified by the lattice band structure. The Rabi frequency has been chosen according to Eq. 3.6 and the pulse time corresponds to a $\pi/2$ -pulse. For decreasing trap depths, the signal amplitude decreases as well and the spectral feature broadens into a resonance structure featuring two maxima as the result of tunneling motion induced Doppler effects.

associated with tunneling motion" [116]. For increasing trap depths, the line shape broadening decreases (blue and magenta curves), starts to overlap (black curve) and transforms into the expected *sinc*-line shape for a sufficiently deep lattice (red curve). But what exactly is "sufficiently deep"? The carrier resonance obviously breaks together and broadens, if the *shallow lattice regime* dominates, here I define with the condition $\Delta E \gg \Omega$. Table 4.1 summarizes the different trap depths used for the simulations in Fig. 4.13 together with the corresponding ground state band widths.

4.3.3 Spectroscopy of Bloch bands close to the magic wavelength

In the previous subsection it was assumed that clock spectroscopy is performed at the magic wavelength. Hence, a symmetrically broadened line shape should be observed in the experiment. Extending this model to arbitrary lattice wavelengths should differently affect the band structure of the ground and excited states as it is directly related to the AC polarizability. Furthermore, the calculations in the last subsection assumed that the lattice potential is of uniform well depth for

Trap depth in E_R	10.5	15	20	25	30
Band width in Hz	2590	893	377	144	71

Table 4.1: Trap depths used for the simulation of the frequency spectrum in Fig. 4.13 and the corresponding ground state band widths.

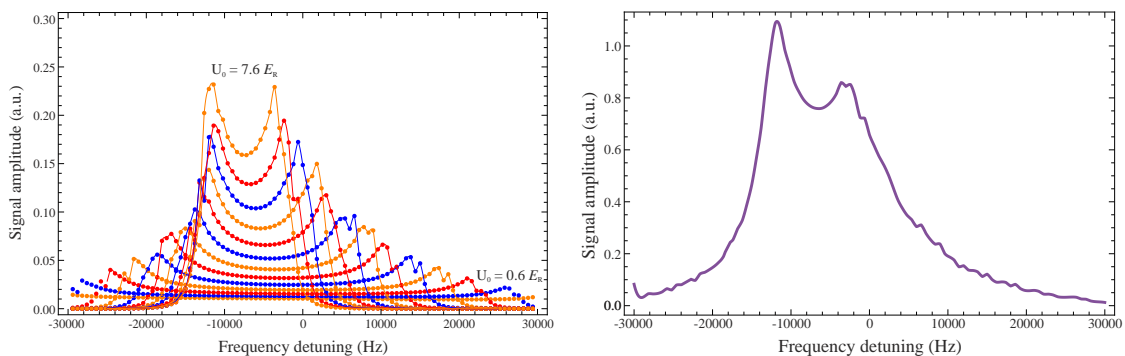


Figure 4.14: (*Left*) Simulation of the carrier spectrum featuring an AC Stark shift. Calculations have been carried out using the Bloch equations in Eq. 4.61 with introduced atomic polarizabilities for the clock states as calculated by [110]. Here, in particular, the contribution from different trap depth's spectra has been plotted, serving as a kind of "base functions" for the calculation of the total spectral feature. (*Right*) Sum of the base functions for different trap depths. The expected signal of the carrier scan features an asymmetric line shape due to inhomogeneous broadening.

each lattice site. However, in reality, the lattice is formed by a Gaussian laser beam. This means, the atoms will explore different well depths in radial and axial direction ruled by the beam parameters. In particular, for random lattice wavelengths, atoms now additionally experience a decreasing AC Stark shift for shallower explored trapping regions. As in our case, the optical lattice is loaded from an elongated dipole trap, approximately 1,000 atoms are distributed over 130,000 lattice sites along the lattice axis. Hence, it is very likely that all these atoms contribute to an inhomogeneous spectral feature during clock spectroscopy.

Fig. 4.14 (*left*) shows the expected frequency spectrum for different trap depths at a lattice wavelength of 467.5 nm, which is below the estimated magic wavelength. Values of corresponding ground and excited state polarizabilities have been chosen according to Fig. 4.5 [110]. For visualization purposes, the spectra have been plotted for a maximum trap depth of $7.6 E_R$ and a minimum trap depth of $0.6 E_R$, as well as sufficient steps in between. Furthermore, $\Omega/2\pi = 400 \text{ Hz}^3$ and $\tau_p = 100 \text{ ms}$ have been chosen, being closer to the experimental parameters. Each plotted curve represents the calculated interpolation function of the simulated data points. In a very simple approach, the idea was that each of the calculated spectra in Fig. 4.14 (*left*) can be treated as a sort of "base function" ϕ_i belonging to a certain potential well with trap depth U_i . A linear combination $\sum_i c_i \phi_i$ with $c_i \in \mathbb{R}_+$ of all these base functions should then result in a fitting function which can be applied to the experimental data. Fig. 4.14 (*right*) exemplarily shows the sum with $c_i = 1 (\forall i)$ of the base functions, assuming a uniform distribution of the atoms along the lattice sites, to give a first idea on the overall expected frequency spectrum.

In the experiment, the atoms are distributed over several lattice sites (each having a different trap depth due to the Gaussian lattice beam) and will all contribute

³Note that $\Omega_{\text{eff}} = \sqrt{\Omega^2 + (\Delta E_{\text{clock}}/\hbar)^2}$.

to the resonance signal. The latter is thus expected to feature an inhomogeneous broadening. In particular, the line shape now shows a certain asymmetry whereas two features are of interest: The resonance peak's amplitude and their slopes. For a lattice wavelength smaller than the magic wavelength, the left peak appears with a larger amplitude and a steeper slope, the right peak is of smaller amplitude and facing a flatter slope. The same holds inversely for a lattice wavelength being larger than the magic wavelength. Hence, it seems likely to investigate the local minimum between the resonance's maxima and the FWHM frequency values of the slopes to make a qualitative statement on experimental data. If done so, a new method of measuring the magic wavelength has been found, requiring just a single recorded frequency spectrum per lattice wavelength.

4.4 Conclusion

In summary, this chapter treats the introduction to Lamb-Dicke spectroscopy, starting out from the ideal harmonic potential and the preparation of tools for understanding the basic features of the Lamb-Dicke regime. Turning to spectroscopy in "real" potentials, e.g. provided by optical lattices, several aspects have been discussed that affect the spectroscopy signal and shall be briefly recalled.

Optical lattices usually operate at the magic wavelength, where the differential AC Stark shift of the clock states vanishes in first order. If multiple motional states in the lattice are occupied due to a Boltzmann distributed ensemble of atoms, carrier transitions $\Omega_{n,m}$ are no longer degenerate if the lattice wavelength deviates from the magic wavelength. Each carrier transition contributes with its Lorentzian line shape to an inhomogeneously broadened total carrier line shape.

As the trapping potential of an optical lattice shows tight confinement along the lattice axis and weak confinement in radial direction due the Gaussian beam shape, atoms have axial and radial degrees of freedom. Related to temperature, radially oscillating atoms explore decreasing trap depths in radial direction and hence decreasing axial confinement, thereby modifying the axial frequency spectrum via inhomogeneous broadening of the sidebands. Performing clock spectroscopy of lattice-trapped magnesium, the carrier transition in the lattice is expected to be sensitive to misalignment of the probe laser relative to the lattice axis. Referring to expected experimental parameters of the magnetically enabled clock transition, Rabi oscillations will almost be suppressed for beam tilts of $\theta \geq 10$ mrad and atoms with a radial temperature of $7 \mu\text{K}$. As a consequence, the clock laser has to be very carefully aligned or the atoms have to be further cooled down.

Finally, the aspect of tunneling motion acting on the carrier frequency spectrum is discussed. Due to the finite well depth, the lattice potential forms vibrational bands rather than explicit states. This band structure enables tunneling between adjacent lattice sites, which can be thought of as residual Doppler motion. If the lattice is operated in the shallow lattice regime, meaning the ground state band

width is larger than the system's Rabi frequency, the signal amplitude of the carrier transition will drop, giving rise to a broadening. This spectroscopic feature is supposed to be of symmetric line shape if the lattice is tuned to the magic wavelength. For different wavelengths, the carrier resonance obeys an asymmetry depending on the lattice wavelength's detuning relative to the magic wavelength. This asymmetry is related to inhomogeneous broadening as the atoms are spread along the longitudinal lattice sites with shallower trap depths, all contributing to the total spectroscopy signal. Nevertheless, it features a new method of determining the magic wavelength.

Lamb-Dicke spectroscopy of the $^1S_0 \rightarrow ^3P_0$ clock transition

As I have discussed the theoretical background of Lamb-Dicke spectroscopy in the previous chapter, thereby introducing the most relevant characteristics, this chapter describes the measurements on Lamb-Dicke localized magnesium atoms, as they have been carried out in the frame of this thesis. In Section 5.1, I will characterize our optical lattice to set up a prerequisite for the following measurements. Section 5.2 treats the light shift measurements on the carrier transition for the determination of the magic wavelength. The measurement of the magnetic polarizability β is described in Section 5.3. Its knowledge further allows the preliminary deduction of the clock transition frequency. Section 5.4 discusses a new method of lattice-based spectroscopy of Bloch bands carried out via an optical transition. This effect becomes pronounced for shallow trap lattices giving rise to a frequency shift of the clock transition together with a change in the spectroscopic line shape. The latter turns out to be lattice wavelength-dependent, alternatively allowing the determination of the magic wavelength.

5.1 Characterization of the optical lattice

Performing clock spectroscopy in ^{24}Mg requires the presence of an external magnetic field for enabling optical dipole excitation of the strongly forbidden $^1S_0 \rightarrow ^3P_0$ transition. As a starting point, a magnetic field of 249 G has been chosen to have a sufficiently large signal-to-noise ratio. Accordingly, the resonance frequency of the clock transition will be shifted due to the second-order Zeeman effect, which is expected to be $-135\,625$ Hz with the above mentioned magnetic field amplitude [67].

Without performing an absolute frequency measurement on the 458 nm clock transition, its frequency is already known with an accuracy of 48 Hz due to previous

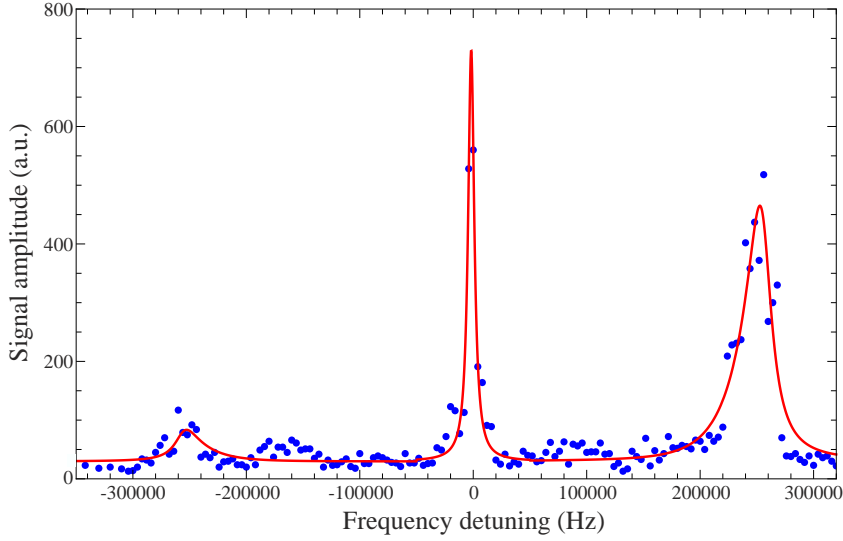


Figure 5.1: Frequency scan of the $^1S_0 \rightarrow ^3P_0$ clock transition at 458 nm. The red curve is a fit corresponding to the line shape derivation in Subsection 4.2.3. The axial sideband frequency separation is 256 kHz, whereas the radial sidebands cannot be resolved here. Including the quartic distortion of the lattice potential, the axial trap frequency of the lattice is 294 kHz.

frequency measurements of the $^1S_0 \rightarrow ^3P_1$ and $^3P_0 \rightarrow ^3P_1$ transitions [57, 121]. Subtracting both frequencies, the clock transition frequency is 655 058 646 681 860(48) Hz, where the above calculated Zeeman shift still has to be added.

As it has been mentioned in the previous chapter, a frequency scan ranging from the first red to the first blue sideband contains information about the temperature of the atoms and the properties of the trapping potential. Figure 5.1 shows such a frequency spectrum recorded at a lattice wavelength of 468.95 nm with a circulating power of 2.4 W. The carrier frequency has been retrospectively set to 0 Hz, displaying just a relative frequency measurement. Having a look at the frequency spectrum, the axial sidebands can be clearly identified by applying the derived sideband line shape from Subsection 4.2.3 as fit to the experimental data (red curve). Observation of motional sidebands verifies that spectroscopy is performed in the resolved sideband regime. As expected, the sideband shape appears to be inhomogeneously broadened, indicating the coupling to radial motion of the atoms. The frequency separation of the axial sidebands from the carrier transition is $\gamma(0)/2\pi = 256 \text{ kHz}$ ¹(see Subsection 4.2.1 and especially Eq. 4.43). Including the lattice recoil frequency of 38 kHz, the axial trap frequency of our optical lattice is 294 kHz. Calculating the Lamb-Dicke parameter according to Eq. 4.25 together with the clock photon's recoil frequency of 40 kHz, $\eta = \sqrt{\omega_{\text{Rec}}/\omega_z} \approx 0.37$, which means the magnesium atoms are well localized in the Lamb-Dicke regime. Furthermore, the knowledge of the axial trap frequency is a direct measure of the lattice

¹Experimentally measured frequencies are always in the unit of $\omega/2\pi$, hence I will restrict myself in the following to "real" frequencies instead of angular frequencies.

Atomic species	²⁴ Mg	¹⁹⁹ Hg	⁸⁷ Sr	¹⁷¹ Yb
Mass in u	23.985	198.968	86.908	170.936
λ_{magic} in nm	468	363	813	759
$E_{\text{R}}/k_{\text{B}}$ in μK	1.8	0.36	0.17	0.09

Table 5.1: Comparison of the commonly used clock isotopes of Mg, Hg, Sr and Yb. Due to its low mass and short magic wavelength, ²⁴Mg features the largest recoil energy among the compared species.

depth according to Eq. 4.41. Hence, the trap depth for the frequency scan in Fig. 5.1 is $U_0 = 15 E_{\text{R}}$.

As a consequence of the lattice loading scheme (see Subsection 3.3.2), the amplitude of the red sideband is suppressed, indicating that most of the atoms are occupying the vibrational ground state. Analyzing the ratio of the first sideband’s amplitudes according to Eq. 4.36, the axial temperature of the atoms is $T_z = 7 \mu\text{K}$, being in agreement with previous measurements on the Doppler width of the atomic velocity distribution [66]. Fitting a Lorentzian lineshape to the carrier feature, the linewidth is approximately 6.5 kHz, hiding the radial sidebands which are supposed to have a frequency separation of a few hundred Hz. The magnetic field enabled linewidth should be just a few μHz while the most dominant contributions to the spectroscopic linewidth probably arise from the ground state band width (see Fig. 4.11) and an inhomogeneous broadening due to the lattice wavelength being not magic. If the radial trap frequency was known, the optical lattice would be fully characterized, as the lattice waist could be determined via Eq. 4.42. As this was impossible for the measurements presented in this work, the lattice waist has been measured to be $w_0 = 79 \pm 4 \mu\text{m}$ using a CCD camera detecting the light leaking out of the enhancement cavity while locked.

However, there is a small spectroscopic feature arising at a frequency detuning of approximately -170 kHz away from the carrier transition (and eventually also at -80 kHz), which has been reproducibly observed. So far, the origin of these resonances could not yet be determined, but it might be that the optical lattice is modulated in some sense, as it has already been observed in other lattice clock experiments [122].

Drawing a first conclusion, large axial trapping frequencies have been observed at moderate trap depths, being almost a factor of three times larger than in ytterbium [68] and a factor of four times larger than in strontium [109]. As a consequence, confinement in the Lamb-Dicke regime is very likely in magnesium. However, for a direct comparison of the clock species, one has to consider the isotopic mass and magic wavelength, as summarized in Table 5.1. Due to their high mass and magic wavelength being in the low-energy regime of the visible spectrum (excluded Hg with its magic wavelength in the UV [108]), Hg, Sr and Yb feature a lattice recoil energy being nearly an order of magnitude smaller, as compared to

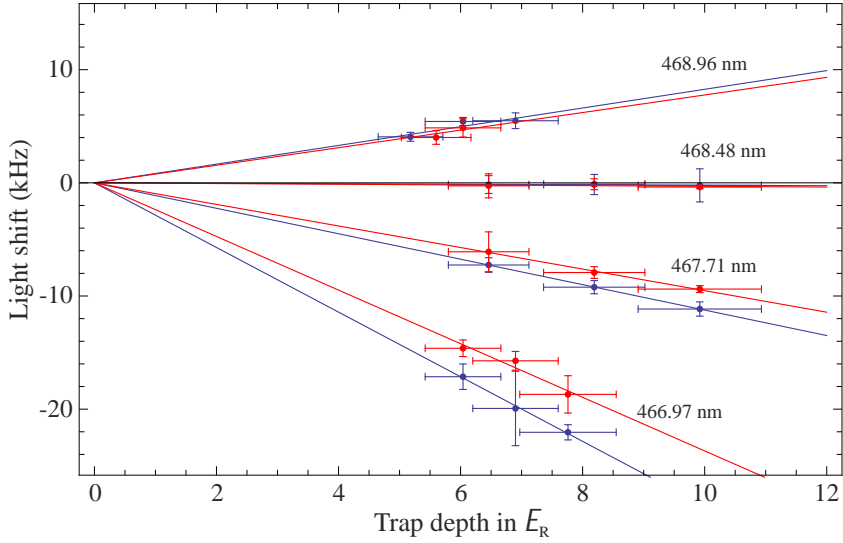


Figure 5.2: AC Stark shift for different lattice wavelengths vs. the lattice trap depth in units of the recoil energy. The red and the blue data correspond to the same experimental parameters but have been recorded independently from each other at different times. The deviation complies with the combination of statistical and systematic uncertainties.

Mg. Additionally possessing larger atomic polarizabilities, ytterbium and strontium lattice clocks usually operate at recoil energy normalized trap depths of up to $300 E_R$ achieving spectroscopic linewidths of a few Hz [38, 123]. Hence, these species are not limited by the ground state band widths.

5.2 Measurement of the magic wavelength for the clock transition

The differential AC Stark shift is directly proportional to the lattice wavelength and trap depth. According to Eq. 4.44, it should add an offset to the unperturbed resonance frequency ν_0 . A measurement campaign comprising frequency scans on the carrier transition for several trap depths, being repeated at different lattice wavelengths, typically gives rise to the zero-shift at the magic wavelength. For the $^1S_0 \rightarrow ^3P_0$ clock transition in magnesium, the most precise calculation of the magic wavelength suggests $\lambda_{\text{magic}} = 468.45(23)$ nm (see Subsection 4.2.2), thus, measurements in a wavelength range from 467 to 469 nm have been performed, as depicted in Fig. 5.2. Each data point of this graph represents the Gaussian fit's center frequency of a data set consisting of three independent carrier scans being merged together. For clarity, Fig. 5.3 (*left*) shows the measurement campaign for a lattice wavelength of 466.97 nm. Each graph shows the number of excited atoms (red and blue dots) as a function of clock laser frequency and the corresponding Gaussian fits (red and blue solid curves). The measurement procedure was as

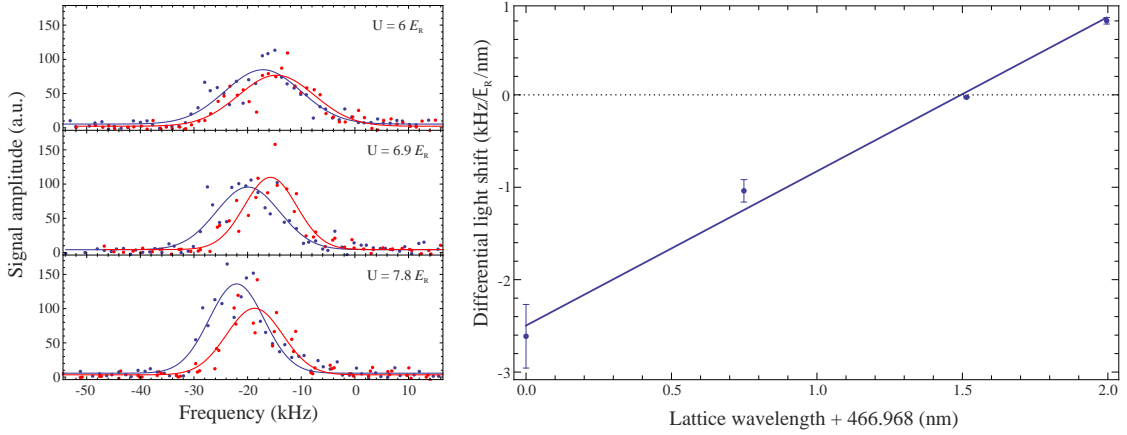


Figure 5.3: (*Left*) Frequency scans of the line profile taken at different lattice depths, exemplarily shown for a lattice wavelength of 466.97 nm. Each data represents the combination of three line scans being corrected for residual clock laser drifts. The solid lines are Gaussian profiles that have been fitted for center frequency determination. (*Right*) Linear regression of the combined measurements in Fig. 5.2 as a function of lattice wavelength. The magic wavelength (crossing point between regression and dotted line) determines to 468.463(207) nm. The linear dependence of the AC Stark shift on lattice depth and wavelength is 1.669(115) kHz/ E_R /nm.

follows:

Initial clock laser drifts have been removed as described in Subsection 3.4.2. However, taking multiple measurements on the carrier transition without changing experimental parameters, we observed residual clock laser drifts due to thermal disequilibrium of the clock laser’s ULE cavity. The line profiles for different trap depths were measured successively, while a single line scan comprises about 30 measurements, each lasting 1.9 s. The linewidth of the carrier transition is on the order of 10 kHz being most probably dominated by the lattice band width (see Fig. 4.11), as it narrows down for increasing trap depth. The measurement sequence has been repeated three times to evaluate and correct for the residual laser drift. The corresponding frequency shift has been measured by fitting Gaussian profiles to the data. Comparing the frequencies for a specific lattice depth, residual clock laser drifts being as large as 2 – 3 kHz were determined in several minutes. Finally, each of the line profiles in Fig. 5.3 is obtained by superimposing the drift-corrected frequency scans to one single data set. Fitting a Gaussian profile to this data set, the resulting center frequency is used for evaluation in Fig. 5.2, where the line center frequencies are plotted together with a linear regression for the corresponding AC Stark shift. Taking each wavelength measurement, an individual offset was subtracted from each data set (as a consequence of the thermal drift of the ULE cavity), such that they cross at zero lattice intensity. The data point’s error bars are composed as follows: The uncertainty of the determination of the lattice depth is about 5% being dominated by the uncertainty of the measurement of the lattice waist, as it showed slight deviations throughout daily operation. The uncertainty of the AC Stark shift results from the combined statistical uncertainty

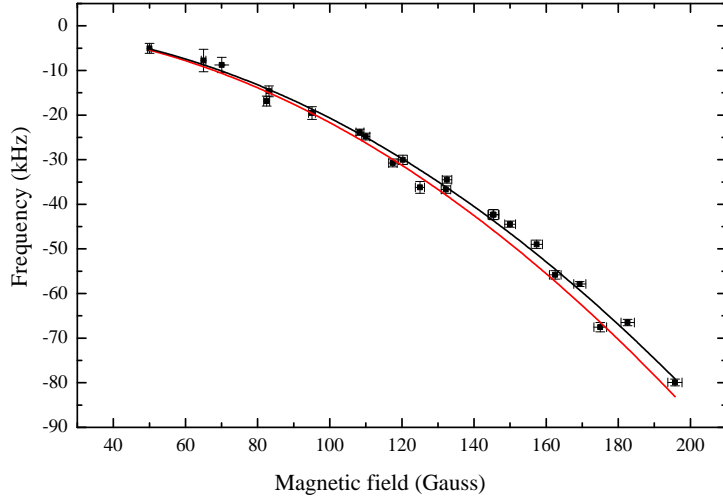


Figure 5.4: Measurement of the quadratic Zeeman shift. The center frequency of the carrier transition (black squares) is plotted as a function of magnetic field amplitude. We derive a Zeeman coefficient of $\beta = -206.6(2.0) \text{ MHz/T}^2$ ($= -2.06(2) \text{ Hz/G}^2$, black solid curve), being consistent with a theoretical prediction of $\beta = -217(11) \text{ MHz/T}^2$ (red solid curve).

of the line center fits and the systematic uncertainty due to residual clock laser drifts leading to frequency offset fluctuations on the order of a few kHz.

The red and the blue data display the same measurement campaigns being performed at different times to check the consistency of the measurements. Their deviation in the AC Stark shift complies with the above described uncertainties. The magic wavelength for the $^1S_0 \rightarrow ^3P_0$ clock transition in ^{24}Mg determines to $\lambda_{\text{magic,exp}} = 468.463(207) \text{ nm}$, with a linear dependence of the AC Stark shift on lattice depth and wavelength of $1.669(115) \text{ kHz/E}_R/\text{nm}$. Treating the two measurement campaigns displayed in Fig. 5.2 independently, $468.472(224) \text{ nm}$ (blue data) and $468.452(192) \text{ nm}$ (red data) were obtained for the value of the magic wavelength, being consistent with the averaged value. The final value is also in excellent agreement with the previously mentioned theoretical calculation of $\lambda_{\text{magic,theo}} = 468.45(23) \text{ nm}$ [110].

5.3 Measurement of the 2nd order Zeeman shift

The presence of an external magnetic field enhances optical dipole coupling of the $^1S_0 \rightarrow ^3P_0$ clock transition in bosonic isotopes, as it has already been demonstrated with ytterbium [68] and strontium [69], but it also implies a large shift on the transition frequency due to the second-order Zeeman effect. Hence, a careful measurement of the magnetic polarizability is necessary to give a first estimate of the unperturbed clock transition frequency.

Atomic species	Mg	Sr	Yb
Theory	-217(11)	-23.3(1.2)	-6.2(3)
Experiment	-206.6(2.0)	-23.5(2)	-6.6(4)

Table 5.2: Comparison of the magnetic polarizability β of Mg, Sr and Yb. Values are given in MHz/T².

5.3.1 Measurement of the magnetic field dependence

Similar to the measurement of the wavelength dependence, the carrier frequency shift has been studied for various magnetic field strengths. The magnetic field amplitude has been determined to 2.49(1) G/A by performing optical spectroscopy of the $^3P_1 m_J$ Zeeman sub-states [66] with a sensitivity of 2.1 MHz/G [72]. Figure 5.4 shows the center frequency (black squares) of the $^1S_0 \rightarrow ^3P_0$ carrier transition, obtained by Gaussian fits, as a function of magnetic field amplitude. To suppress systematic drifts of the experiment, the Zeeman shift was measured in an interleaved sequence². Applying a parabolic fit to the experimental data, the magnetic polarizability is $\beta = -206.6(2.0)$ MHz/T² (equivalent to $-2.06(2)$ Hz/G², black solid curve) which is consistent with the theoretical prediction of $\beta = -217(11)$ MHz/T² (red solid curve) [67, 124].

The experimentally determined magnetic polarizabilities in ytterbium and strontium are $\beta_{\text{Yb}} = -6.6(4)$ MHz/T² and $\beta_{\text{Sr}} = -23.5(2)$ MHz/T² [68, 125], respectively, all being nearly one order of magnitude smaller than in magnesium. Table 5.2 summarizes the measured parameters and their corresponding theoretical prediction [67, 124].

5.3.2 Measurement of the clock transition frequency

To give a first estimate on the clock transition frequency, the spectroscopy laser was beated with an optical frequency comb that was stabilized to a 10 MHz GPS-based reference signal. The parameters for the optical frequency comb were as follows:

$$n = 3275292, \quad \nu_{\text{rep}} \approx 100 \text{ MHz} + 28.1 \text{ Hz}, \quad \nu_{\text{CEO}} = -20 \text{ MHz}, \quad \nu_{\text{beat}} = 31.7 \text{ MHz},$$

where n is the mode number, ν_{rep} is the comb repetition rate, ν_{CEO} is the carrier envelope offset and ν_{beat} is the beat frequency of the laser with the comb at 916 nm. The clock laser frequency in the infra-red is then given by the following equation

$$\nu_{\text{L}} = n \times \nu_{\text{rep}} + \nu_{\text{beat}} + 2\nu_{\text{CEO}}, \quad (5.1)$$

²Such that the magnetic field amplitude has not been varied in a successive way.

where the offset frequency has to be added with a factor of 2, as the beat is recorded with the frequency-doubled comb spectrum [93]. For the measurement of the clock transition frequency, the amplitude of the quenching magnetic field was 184 G, hence the transition is expected to be shifted by $\delta\nu_{\text{Zeeman}} = -108974$ Hz. Furthermore, the switching-AOM frequency of $\nu_{\text{AOM}} = 79.111$ MHz at 458 nm has to be added to the clock laser frequency. Hence, the clock transition frequency results to

$$\nu_0 = 2\nu_L + \nu_{\text{AOM}} - \delta\nu_{\text{Zeeman}} = 655\,058\,646\,691(101) \text{ kHz}, \quad (5.2)$$

where its uncertainty is mainly dominated by the accuracy of the GPS frequency reference. Nevertheless, this value displays a first measurement of the clock transition frequency, being in agreement with the expected value of 655 058 646 681 860(48) Hz. Future, more precise determinations of the transition frequency would require a more accurate frequency reference, e.g. a hydrogen maser or a comparison against several frequency standards at PTB being available via the optical fiber link [92].

5.4 Optical spectroscopy of Bloch bands

The band structure of optical lattices has so far been studied by coupling the ground state band to higher-order bands by means of a phase modulation imprinted on the lattice potential [126] or by mapping the crystal momentum onto free-space momentum by adiabatically lowering the lattice depth [127]. However, in this work, mapping of the shape of the Bloch bands onto a frequency shift of the lattice carrier transition is demonstrated by coupling the lowest band of the 1S_0 ground state to its counterpart in the 3P_0 state via the optical clock transition at 458 nm, as described in Section 4.3. Higher-order bands are not excited in these experiments.

5.4.1 Spectroscopy in the shallow lattice regime

The optical lattice is operated at a wavelength of 468.48 nm, which is the determined magic wavelength for the ^{24}Mg clock transition within the error bars, as described in Section 5.2. After the transfer of the atoms to the lattice, the well depth intensity is lowered to create reproducible temperature conditions for each measurement, before the lattice intensity is set to the final value for clock spectroscopy. Figure 5.5 shows frequency scans of the carrier transition performed for different final lattice depths with a clock laser pulse of 100 ms duration. The red solid curves represent a fit to the experimental data (blue dots) according to a linear combination of base functions for different trap depths (similar to Subsection 4.3.3, but assuming identical polarizabilities for the clock states). However, the

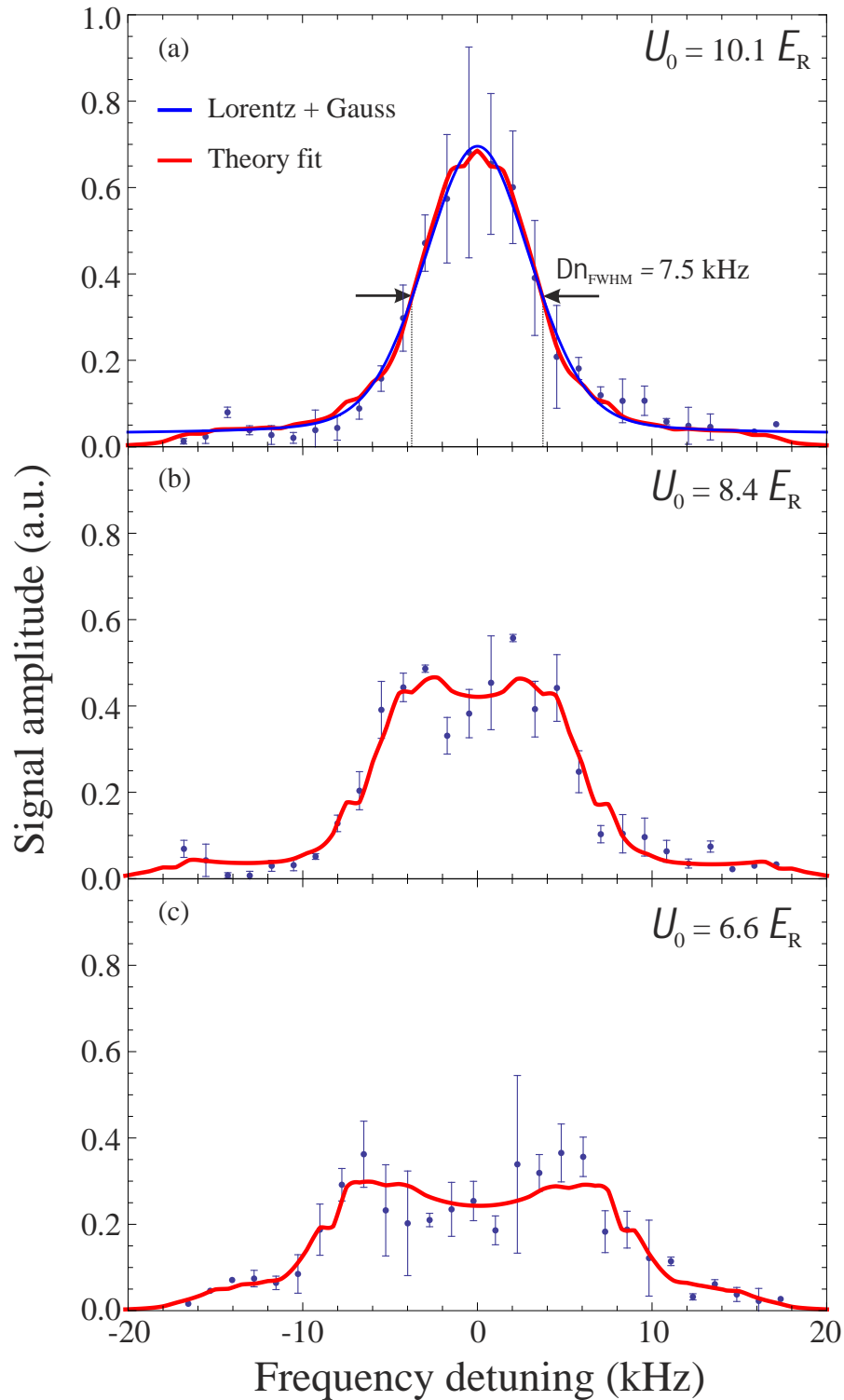


Figure 5.5: Spectroscopy of the carrier signal taken for different trap depths at the magic wavelength. For decreasing trap depths, the signal contrast of the resonance decreases and gives rise to a broadened line shape caused by tunneling motion of the atoms. The red solid curves represent fits according to a linear combination of base functions, as described in Subsection 4.3.3. The blue curve in (a) is a convolution of a Lorentz and a Gauss function.

fitting function is not fully smooth, showing "unphysical" irregularities. The reason for this is the following: As can be seen in Figure 4.14, these irregularities already occur in each interpolated base function as a consequence of a limited number of simulated data points per function, keeping the calculation time in a reasonable frame. An improvement of the theoretical simulation could not be realized in the frame of this thesis.

At a trap depth of $U_0 = 10.1 E_R$ (Figure 5.5, (a)), a distinct spectral resonance is observed. For comparison, a fit based on the convolution of a Lorentzian and a Gaussian profile (blue curve) is plotted versus the fit generated out of the theoretical model. Although both functions agree well for the central data points, they seem to not fully match the high-frequency line shape of the resonance. However, its FWHM linewidth of approximately 7.5 kHz indicates the presence of a broadening mechanism, as the Fourier-limited transition linewidth should be in the order of a few Hz. The expected ground state band width of the optical lattice is 2.8 kHz (see Figure 4.11), giving a first evidence on tunneling induced broadening. The spectral feature becomes more pronounced, while having a look on the frequency scans performed at shallower trap depths (Figure 5.5, (b) and (c)). It is clearly visible that the signal contrast of the carrier amplitude reduces with shallower potentials, giving rise to the simulated line shape of Section 4.3. In this regime, fitting with the above used convolution function is not reasonable anymore.

In essence, this measurement reveals spectral maxima with the expected positive and negative frequency shifts, as has been calculated in Figure 4.12, exemplary for a trap depth of $10.5 E_R$. This in particular means, the shape of the lowest bands of the electronic ground and excited state is probed as a function of frequency detuning. Treating the carrier line shape therefore as a composition of maxima³, it seems not only that they are shifted in the order of the ground state band width, it also appears that the distance of the turning points due to the band structure increases by the same amount, verifying the proposed behavior by P. Lemonde and P. Wolf [116]. Nevertheless, the observed FWHM linewidth (e.g. 7.5 kHz for $U_0 = 10.1 E_R$) cannot fully be explained via tunneling broadening as it is slightly larger than twice the ground state band width. The discussion in Subsection 4.3.3 suggests, that an atomic cloud, which is distributed over several, varyingly deep lattice sites, is expected to cause an inhomogeneous broadening during clock interrogation.

For further investigation of broadening mechanisms, the minimum lattice depth was varied during the phase of the ramp down of intensity, which directly influences the occupancy of the lattice sites. Figure 5.6 shows frequency scans of the carrier transition in the case where no initial intensity variation has been applied to the lattice (a), when the peak intensity has been initially ramped down to $7 E_R$ (b) and to the lowest possible depth⁴ of $5 E_R$ (c). The duration for either ramping down and

³By clearly distinguishing between negatively and positively frequency shifted contributions.

⁴Where atoms still could be trapped by the lattice.

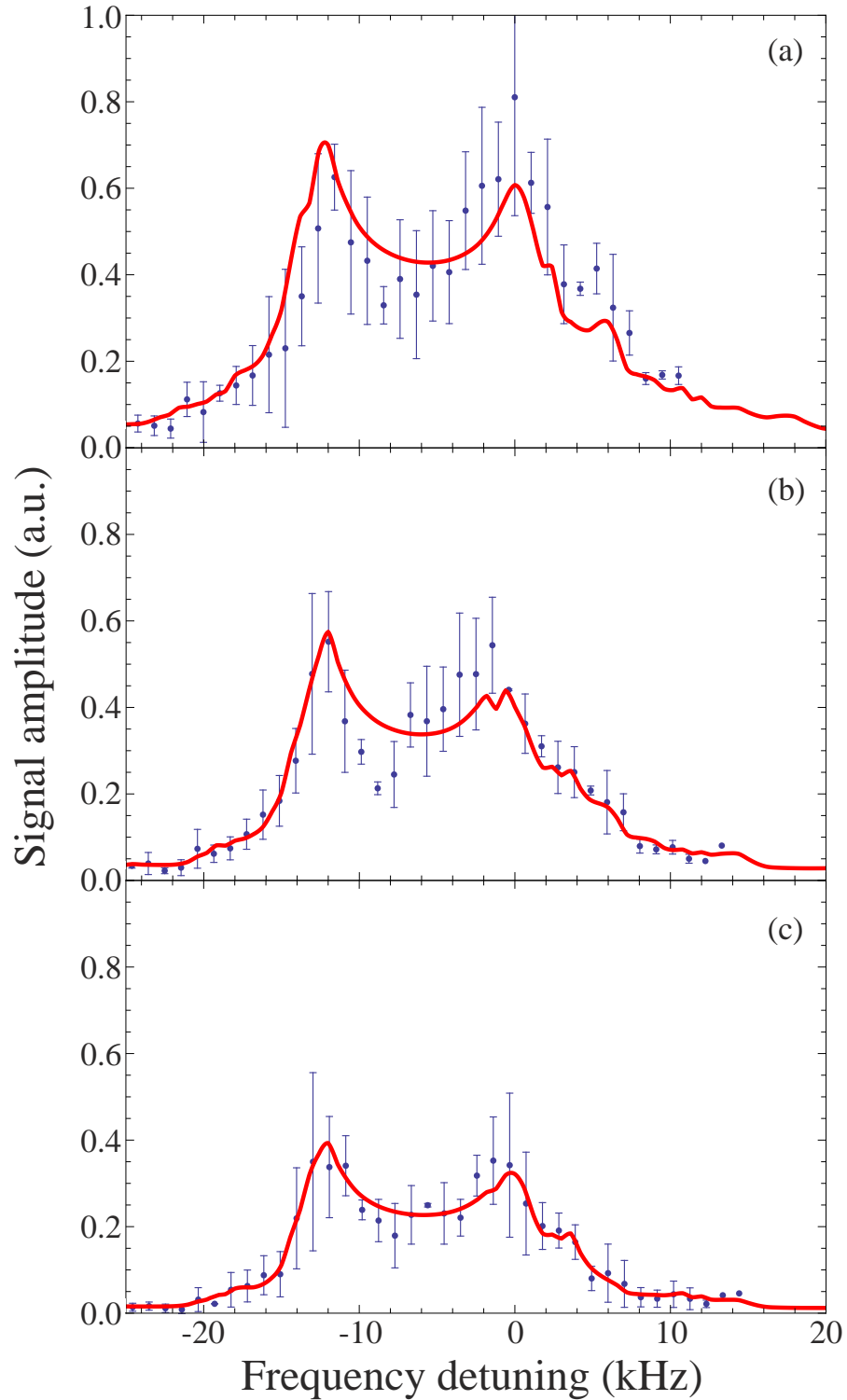


Figure 5.6: Measurement of the carrier signal taken for no initial ramp-down of lattice intensity (a), for a ramp down to $U_0 = 7 E_R$ (b) and a ramp down to the minimum trap depth of $U_0 = 5 E_R$ (c). The final trap depth for clock spectroscopy in each of the cases is $U_0 = 8.5 E_R$, while the lattice wavelength was 467.50 nm. The red solid line is a fit composed of a linear combination of the previously described base functions.

up again was each 100 ms. In each of the scans, the final lattice depth was $8.5 E_R$, being limited by the available power of the Ti:Sa laser at a lattice wavelength of 467.50 nm. The red solid curve is again a fit comprising a set of base functions of Subsection 4.3.3. As can be seen from the different scans, one clearly loses atoms, if the lattice intensity is initially decreased, indicated by the smaller signal amplitude. Moreover, the high-frequency wings of the resonance are suppressed if Figure 5.6 (c) is directly compared to (a), indicating that the observed spectral feature is composed by resonances belonging to several different trap depths. In fact, the optical lattice is loaded out of the elongated dipole trap, while the latter has a confocal parameter of $b \approx 3$ cm. Within this range, the atomic cloud would be distributed over 130,000 lattice sites, experiencing trap depths from $5.7 E_R$ up to $8.5 E_R$ at the position of the lattice waist. If the lattice intensity is reduced during the purification sequence (see Subsection 3.3.2), atoms can no longer be captured in the shallower outer parts and will be released from the trap. As the lattice features a detuning of the magic wavelength, this shallow-trap contribution especially causes an inhomogeneous broadening of the carrier transition.

In Section 5.1, I have discussed that the intensity variation of the optical lattice modifies the temperature of the atomic sample and hence the occupancy of higher-order vibrational states. The measurements depicted in Figure 5.6 further suggest, that the purification sequence also modifies the ground state band population, in particular the number of atoms with initial quasimomentum between approximately $\pm 0.5 q_L$ (see Figure 4.12). Those are contributing to a positive frequency shift and hence to the right maximum of the spectral feature. Its amplitude seems to depend on the inner-band population distribution of the atoms and is obviously more pronounced, if the optical lattice is not operated at the magic wavelength. In the frame of this work, the population distribution used in the theoretical model has been considered to be uniform, hence the obtained fitting functions (red curves) do not fully explain this behavior.

In summary, the theoretical model can describe most of the physics of the *shallow lattice regime* within the spectroscopic resolution. The observation of the line shape behavior of the carrier transition at different trap depths (Figure 5.5) matches with the theoretical simulation as discussed in Section 4.3. In the experiment, the carrier resonance features a frequency shift as well as a broadening in the order of the ground state band width, which is homogeneous at the magic wavelength and obviously inhomogeneous if the lattice is detuned from the magic wavelength, giving rise to an asymmetric line shape. Concerning clock operation, any kind of line broadening directly affects the clock's accuracy. The simplest solution would hence be to perform spectroscopy in deeper lattices where tunneling is suppressed. Coming to the last part of this section, I will discuss how this inhomogeneity can be used for the determination of certain atomic parameters, like the magic wavelength.

5.4.2 Spectroscopy of Bloch bands close to the magic wavelength

Besides the fact that the calculated atomic polarizabilities are predicting the magic wavelength for the clock transition in ^{24}Mg with a high accuracy [110] and in well agreement with the measurements, it is interesting to study the effect of unequal clock state polarizabilities on spectroscopy of Bloch bands. However, the experimental data presented in Figure 5.6 suggest, that the theoretical simulation, which has been carried out in the frame of this thesis, does not yet contain all relevant physical effects, being more pronounced at a non-magic wavelength, as discussed in the previous subsection. As an alternative, one could think of a more straight-forward approach concerning data analysis, hence skipping the complex routine of simulating data points, calculating the interpolation base function and obtaining a linear combination of several base functions for data fitting.

As has been previously mentioned, the line shape of the carrier transition in the shallow lattice regime features two maxima with respect to a negative and positive frequency shift, respectively. Furthermore, the resonance is affected by an inhomogeneous broadening, as several differently deep lattice sites contribute to the spectral feature⁵. According to Wolf and Lemonde [116], tunneling causes the Bloch states for a certain lattice band to dephase on a time scale being the inverse of the band width. In a comparable situation, an excited atom will decay on a time scale being the inverse of the natural linewidth γ . The resonance spectrum of the latter is described with a Lorentz function, so it may be arguable to fit each maximum of the observed resonance by an independent Lorentz function, while both overlap for the final function $f_{\text{fit}}(\nu)$. Although each maximum in the single-site calculated base function (see Figure 4.14, *left*) is in contradiction to a Lorentzian line shape, their sum (Figure 4.14, *right*) reminds of a composition of two resonances with different linewidths. For clarity, Figure B.1 shows such a composition in comparison to the graph of Figure 4.14 (*right*). To comment on the degree of the observed inhomogeneity of the carrier transition, several spectra for different lattice wavelengths will be discussed in the following, whereas the maxima's different linewidths, obtained via Lorentzian fits, are directly compared.

Figure 5.7 shows scans of the carrier transition recorded at lattice wavelengths below (467.50 nm), at (468.42 nm) and above the magic wavelength (468.81 nm). The lattice intensity variation during the purification phase has been chosen to be slightly below U_0 in each case, to pronounce the spectroscopic feature. Each data point has been averaged over three measurements. The red solid curve is a composition $f_{\text{fit}}(\nu)$ of two independent Lorentzian functions each fitted to the left and the right maximum of the line shape, respectively. For data analysis, the local minimum between the maxima has been chosen as reference point ν_{ref} . The width

⁵This situation may be comparable to the derivation of the axial sideband's line shape, being modified by radial motion of the atoms (see Figure 4.7).

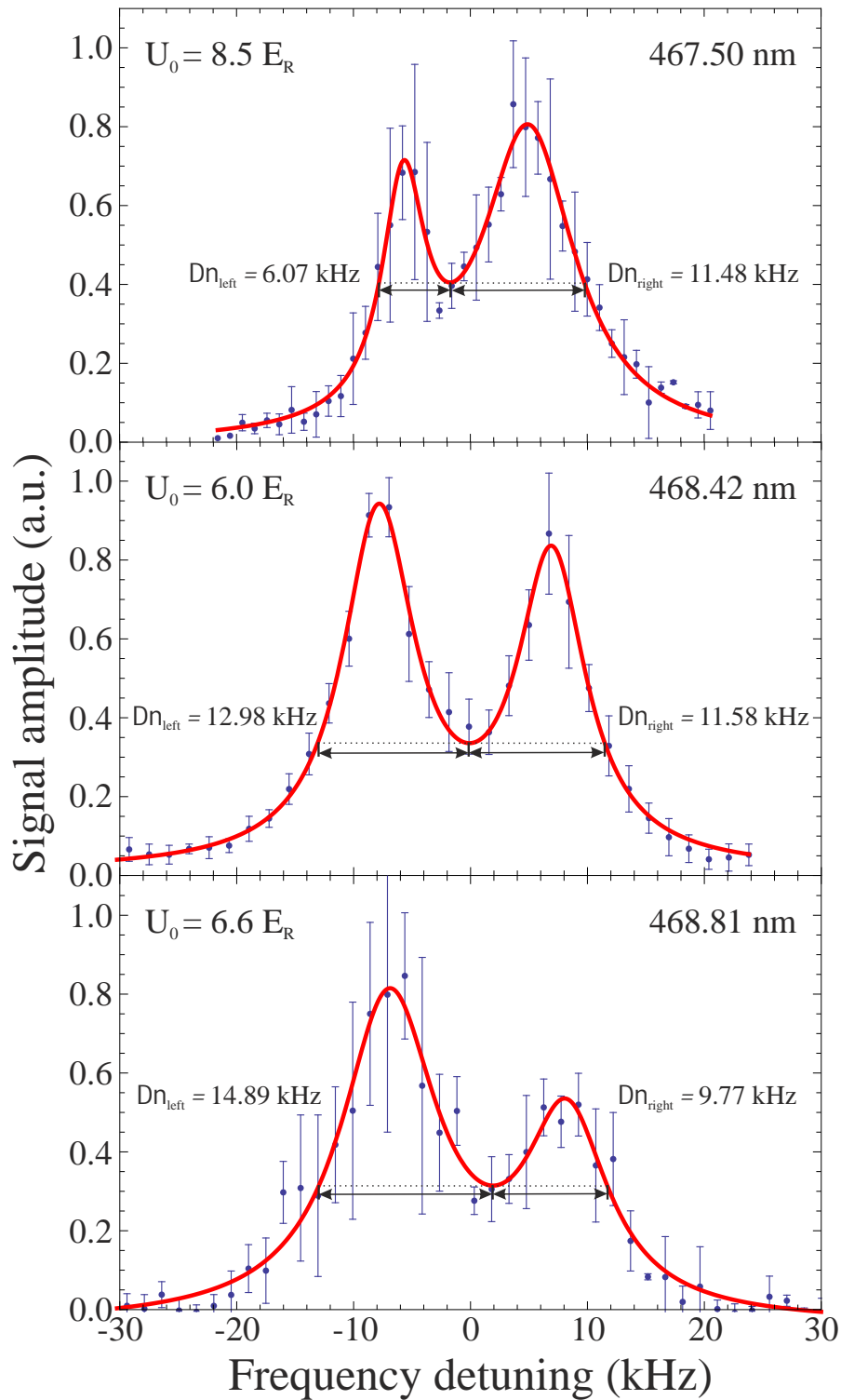


Figure 5.7: Carrier spectroscopy at different lattice wavelengths. The red solid curve is a composition of two independent Lorentz functions fitted to the left and the right maximum of the carrier line shape for analysis purposes. The ratio of the peak linewidths gives evidence on the detuning of the lattice light relative to the magic wavelength.

Lattice wavelength	467.50 nm	468.42 nm	468.81 nm
$\Delta\nu_{\text{right}}/\Delta\nu_{\text{left}}$	1.889	0.892	0.656

Table 5.3: Evaluation of the carrier resonance characteristics. The maxima's linewidth ratio suggests that the magic wavelength lies between 467.50 nm and 468.42 nm.

of the maxima shall here be defined by the frequency difference $|\nu_{\text{ref}} - \nu_{\text{left/right}}|$, where $f_{\text{fit}}(\nu_{\text{left/right}}) = f_{\text{fit}}(\nu_{\text{ref}})$. Looking at the carrier scans in Figure 5.7, the width of the right peak appears to be broader than the left one, if the optical lattice is operated below the magic wavelength (and hence the 3P_0 polarizability is larger than the 1S_0 polarizability, see Figure 4.5) and vice versa if the lattice wavelength is larger than the magic one. Hence, the ratio $\Delta\nu_{\text{right}}/\Delta\nu_{\text{left}}$ of the widths gives evidence on the detuning relative to the magic wavelength and should be proportional to the ratio of atomic polarizabilities $\alpha_{^3P_0}/\alpha_{^1S_0}$. At the magic wavelength, the line shape is expected to be symmetric and as a consequence

$$\Delta\nu_{\text{right}}/\Delta\nu_{\text{left}} = \alpha_{^3P_0}/\alpha_{^1S_0} = 1. \quad (5.3)$$

Hence, the frequency scan at 468.42 nm suggests, that the magic wavelength has to be slightly smaller than the operated lattice wavelength. However, comparing all the frequency scans with each other, the peak amplitudes also seem to change with different lattice wavelengths. According to the discussion in the previous subsection, this effect may be related to the inner-band population distribution of the atoms as well as the differential AC atomic polarizabilities. Unfortunately, this hypothesis could not be further investigated in the frame of this thesis, as a consequence of limited lattice laser power.

In brief summary, the optical spectroscopy of Bloch bands displays a tool of measuring atomic parameters, like the magic wavelength, throughout an indirect measurement of atomic polarizability ratios. Moreover, a single frequency scan per lattice wavelength contains all the relevant informations, therefore reducing the experimental effort, compared to the traditional light shift measurements, where several scans at different trap depths have to be recorded for the determination of the light shift. In principle, this method can be applied to any other atomic species used in an optical lattice clock.

The results summarized in Table 5.3 suggest, that the magic wavelength is between 467.50 nm and 468.42 nm. Figure 5.8 shows the linewidth ratios of the carrier's maxima as a function of lattice wavelength. Applying a linear regression to the data points, the magic wavelength determines to 468.394(179) nm which is consistent with the light shift measurement of 468.463(207) nm (see Section 5.2).

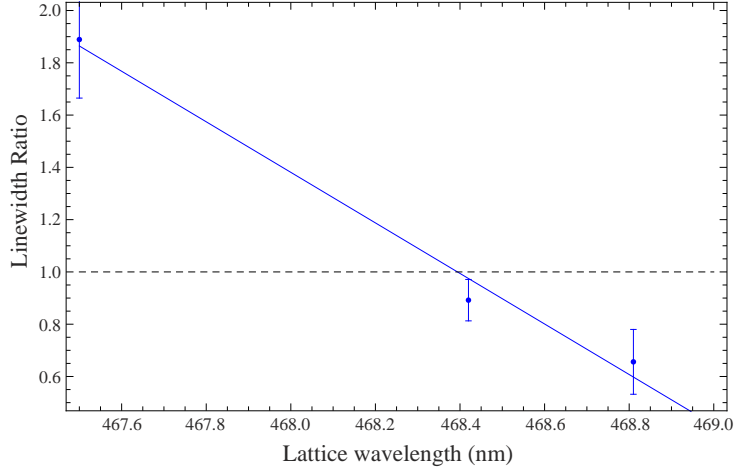


Figure 5.8: Determination of the magic wavelength via optical spectroscopy of Bloch bands. The linewidth ratios obtained in Figure 5.7 are plotted as a function of lattice wavelength. The magic wavelength, where $\Delta\nu_{\text{right}}/\Delta\nu_{\text{left}} = \alpha_{^3P_0}/\alpha_{^1S_0} = 1$, is 468.394(179) nm. The error bars are composed of the statistical uncertainties of the Lorentzian fits.

5.5 Conclusion

In this chapter, I have discussed the characterization of the optical lattice and the determination of clock relevant atomic parameters by optical spectroscopy. The measurements benefited from previous frequency measurements of the $^1S_0 \rightarrow ^3P_1$ and $^3P_0 \rightarrow ^3P_1$ transitions, whereas the difference of their frequency values determined the clock transition frequency with an accuracy of 48 Hz.

In the experiment, large axial trapping frequencies have been observed, being in the order of a few hundred kHz. However, due to its low atomic mass, a short magic wavelength and smaller atomic polarizabilities, Mg possesses a higher lattice recoil energy, as compared to Sr or Yb. As a consequence, spectroscopy in the Lamb-Dicke regime requires high laser powers, featuring small recoil energy normalized trap depths. So far, the radial trapping frequencies, expected to be a few hundred Hz, could not be resolved as the carrier linewidth features a broadening of several kHz, which is due to tunneling between adjacent lattice sites. If the radial trapping frequency was known, the lattice would be fully characterized in terms of beam waist and trap depth. Alternatively, the lattice waist was measured with a CCD camera for obtaining a complete characterization of the optical lattice.

Studying the frequency shift of the carrier transition, the magic wavelength of the $^1S_0 \rightarrow ^3P_0$ clock transition has been determined to 468.463(207) nm via lattice light shift measurements and the magnetic polarizability, measured via the second-order Zeeman shift, is $\beta = -206.6(2.0)$ MHz/T². Both values are consistent with their theoretical predictions. The knowledge of both parameters allowed for the first direct spectroscopic measurement of the clock transition frequency of 655 058 646 691(101) kHz, while beating the clock laser with an optical frequency

comb. The accuracy of this measurement is limited by the uncertainty of the comb's GPS based frequency reference.

Finally, a novel method of spectroscopy of Bloch bands is presented, carried out on the strongly forbidden optical clock transition. If the optical lattice is operated in the so-called *shallow lattice regime*, the shape of the lowest bands of the electronic ground and excited state can be mapped onto a frequency shift of the lattice carrier transition, giving rise to a resonance structure being modified by tunneling motion. In our case, atoms are distributed along the lattice axis as they are loaded out of an elongated dipole trap. As a consequence, atoms are trapped in shallower trapping regions the more far away they are from the lattice waist. Hence, as all excited atoms contribute to the total spectroscopy signal, the latter appears to be broadened. In particular, this broadening mechanism turns out to be inhomogeneous, if the lattice wavelength is detuned from the magic wavelength. However, this asymmetric line shape can be used for the determination of atomic parameters, like the magic wavelength. In particular, a single frequency scan already contains all relevant informations, reducing the experimental efforts as compared to the traditional light shift measurements. In a simplified approach of data analysis, the magic wavelength via optical spectroscopy of Bloch bands determines to 468.394(179) nm, being consistent with the previous value obtained via light shift measurements.

Outlook

Concluding this thesis, this chapter will give an overview on the immediate next steps in the experiment, based on the results that have been achieved so far, as well as on possible experiments that could be carried out in the near future. Section 6.1 describes possible ways to further increase the optical lattice depth to enable Fourier-limited spectroscopy of the clock transition. Furthermore, systematic frequency shifts for a future Mg optical lattice clock are discussed. Section 6.2 compares fermionic lattice clocks with bosonic lattice clocks opposing their most prominent (dis)advantages, before a potential way how to operate a lattice clock with fermionic ^{25}Mg is identified. To its end, future prospects for optical spectroscopy of Bloch bands and possible applications are discussed in Section 6.3.

6.1 High-precision Lamb-Dicke spectroscopy

The measurements performed in the frame of this thesis represent a fundamental starting point for a future clock operation with lattice-trapped magnesium. Although the determination of ^{24}Mg parameters, like the magic wavelength of the $^1S_0 \rightarrow ^3P_0$ clock transition or the magnetic polarizability β , has been carried out at sufficient precision, their uncertainties can be further reduced, if the optical lattice is operated at deeper trap depths and hence tunneling between adjacent lattice sites is suppressed. Approaching linewidths on the order of ~ 10 Hz, the optical lattice can be fully characterized via resolved radial sideband spectroscopy, obtaining a complete picture of lattice depth and waist.

In this thesis, the available output power of the Ti:Sa laser at 936 nm (which is the fundamental wavelength of the lattice light) was limited to maximum 550 mW due to degrading laser diodes of the Verdi pump laser. In the ongoing work [128], the old pump laser has already been replaced by a new one¹ with a maximum

¹Verdi G12, Coherent

pump output power of 12 W. As a consequence, the available Ti:Sa power could already be enhanced to at least 1.3 W at 936 nm. A more compact setup of the overall laser system, including the SHG stage for 468 nm and a shorter glass fiber for transportation to the lattice setup, is conservatively expected to give at least 200 mW at 468 nm available for coupling into the lattice enhancement cavity.

6.1.1 Increasing the lattice trap depth

As can be seen from Eq. 4.38, the lattice well depth is depending on the lattice power and the lattice waist. Concerning the power, the incident laser light is enhanced in our 1D build-up cavity passing through the vacuum chamber. Here, round trip losses due to imperfect optic coatings (ideally highly reflective in the case of cavity mirrors and highly transmissive chamber viewports) limit the maximal achievable power enhancement. The cavity enhancement factor is given by

$$g \simeq \frac{\mathcal{F}}{\pi} \quad (6.1)$$

where $\mathcal{F} = \pi\sqrt{R}/(1 - R)$ is the resonator's finesse [83, 91, 129]. For the measurements presented in this thesis, the cavity enhancement factor was about 25, corresponding to a total cavity reflectivity of $R \simeq 0.96$. With the above anticipated fiber-coupled laser power of 200 mW at the magic wavelength, a circulating lattice power of 5 W is expected. Featuring a lattice waist of $w_0 = 79 \mu\text{m}$, the resulting trap depth will be $U_0 = 28.6 E_R$ giving rise to a ground state band width of approximately 87 Hz (see Figure 4.11). In terms of clock spectroscopy, this already represents a linewidth limitation improvement of almost two orders of magnitude. There are two possibilities for a further increase of the lattice trap depth:

- (i) A reduction of the lattice waist would automatically lead to an increase in lattice depth and displays an easy-to-implement solution, as the corresponding optical lenses are mounted on translation stages [91]. A waist of $w_0 = 69 \mu\text{m}$ would already lead to a trap depth of $U_0 = 37.5 E_R$ and hence a ground state band width of 23 Hz.
- (ii) So far, the lattice optics feature a broad band coating with reduced reflectivity as we had initially been prepared to measure the magic wavelength in a range of 460 – 470 nm. As the uncertainty of the magic wavelength has been reduced to 0.207 nm in the frame of this thesis, new cavity optics could be purchased offering a high-reflection coating for $\lambda_{\text{magic}} = 468.463(207) \text{ nm}$. If it was possible to obtain an incoupling mirror optimized for impedance matching of round trip losses at the magic wavelength and being highly transmissive for the clock laser at 458 nm², one could even change the lat-

²Featuring a broad band coating with a reflectivity of a few percent and a high transmission at 458 nm at the same time had been impossible in the past [91].

	w_0 in μm ($P = 5 \text{ W}$)			g ($w_0 = 79 \mu\text{m}$)		
	59	69	79	25	33	50
U_0 in E_R	51.4	37.5	28.6	28.6	37.8	57.3
ΔE in Hz	4	23	87	87	22	2

Table 6.1: Calculated lattice trap depths and ground state band widths for different configurations of lattice waist and cavity enhancement. The incident laser power in each case is 200 mW at λ_{magic} .

tice setup to a two-mirror resonator, further reducing light losses on optics. However, as the vacuum windows that had been replaced in the frame of this thesis, again show a reduced transmission for the magic wavelength due to a contamination on the vacuum side or optical coating damages as a consequence of the intense blue lattice power, they could be replaced as well by the already available ones featuring optimized coatings for the optical traps (see Section 2.1). Estimating the total cavity reflectivity with $R \simeq 0.98$, if all these optimizations were executed, would result in a cavity enhancement factor of $g \simeq 50$ and a circulating power of 10 W. As a consequence, the lattice trap depth would be $U_0 = 57.3 E_R$ featuring a ground state band width of approximately 2 Hz. Obtaining a spectroscopic linewidth of this order of magnitude in magnesium would already be competitive with state-of-the-art strontium or ytterbium optical lattice clocks.

Table 6.1 gives an overview on the maximum trap depth for different configurations of the lattice waist w_0 and enhancement factor g , assuming a fiber-coupled laser power of 200 mW at the magic wavelength.

As some frequency shifts and broadening effects presented in this thesis (see Section 5.4) are a consequence of tunneling and the corresponding delocalization of atoms, localization could be established by introducing an acceleration to the optical lattice, e.g. provided by the gravitational force [116]. In this case, each lattice site will be shifted by

$$\Delta E_g = m_{\text{Mg}} g \frac{\lambda_{\text{magic}}}{2} \sin \theta, \quad (6.2)$$

where m_{Mg} is the mass of the magnesium atom, g is the gravitational acceleration and θ is the angle between the horizontal plane and the direction of gravity, therefore reducing the influence of tunneling between adjacent potential wells. A vertical orientation of the magic wavelength lattice, being under maximum influence of gravity, then corresponds to an energy spacing of $\Delta\nu = 138 \text{ Hz}$. Accordingly, any combination displayed in Table 6.1 would allow for spectroscopy in a tunneling-suppressed regime. However, the current experimental setup, as described in Subsection 3.3.2, does not allow for the implementation of a vertical

lattice for several reasons: On the one hand, the z -viewports would have to be replaced, as the coating is optimized for the operation of the UV MOTs, on the other hand, the magnetic quenching field ideally needs to be oriented perpendicularly to the lattice axis and hence the clock laser axis, as can be seen from Eq. 3.6.

Nevertheless, a tilt of $\theta = 5^\circ$ could be introduced with the current lattice optics generating an energy spacing of at least $\Delta\nu = 12$ Hz. If tunneling effects shall be fully inhibited in future, ground state band widths of the same order need to be realized, which should be the case for trap depths of $U_0 = 45 E_R$ and higher, as depicted in Figure 4.11.

6.1.2 Purification of the atomic ensemble

Once the spectroscopic linewidth is reduced down to the Fourier limitation on the order of several 10 Hz, some effects will dominate the line shape of the carrier transition, e.g. the excitation of multiple transitions $\Omega_{n,n}$, if multiple axial motional bands are occupied (see Subsection 4.2.2), or the radial temperature acting on the Rabi frequency as well as on the carrier line shape, as described in Subsection 4.2.3.

As we have seen in Sections 5.1 and 5.4, a variation of the lattice intensity down to shallow depths before the spectroscopy pulse is applied, modifies the atomic temperature and hence the occupancy of higher-order vibrational states. Nevertheless, the latter may not fully be emptied, so one might apply some additional state-selective purification to these. A possible scheme is depicted in Figure 6.1. An additional 457 nm laser beam being red-detuned by $\nu_L = \nu_0 - \nu_z$ from the clock transition, could be irradiated to eliminate contributions from the first red sideband. Atoms excited to the 3P_1 state, that are immediately pumped to the 3D_2 state by means of RP 2 in presence of the lattice light, will be exposed to photoionization caused by lattice photons [64], and should consequently leave the optical trap³.

An alternative method, which in addition should allow for reduction of atomic temperature, is given by sideband-resolved laser cooling [28]: If the $^1S_0 \rightarrow ^3P_0$ clock laser is tuned to the frequency of the first red sideband, lattice-trapped atoms will absorb photons with energy $h\nu_L = h(\nu_0 - \nu_z)$ and on average re-emit photons with energy $h\nu_0$. As a consequence, each photon scattering event reduces the atomic energy by amounts of $h\nu_z$ with atoms finally occupying the vibrational ground state of the trap. However, this scheme might be applicable in a limited way only, as the 3P_0 state features a long life time.

³In addition, the photon recoil at 383 nm applied to the ~ 20 MHz broad transition should push the atoms out of the trap.

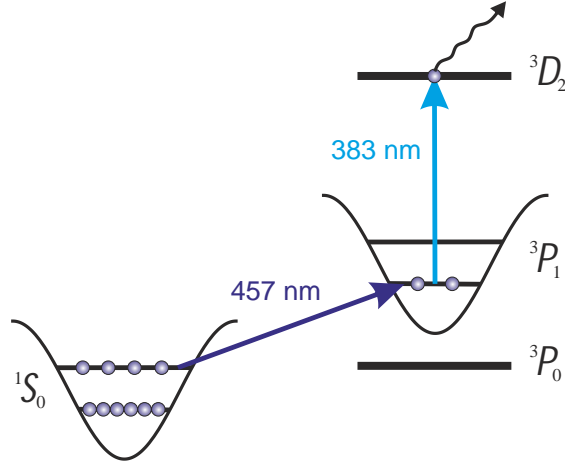


Figure 6.1: Possible scheme for purification of higher-order axial vibrational bands in the 1S_0 ground state. Atoms are excited on the $^1S_0 \rightarrow ^3P_1$ transition at 457 nm being red-detuned with respect to the first red sideband's frequency. If 3P_1 atoms are subsequently pumped to the 3D_2 state, photo ionization will occur in the presence of the lattice light. The latter will not necessarily be at the magic wavelength for 3P_1 .

6.1.3 Towards an optical lattice clock with magnesium

Heading towards a frequency measurement of the strongly forbidden $^1S_0 \rightarrow ^3P_0$ transition in lattice-trapped magnesium atoms, several requirements have to be accomplished in the experiment. The most crucial part is to analyze the reasons for thermal disequilibrium of the clock ULE cavity at 916 nm. As it has been mentioned in Section 5.2, residual (nonlinear) clock laser drifts as large as 2 – 3 kHz in several minutes occurred during the measurements, being inapplicable for Hz-spectroscopy of the clock transition. Here, the clock laser system needs to be improved to reach again the demonstrated low drift rate of 150 mHz/s (or equivalently 4.6×10^{-16}) [93].

Normalization of the atomic signal

To provide a sufficiently high and reliable S/N ratio of the clock transition, the knowledge of the total number of atoms being prepared in the optical lattice is crucial for normalization of the spectroscopy signal. For the measurements presented in this thesis, atoms have been prepared in the 1S_0 ground state offering an improved S/N ratio for spectroscopy as compared to previous measurements [66], where the clock transition had been interrogated by optical disexcitation of atoms prepared in the 3P_0 state. As it has been demonstrated in this thesis, ramping down the lattice intensity displays a first-order purification of the trapped atomic ensemble. Accordingly, we might again operate the magnesium clock in future starting out from the 3P_0 state, avoiding further photon recoil heating by optical depumping to the 1S_0 ground state. A possible detection scheme of atoms could

thus look as follows:

- (1) After the clock laser pulse has been applied, lattice trapped atoms will be transferred to the optical dipole trap at 1064 nm, which already has been evaluated with an efficiency of $\sim 100\%$. The remaining atoms N_e in the 3P_0 state can now be detected in absence of the lattice light using the triplet-MOT beams, hence avoiding photo ionization effects.
- (2) Atoms that have been disexcited to the 1S_0 ground state, will be optically repumped to the triplet manifold via the $^1S_0 \rightarrow ^3P_1$ transition. Detection is again carried out with the triplet-MOT yielding N_g .
- (3) The normalized spectroscopy signal results to $N_g/(N_g + N_e)$.

This detection scheme requires two pictures to be taken of the atoms. As the read-out of the currently used CCD camera turned out to be too slow for two consecutive images, the second number of atoms N_g could alternatively be recorded by means of a PMT. The opto-mechanical setup and the implementation into the LabView computer control is subject of an ongoing work in our group [128]. However, this proposed normalization scheme benefits from background-free detection with the triplet-MOT showing a sensitivity to a few tens of atoms, as metastable magnesium only occurs throughout laser excitation in our experiment. Exemplarily, in Yb, the strong $^1S_0 \rightarrow ^1P_1$ transition is used for optical detection of atoms N_g [123]. After clock interrogation, excited atoms are repumped to the 3D_1 state with further decay to the 1S_0 ground state. Again, the singlet-MOT transition is used to measure N_e . However, in this scheme additional atoms may be excited from the background gas leading to an error in the number of atoms.

Lattice induced frequency shifts

The measurements on the magic wavelength of the $^1S_0 \rightarrow ^3P_0$ clock transition in Section 5.2 yielded a linear dependence of the differential AC Stark shift on lattice depth and wavelength of $1.669(115)$ kHz/ E_R /nm. Aiming for a fractional clock uncertainty of 1×10^{-18} (equivalent to 0.65 mHz), this sensitivity sets a requirement on frequency stability of the lattice laser for a given trap depth U_0 (expressed in E_R) to the level of $3.9 \times 10^{-7}/U_0$. In Subsection 6.1.1, the ideal trap depth for future lattice clock operation has been estimated with $U_0 = 45 E_R$, hence the lattice laser has to be stabilized on the level of 8.7×10^{-9} , corresponding to 10 kHz stability. In parallel to this work, the stabilization scheme for the lattice laser is under development. The Ti:Sa frequency will in future be locked in the infra-red at 936 nm to a transfer cavity, whose length will be stabilized to the high-finesse clock cavity, providing a frequency stability being well below the above mentioned requirements [130].

As expressed by Eq. 4.44, the clock transition energy is not only modified by the differential AC polarizability. In higher order, hyperpolarizability effects will also have an impact on the transition frequency. The largest contribution to the hyperpolarizability is given by two-photon transitions being near resonant to the magic wavelength of the optical lattice [89, 131]. However, in the case of magnesium, there are no two-photon transitions known so far corresponding to 2×468.463 nm [132, 133], accordingly hyperpolarizability effects should be suppressed.

Black body radiation shift

The black body radiation (BBR) shift arises from perturbations of the atomic energy levels caused by time varying thermal radiation and is given by

$$\Delta\nu_{\text{BBR}} = -\frac{1}{2\hbar}\Delta\alpha \langle E^2 \rangle_T + \Delta\nu_{\text{dyn}}(T), \quad (6.3)$$

where $\Delta\alpha$ is the differential static polarizability, $\langle E^2 \rangle_T \sim (8.319 \text{ V/cm})^2 (T/300 \text{ K})^4$ is the mean squared electric field of the BBR radiation at temperature T and $\Delta\nu_{\text{dyn}}$ is a dynamical correction that has to be included in the total BBR shift [36]. $\Delta\nu_{\text{dyn}}$ is derived from the combination of theoretical calculations and measurements of the 3D_1 state lifetime [40, 134].

Both clock states are affected by BBR and $\Delta\nu_{\text{BBR}}$ displays the difference of the shift for the two levels. Porsev and Derevianko calculated the BBR shift for the $^1S_0 \rightarrow ^3P_0$ clock transition in Mg to be $-0.258(7)$ Hz (or equivalently $-3.9(1) \times 10^{-16}$ in fractional frequency shifts) at $T = 300$ K, being one order of magnitude smaller as the calculated shifts in Sr and Yb [63]. The refined atomic structure model for magnesium, that has also been used for the most recent calculation of the magic wavelength [110] (see Subsection 4.2.2), predicts a static BBR shift to be eight and five times lower than those of Sr and Yb, which were recently measured [36, 37]. The dynamic contribution for the 3P_0 state has been estimated to be 0.1 % in Mg, being remarkably smaller than for Yb (1 %) or Sr (4 %) [63, 135].

Other systematic shifts and cancellation techniques

The large second-order Zeeman shift, that has been calculated for magnesium [67, 124] and was confirmed by the measurements presented in this thesis, displays a dominant contribution to the error budget of our magnesium clock and puts tight constraints on the knowledge of the magnetic field with respect to accuracies of state-of-the-art optical clocks. However, enhancing the dipole coupling of the ground state 1S_0 to 3P_0 with a magnetic field, allows to arrange a trade-off between the clock laser induced AC Stark shift and the quadratic Zeeman shift. According to the measurements performed in the frame of this thesis, a clock laser intensity of 7.07 W/cm^2 and a magnetic field amplitude of 10 G (equivalent to 1 mT) will yield a reasonable Rabi frequency of 8 Hz, a second-order Zeeman shift of $-206.6(2.0)$ Hz

and an estimated clock AC Stark shift of -3.5 Hz. To reach a fractional clock uncertainty of 1×10^{-18} , i.e. 0.65 mHz in absolute frequencies, with an applied magnetic field of 10 G, the field amplitude needs to be stabilized at the level of $16 \mu\text{G}$. However, this level of accuracy also puts a constraint on the knowledge of the Zeeman coefficient β : If the magnetic field is stabilized with an uncertainty of $16 \mu\text{G}$, the value of β has to be measured to the level of 4×10^{-8} , displaying a challenging restriction for future experiments.

Although the major systematic shifts for a future magnesium optical lattice clock, the lattice AC Stark and second-order Zeeman shifts, have been measured on a decent level of precision, their uncertainties can be further reduced, if clock spectroscopy is performed on a Fourier-limited linewidth level on the order of ~ 10 Hz. This regime will then also allow for the determination of other systematic effects, e. g. the clock laser induced AC Stark shift, that could not be resolved so far in the frame of this work due to observed transition linewidths of several kHz. Taichenachev *et al.* calculated the clock laser AC Stark shift coefficient in Mg to be $\kappa = -0.5 \text{ mHz}/(\text{mW}/\text{cm}^2)$ [67]. As has been mentioned above, the expected frequency shift with the current clock laser intensity is about -3.5 Hz.

However, there are strategies to eliminate residual AC Stark shifts, Zeeman shifts and others, that are present during the interaction with the clock laser. In a generalized Ramsey excitation scheme, the so-called "hyper-Ramsey" scheme, the probe laser frequency is adjusted by means of the frequency shifts. In addition, the pulse durations and phases are modified that, in the end, a suppression of the clock laser AC Stark effect has been demonstrated in [136] and a related scheme [137]. If we implemented these techniques in our experiment, bosonic magnesium becomes a favorable candidate for optical lattice clocks.

6.2 Fermions vs. bosons

There are two prominent advantages for lattice clocks to use fermions, as opposed to bosons. First, spin-polarized fermions are expected to show a reduced collisional frequency shift (CFS), as they obey the Pauli exclusion principle. Accordingly, one either operates with bosons in a 3D optical lattice with single-site occupancy to fully suppress collisions or one precisely determines the CFS in a 1D lattice and keeps the atomic density low and well controlled. Comparing a ^{87}Sr [138] and a ^{88}Sr [139] lattice clock, both being at a comparable state of development at that time, yields no limitation for the bosonic clock due to collisions, as Lisdat *et al* carefully designed their lattice geometry. In fact, the uncertainties of the CFS for both clocks were in the low 10^{-17} regime. As the development of lattice clocks concentrated more on fermionic isotopes, state-of-the-art ^{87}Sr clocks nowadays exhibit a density shift of $-3.5 \pm 0.4 \times 10^{-18}$ [40]. For clarity, the density shift reported for the ^{88}Sr clock in [139] is $7.2 \pm 2.0 \times 10^{-17}$, where 2×10^4 atoms were distributed over 1,400 lattice sites (corresponding to a mean occupancy of approximately 14

atoms per lattice site). In the case of our bosonic ^{24}Mg atoms, we load the optical lattice out of the elongated dipole trap at 1064 nm. We measured the number of atoms being available for clock spectroscopy after the lattice purification phase to be $\sim 1,000$ atoms, where we estimate the ensemble to be distributed over 1.3×10^5 lattice sites. Hence, the mean occupancy here is about 0.008 atoms per lattice site, being three orders of magnitude smaller as compared to [139]. As a consequence, a 3D optical lattice for ^{24}Mg will not be required, as collisions should play a minor role in our clock. Nevertheless, the density shift for magnesium has to be experimentally determined at some point.

Second, fermions are favorable candidates for lattice clocks as they exhibit a nuclear spin, naturally causing a hyperfine-mixing of the 3P_0 and 3P_1 states. Hence, a magnetic quenching field is not necessary for enabling spectroscopy of the strongly forbidden $^1S_0 \rightarrow ^3P_0$ clock transition, keeping the second-order Zeeman contribution to the clock's uncertainty budget on a remarkably low level as compared to their bosonic counterparts.

6.2.1 Challenges for fermionic isotopes

Nevertheless, one also has to take into account the disadvantages that fermionic clocks are facing. The presence of a nuclear spin gives rise to either a vector shift that occurs through interaction with residual elliptical polarization of the lattice light [114, 140] and a tensor shift being roughly proportional to the ratio of the hyperfine splitting of the coupled electronic state and the lattice laser detuning to that state [32]. However, these shifts can be experimentally determined in presence of a small bias magnetic field: as the degeneracy of the m_F substates is lifted, the frequency splitting of neighboring components gives rise to the shift coefficients [141].

Although the second-order Zeeman shift for fermions is fairly low, they are facing a strong linear sensitivity which is, for π -transitions with $\Delta m_F = 0$, given by $\Delta f = -m_F \delta g \mu_0 B$ [142]. Here, μ_0 is the Bohr magneton and δg the differential g -factor of the two clock states. As a π -transition is sensitive to δg , a σ -transition ($\Delta m_F = \pm 1$) is sensitive to both δg and g_I , the nuclear g factor. Analogously to the measurement of the residual lattice-dependent shifts, a measurement of the frequency splitting of both π - and σ - transitions yields the value of δg .

However, there are ways to eliminate the first-order m_F -dependent shifts, such as the lattice vector and the linear Zeeman shift. Equal m_F components with opposite sign feature the same absolute frequency shift, but with opposite sign. Accordingly, the average transition frequency $^1S_0(F, \pm m_F) \rightarrow ^3P_0(F, \pm m_F)$ of these m_F components is no longer dependent on the linear shifts and is equal to the perturbation-free value [53, 143]. For this reason, atoms are usually state-prepared in opposite m_F states throughout spin-polarization, whereas the clock transition is interrogated in interleaved measurements of the corresponding $\pm m_F$ component.

However, after this process of spin-polarization, some atoms may remain in neighboring m_F components. Transitions driven from there will lead to a line-pulling by means of an inhomogeneous broadening of the clock transition [55].

Finally, an s-wave frequency shift for fermions can arise, if the clock interrogation field exhibits spatial inhomogeneities. Hazlett *et al.* demonstrated that, in this case, fermions become distinguishable, giving rise to a CFS [144].

6.2.2 The fermionic ^{25}Mg

As has been mentioned in Section 3.1, there is one stable fermionic isotope for magnesium, ^{25}Mg , with a nuclear spin of $I = 5/2$. Laser cooling of the fermion in the singlet-MOT at 285 nm has been achieved in a previous work of our group [71], trapping $10^4 - 10^5$ atoms at a temperature of 4 mK, being slightly hotter than the MOT for ^{24}Mg . The small number of atoms is probably limited by the natural abundance of 10% only, but in principle does not display an overall limitation. Using appropriate oven designs with corresponding slowing schemes of the thermal beam might increase the atomic flux into the fermionic singlet-MOT [145].

The 1S_0 ground state of ^{25}Mg offers a hyperfine structure being suitable for sub-Doppler cooling techniques like polarization-gradient cooling [146]. These cooling effects have also been studied in [71], but unfortunately sub-Doppler temperatures could not be demonstrated, as the hyperfine splitting of the 1P_1 state cannot be resolved in presence of the broad $^1S_0 \rightarrow ^1P_1$ transition linewidth of 78 MHz and the calculated capture velocity of the sub-Doppler force turned out to be smaller compared to the recoil velocity of magnesium.

In principle, the state preparation scheme for the bosonic ^{24}Mg (see Chapter 3) could be adapted to the fermion as well, but one has to face the fact that the fine structure of each state 3P_J in the triplet manifold of ^{25}Mg further possesses a hyperfine structure. This leads to a variety of possible transitions that have to be covered by additional laser beams at 383 nm, if one wants to operate a triplet-MOT, immensely increasing the experimental complexity of the existing laser system at 383 nm.

The optimal solution would be a cooling mechanism in the singlet manifold leading to temperatures of several 100 μK , which might be given by quench-cooling on the $^1S_0 \rightarrow ^3P_1$ intercombination line [147, 148] or other schemes. Achieving such low temperatures, we could apply the optical dipole trap at 1064 nm as energy filter, similar as in [64, 65] for optical trapping of a cold fraction of atoms in the 1S_0 ground state. As a next step, these atoms would be transferred to the optical lattice, as mentioned in Chapter 3, followed by optical clock spectroscopy. The frequency of the $^1S_0 \rightarrow ^3P_0$ clock transition in ^{25}Mg is already known to be 655 060 050 580(120) kHz, including the isotope shifts of the $^1S_0 \rightarrow ^3P_1$ transition between ^{24}Mg and ^{25}Mg as well as the determined center-of-gravity frequency of the $^3P_1 \rightarrow ^3P_0$ fine-structure transition in ^{25}Mg [57, 149, 150]. Furthermore, the

same clock laser at 458 nm could be used for interrogation of the clock transition.

6.3 Prospects for optical spectroscopy of Bloch bands

As we have seen in Section 5.4, the carrier line shape observed in the shallow lattice regime is sensitive to both the lattice intensity and wavelength enabling the precise determination of wavelength dependent atomic parameters. To further improve our studies on atomic properties, we need to gain more insight into the impact of lattice band filling and the corresponding population distribution on the spectroscopic line shape.

Study of lattice dynamics

So far, mapping of the Bloch band curvatures onto a frequency shift has been demonstrated, if clock spectroscopy is carried out in the shallow lattice regime. A variation of the lattice intensity to shallower depths for purification of higher-order bands seems to modify the population distribution of atoms in the ground state band (see Subsection 5.4.1). For a full understanding of the lattice dynamics, the behavior of the population distribution needs to be further investigated. Here, the use of absorption detection of the atomic cloud seems to be unavoidable. If the lattice intensity is ramped down adiabatically, therefore preserving the crystal momentum, Bloch states in the ground state band were demonstrated to be mapped onto a free-particle momentum in the first Brillouin zone [127]. Accordingly, a uniform mixture of Bloch states and hence a uniform distribution of quasimomenta will cause the atomic cloud to expand in a square box of width $2\hbar k_L$ after release of the trap. As an alternative, this free-particle momentum may eventually also be observed in terms of a frequency shift, if the narrow linewidth clock transition is probed during free-fall with subsequent monitoring of the excited state fraction.

Thermometry in optical lattices

Determination of atomic temperatures in optical lattices is a crucial part. One method is given by analyzing the contributions from the first axial sidebands (see Section 5.1) for lattice states being populated according to a Boltzmann distribution. Recently, a new method for 3D thermometry has been demonstrated for Sr₂ molecules being trapped in the Lamb-Dicke regime of a 1D optical lattice [151]. Here, the carrier spectrum features an asymmetrically broadened line shape being temperature dependent, as it is shifted by ~ 100 kHz due to a lattice AC Stark effect with $\alpha_{3P_0}/\alpha_{1S_0} \neq 1$. The carrier transition itself shows a FWHM linewidth on the order of ~ 20 kHz. Analyzing the carrier line shape, McDonald *et al.* not only

demonstrated the measurement of 3D temperatures instead of just a 1D temperature measurement, as in case of sideband thermometry, this method also turned out to be one order of magnitude more sensitive.

However, as it has already been demonstrated in the frame of this thesis, the variation of the lattice intensity modifies the ground state band population. Hence, we also might perform carrier thermometry in the shallow lattice regime. In our case, the tunneling induced line shape is much more sensitive to the detuning of the lattice wavelength, as in [151] the lattice needs to be detuned by tens of nanometers.

Properties of a compact triplet-MOT

As it has been mentioned in Subsection 3.2.3, the new alignment of the triplet-MOT beams leads to a compact and highly fluorescent cloud of atoms. In the following, I will briefly introduce some MOT properties resulting from this nouveau regime.

MOT dynamics are governed by several types of collisions: Collisions of atoms with the background gas are referred to as *linear losses*, while collisions between trapped atoms are described via *two-body losses*. The resulting reaction rate can either be determined throughout the losses of atoms from the trap or during the loading process [152]. The net loading rate is described by

$$\dot{n} = L_n - \Gamma n - \beta n^2, \quad (\text{A.1})$$

with n being the atomic density, L_n is the linear loss rate and β the two-body-loss coefficient. A solution to above equation is given by

$$n = n_{\text{SS}} \left(\frac{1 - e^{-\gamma t}}{1 + \xi e^{-\gamma t}} \right) \quad (\text{A.2})$$

where n_{SS} is the steady-state density and

$$\gamma = \Gamma + 2\beta n_{\text{SS}}, \quad (\text{A.3})$$

$$\xi = \beta n_{\text{SS}} / (\beta n_{\text{SS}} + \Gamma) \quad (\text{A.4})$$

are the total trap loss rate and the cold collision fraction, respectively, as stated in [153].

Figure A.1 shows the number of triplet-MOT atoms as a function of MOT holding time. The solid curves are fits corresponding to Eq. A.2. There are two

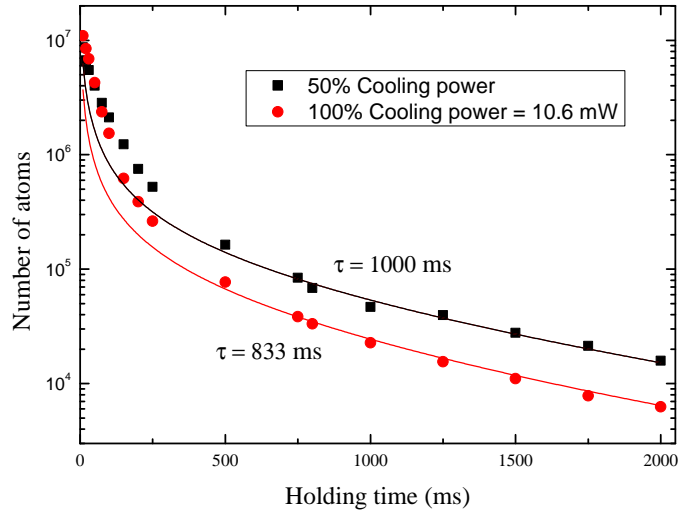


Figure A.1: Decay rate of the triplet-MOT for different cooling laser powers.

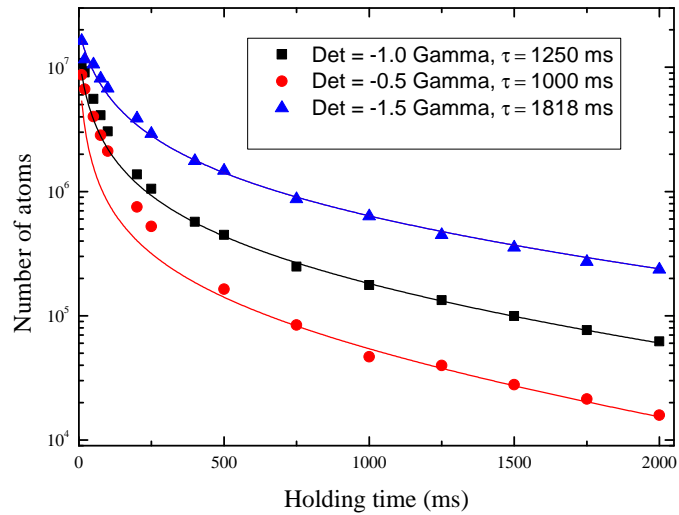


Figure A.2: Decay rate of the triplet-MOT for different cooling laser detunings. Here, 50% $\cong 5.3$ mW of the total cooling power has been used for each measurement.

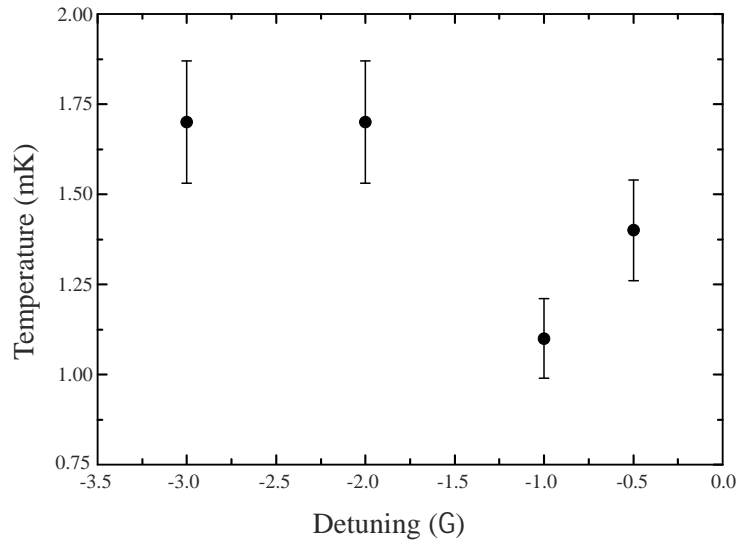


Figure A.3: TOF-temperature measurement of the triplet-MOT as a function of cooling laser detuning.

effects that can be clearly seen from the data: First, the less cooling power is used, the longer the MOT life time, which should be an indication of existing light-assisted collisions. Second of all, high-density effects that occur at short holding times are less pronounced than expected by theory. In a more compact cloud one might expect the opposite case.

Keeping the cooling power at a constant value of 5.3 mW (which is half of the maximum available power), the same decay rate has been measured for different detunings of the cooling laser. The results are depicted in Figure A.2. At a detuning of -0.5γ , the triplet-MOT life time equals the result in Figure A.1 (black curve). However, for more far-detuned cooling laser frequencies, the decay rate adapts to the expected behavior (solid lines) and shows even longer life times of the triplet-MOT.

Finally, the temperature of the ensemble has been measured for different detunings using the time-of-flight (TOF) method (see Figure A.3). The final temperature of the triplet-MOT matches with earlier measurements [64] and shows no significant dependence on the improved beam alignment.

Fitting of the carrier line shape

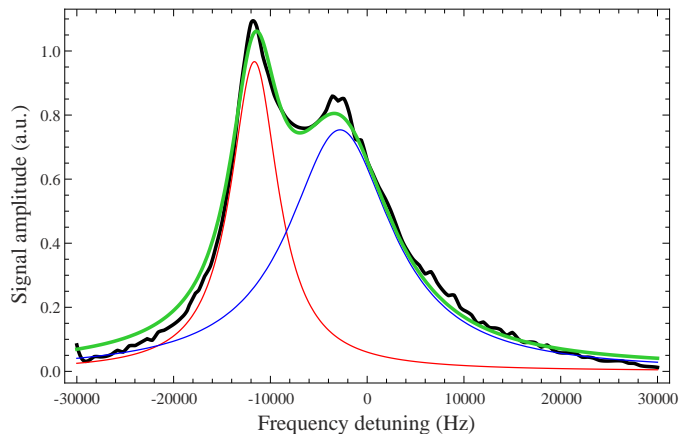


Figure B.1: Composite fit to the carrier line shape (black solid curve) in the shallow lattice regime featuring two independent Lorentzian functions (red and blue solid curves). The fit function (green solid curve) has been generated by linearly combining the Lorentzians.

In Subsection 5.4.2, it has been mentioned, that the asymmetric carrier line shape, observed in the shallow lattice regime at a lattice wavelength close to magic, reminds of a composition of two resonances. These maxima correspond to the contribution of the AC Stark modified band structure, being different for the electronic ground and excited state, which is taken care of by fitting a Lorentzian function with independent linewidth and amplitude to each of the maximum. The total fit function is given by the sum of the independent Lorentzians. For clarity, Figure B.1 shows this fit function (green solid curve) exemplarily applied to the line shape (black solid curve) obtained by summing up the simulated base functions of Figure 4.14 (*left*). In the same way, the experimental data presented in Figure 5.7 has been fitted.

Publications

In the following, publications that have been prepared in the frame of this thesis, are listed in chronological order.

- *An ultraviolet laser system for laser cooling and trapping of metastable magnesium*
A. P. Kulosa, J. Friebe, M. P. Riedmann, A. Pape, T. W. Wübbena, D. B. Fim, S. Rühmann, K. H. Zipfel, H. Kelkar, W. Ertmer, E. M. Rasel
arXiv:1201.3856v2 (2012)
- *First spectroscopy of the $^1S_0 \rightarrow ^3P_0$ transition in Lamb-Dicke confined magnesium atoms*
A. P. Kulosa, S. Rühmann, K. H. Zipfel, D. B. Fim, T. W. Wübbena, W. Ertmer and E. M. Rasel
Joint European Frequency and Time Forum & International Frequency Control Symposium (EFTF/IFC), 101-104 (2013)
- *Towards a Mg Lattice Clock: Observation of the 1S_0 - 3P_0 Transition and Determination of the Magic Wavelength*
A. P. Kulosa, D. Fim, K. H. Zipfel, S. Rühmann, S. Sauer, N. Jha, K. Gibble, W. Ertmer, E. M. Rasel, M. S. Safronova, U. I. Safronova, S. G. Porsev
Phys. Rev. Lett. **115**, 240801 (2015)
DOI: 10.1103/PhysRevLett.115.240801

An ultraviolet laser system for laser cooling and trapping of metastable magnesium

A. P. Kulosa, J. Friebe, M. P. Riedmann, A. Pape, T. W. Wübbena, D. B. Fim, S. Rühmann, K. H. Zipfel, H. Kelkar, W. Ertmer, and E. M. Rasel

Leibniz Universität Hannover, Welfengarten 1, D-30167 Hannover, Germany
phone: +49 (0)511-762-19203, fax: +49 (0)511-762-2211, e-mail: rasel@iqo.uni-hannover.de

The date of receipt and acceptance will be inserted by the editor

Abstract We report on a reliable laser system for cooling magnesium atoms in the metastable 3P manifold. The three relevant transitions coupling the 3P to the 3D manifold are near 383 nm and separated by several hundred GHz. The laser system consists of three diode lasers at 766 nm. All lasers are frequency stabilised to a single pre-stabilised transfer cavity. The applied scheme for frequency control greatly reduces the complexity of operating three lasers combined with resonant frequency doubling stages and provides a high reliability necessary for complex atomic physics experiments.

1 Introduction

Laser manipulation of atoms is an indispensable tool in atom optics. Most experiments require the laser frequency to be stabilised, typically to an atomic transition. This can be achieved via frequency modulation spectroscopy in an atomic vapour cell if the transition originates from the ground state [1]. Applying this method to metastable transitions involves additional complexity of an electric discharge and the associated linewidth broadening [2]. In such cases, as well as in the case that the laser frequency is far from any atomic transition, one can transfer the stability of a reference laser to the target laser via a transfer cavity or a frequency comb [3,4,5]. The transfer cavity technique has been demonstrated for metastable transitions in strontium where the lasers are stabilised to independent reference cavities [6]. This approach considerably increases the complexity of the system with the number of lasers involved. Locking multiple lasers to a single cavity has been achieved using a fast scanning cavity offset lock [7]. However, the system has a feedback bandwidth limited by the scan frequency of the cavity.

In this article, we demonstrate the transfer of frequency stability of the reference laser to three independent lasers using a single transfer cavity. These lasers are around 766 nm and are frequency doubled to obtain 383 nm light needed

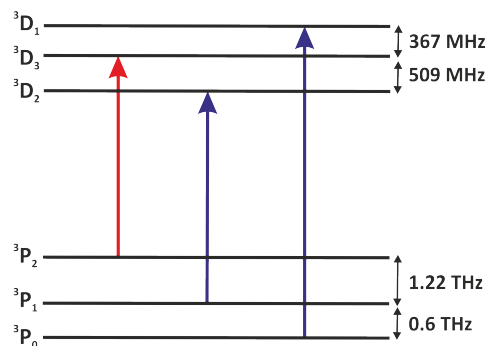


Figure 1 Relevant energy level scheme of the triplet manifold of ^{24}Mg . The red arrow depicts the closed cooling transition, whereas the blue arrows represent the repumping transitions.

to manipulate magnesium atoms in the metastable 3P manifold. The relevant metastable energy levels of magnesium are shown in Fig. 1. Each of the three laser systems consists of a master oscillator power amplifier (MOPA) feeding a cavity enhanced second harmonic generation (SHG) stage. The MOPA systems are locked to the reference cavity that is pre-stabilised to the D_2 -line of ^{39}K at 766 nm. We apply the Pound-Drever-Hall (PDH) stabilisation scheme based on diode current modulation [8]. The modulation sidebands are also used to lock the SHG cavities to the light at 766 nm. A schematic setup of the complete laser system is shown in Fig. 2.

2 The MOPA system

The three seed lasers are external-cavity diode lasers (ECDL) in Littrow configuration [9] with an output power of 50 mW. The laser diodes are anti-reflection (AR) coated and emit light at a central wavelength of 770 nm with a tuning range of ± 40 nm. The external cavity consists of a grating with 1800 lines/mm. According to the Bragg condition for the first order $\lambda = 2d \cdot \sin(\alpha)$, this results in a lasing operation for $\lambda = 766$ nm at an incident angle $\alpha \approx 43.6^\circ$. The temperature of the laser diodes is stabilised to few mK and

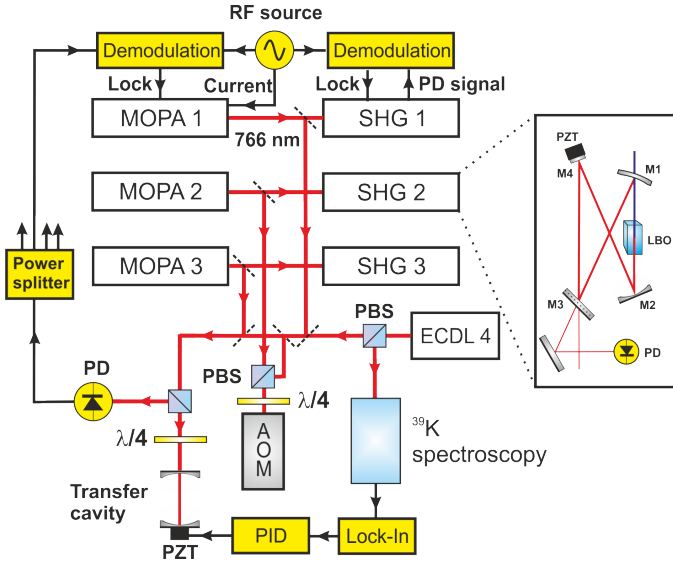


Figure 2 Simultaneous locking of three independent laser systems to a common transfer cavity referenced to an atomic transition. Each laser system is locked to the cavity using the PDH scheme. The required modulation is generated by RF local oscillators imprinting sidebands on the laser frequency via diode current modulation. The same modulation is also used to stabilise the individual SHG cavity of each MOPA. The modulation frequencies are separated by a few MHz to allow the unperturbed demodulation of each signal. The length of the transfer cavity is stabilised with the help of a fourth laser referenced to the D_2 -line of ^{39}K via Doppler-free spectroscopy. The locking scheme is shown in detail only for MOPA 1 for clarity. Blow-up: Bowtie cavity design for second harmonic generation. (PZT: piezo-electric transducer, PBS: polarising beam splitter, PD: photo diode)

an optical isolator (60 dB) protects the laser from back reflections. A tapered amplifier with a central wavelength of 765 nm is used for power amplification which is followed by an isolator (35 dB) to suppress back reflections. Each MOPA system has an output power of 1 W. A Voigt function fit to the beat measurement performed between two free-running MOPAs with a sweep time of 530 ms and a resolution bandwidth (RBW) of 10 kHz resulted in Gaussian and Lorentzian linewidths (FWHM) of 260 kHz and 35 kHz, respectively.

The frequency of each MOPA system is stabilised by locking the master lasers to a transfer cavity via the PDH method. MOPA 2, in addition, passes through an acousto-optic modulator (AOM) in double-pass configuration before the transfer cavity which allows the frequency to be scanned around the $^3P_2 \rightarrow ^3D_3$ cooling transition.

The frequency modulation sidebands for the PDH lock are generated by current modulation around 20 MHz. The differences in modulation frequency are kept large enough to distinguish the error signals of the individual MOPA. Each error signal is fed to the corresponding laser diode current for fast frequency control and to a piezo-electric transducer (PZT) for high gain at low Fourier frequencies.

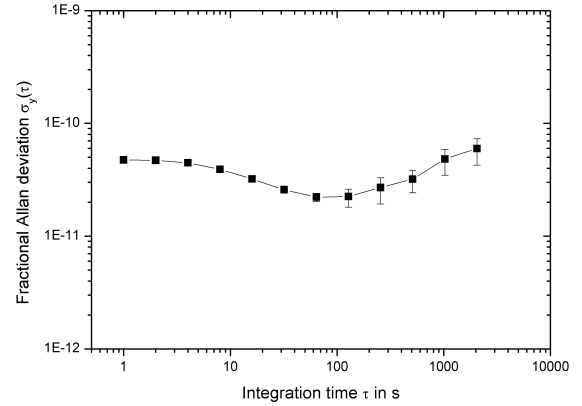


Figure 3 Fractional frequency instability of the beat note between MOPA 1 and MOPA 2 that are separated by 200 MHz and locked to the transfer cavity.

3 The length stabilised transfer cavity

The transfer cavity consists of a plane and a concave mirror (with radius of curvature $R = 100$ mm) for 766 nm separated by a quartz glass spacer of length $L = 7$ cm. One of the mirrors is attached to a PZT for controlling the length of the cavity. The finesse is determined to be $\mathcal{F} \approx 200$ while the linewidth of the resonances is 10.2 MHz. In order to lock the laser to an atomic transition frequency, it is necessary that the cavity resonance be within a few 100 MHz of the transition frequency. This can be achieved by generating a higher order mode degeneracy creating a spectrum of equidistant resonances with a spectral separation $\Delta\nu = c/(2NL)$, where $N \in \mathbb{N}$. Following the approach in [10], this can be accomplished by choosing a specific length of the cavity according to the relation

$$\frac{L}{R} = 1 - \cos^2\left(\frac{q\pi}{N}\right). \quad (1)$$

Here $q \in \mathbb{N}$, $q < N$ and q, N are mutually prime. In the experiment, $q = 6$ and $N = 19$, resulting in a mode spacing of 112.5 MHz.

The absolute length of the cavity is stabilised to an ECDL with an output power of $P = 45$ mW locked to the ^{39}K D_2 -line at 766 nm via Doppler-free saturation spectroscopy. The cavity is heated above room temperature to make fine adjustments to the cavity length to satisfy Eqn. 1 and also for temperature stabilisation.

The locking performance of the transfer cavity was determined in the time domain by locking MOPA 1 and MOPA 2 to adjacent modes of the cavity with a servo bandwidth of a few 100 kHz. The laser frequencies were separated by 200 MHz. The beat signal between the two lasers was detected with a photo diode and fed to a frequency counter with zero dead-time. The gate time for the measurement was 1 s. From the time series the Allan deviation was calculated. The result is shown in Fig. 3. The relative frequency instability reaches a value of $\sigma_y \approx 2 \times 10^{-11}$ for integration times

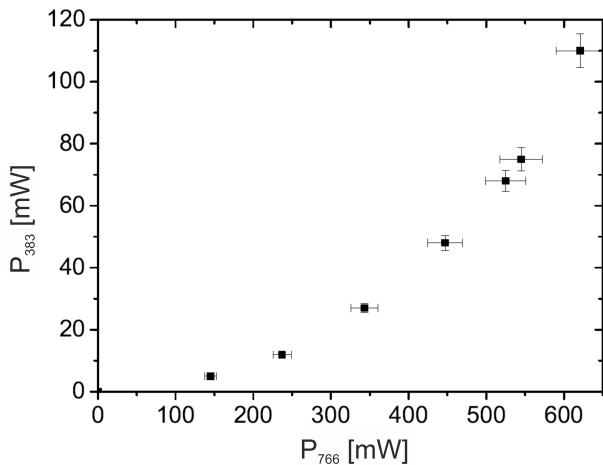


Figure 4 Generated UV power at 383 nm as a function of the power of the incident light field at 766 nm.

$\tau \approx 100$ s. The flicker floor of the lasers results from a jitter in the frequency control loop.

4 The second harmonic generation

Second harmonic generation in a 15 mm long LBO crystal placed inside a bow-tie cavity delivers more than 100 mW of power at 383 nm, corresponding to a conversion efficiency of $\approx 20\%$. Fig. 4 shows the generated power in the UV as a function of the incident power at 766 nm. The crystal is AR coated on both sides. The outcoupling mirror M1 is a miniscus (radius of curvature $R = \pm 50$ mm) to minimise the output beam divergence. Mirror M1 together with curved mirror M2 (radius of curvature = 50 mm), focus the beam to a waist of 30 μm inside the crystal. The incoupling plane mirror M3 has a transmission of 1.2%. Mirror M4 is 4 mm in diameter and attached to a PZT (Fig. 2). The total length of the cavity is about 28 cm. The finesse of the cavity is calculated to be $\mathcal{F} = 270$ from the measured linewidth of $\delta\nu = 3.93 \pm 0.2$ MHz. The crystal is temperature stabilised to room temperature.

The SHG cavity is stabilised to the light at 766 nm with the PDH scheme using the modulation sidebands generated by diode current modulation. The lock has a bandwidth of 2.5 kHz. The power fluctuations in the output beam are below 2%. A beat measurement performed between two lasers at 383 nm resulted in a Gaussian linewidth of 1.2 MHz and a Lorentzian linewidth of 25 kHz measured with a RBW of 100 kHz and a sweep time of 4 ms.

The laser system is used to realise a magneto-optical trap (MOT) for metastable 3P_2 magnesium atoms loaded from a MOT operated on the $^1S_0 \rightarrow ^1P_1$ transition in the singlet manifold. 10^9 atoms at 3 mK are transferred to the triplet manifold using the narrow intercombination transition ($^1S_0 \rightarrow ^3P_1$) at 457 nm. 1.6×10^8 atoms are then captured by the "triplet-MOT" at 383 nm where they are further cooled to 1 mK. This serves as starting point for loading them into

a dipole trap or a magic wavelength lattice for creating an optical lattice clock.

5 Summary

We established frequency stabilisation of three lasers at 766 nm to a single reference cavity whose length is pre-stabilised using a fourth laser locked to a ^{39}K spectroscopy signal. The light of the target lasers is frequency doubled to obtain more than 100 mW of UV light at 383 nm. Sidebands generated by laser diode current modulation are used for locking the lasers to the transfer cavity as well as for locking the second harmonic generation cavities to the fundamental light. Our setup reduces the complexity of operating multiple frequency stabilised lasers. In principle, it allows in the present configuration to lock up to nine lasers to the cavity limited only by its finesse. The method can also be applied to other experiments requiring multiple stabilised lasers by an appropriately designed cavity. A few examples are the sub-Doppler cooling of calcium in the metastable manifold [2], the strontium optical clock [6] and the simultaneous magneto-optical trapping of ^6Li , ^{40}K and ^{87}Rb [11], among many others.

References

1. G. Galzerano, E. Bava, M. Bisi, F. Bertinetto, and C. Svelto, *IEEE Trans. Instrum. Meas.* 48, No. 2, 540 (1999)
2. D. Hansen, and A. Hemmerich, *Phys. Rev. A* 72, 022502 (2005)
3. E. Riedle, S. H. Ashworth, J. T. Farrell, Jr., and D. J. Nesbitt, *Rev. Sci. Instrum.* 65, 42 (1994)
4. P. Bohlouli-Zanjani, K. Afrousheh, and J. D. D. Martin, *Rev. Sci. Instrum.* 77, 093105 (2006)
5. C. E. Liekhuis-Schmaltz, R. Mantifel, M. Torabifard, I. B. Burgess, and J. D. D. Martin, arXiv:1109.0338v1
6. X. Xu, T. H. Loftus, J. L. Hall, A. Gallagher, and J. Ye, *J. Opt. Soc. Am. B* 20, 968-976 (2003)
7. N. Seymour-Smith, P. Blythe, M. Keller, and W. Lange, *Rev. Sci. Instrum.* 81, 075109 (2010)
8. R. W. P. Drever, J. L. Hall, F. V. Kowalski, J. Hough, G. M. Ford, A. J. Munley, and H. Ward, *Appl. Phys. B* 31, 97 (1983)
9. L. Ricci, M. Weidemüller, T. Esslinger, A. Hemmerich, C. Zimmermann, V. Vuletic, W. König, and T.W. Hänsch, *Opt. Commun.* 117, 541 (1995)
10. D. Budker, S. M. Rochester, and V. V. Yashchuk, *Rev. Sci. Instrum.* 71, 2984 (2000)
11. M. Taglieber, A.-C. Voigt, F. Henkel, S. Fray, T. W. Hänsch, and K. Dieckmann, *Phys. Rev. A* 73, 011402(R) (2006)

First Spectroscopy of the $^1S_0 \rightarrow ^3P_0$ Transition in Lamb-Dicke Confined Magnesium Atoms

A. P. Kulosa, S. Rühmann, K. H. Zipfel, D. B. Fim, T. W. Wübbena, W. Ertmer and E. M. Rasel

Institute of Quantum Optics
Leibniz University of Hanover
Hanover, Germany
Email: kulosa@iqo.uni-hannover.de

Abstract— 10^4 magnesium atoms have been trapped in an optical lattice at the predicted magic wavelength of 469 nm. The trap depth of the lattice sites is $16 E_r$, corresponding to a Lamb-Dicke parameter of $\eta = 0.51$. The temperature of atoms in the lattice is $10 \mu\text{K}$. We performed magnetic field-induced spectroscopy on the strongly spin-forbidden clock transition and observed for the first time a 50 kHz broad carrier signal together with a 80 kHz broad red sideband.

Keywords—Magnesium optical lattice clock; Lamb-Dicke spectroscopy; magic wavelength

I. INTRODUCTION

Magnesium is the 12th element in the periodic table and thus is the lightest species among the candidates for optical atomic clocks. It has three stable isotopes: the bosonic ^{24}Mg and ^{26}Mg , as well as the fermionic ^{25}Mg with a nuclear spin of $I = 5/2$. Most knowledge has been gained so far on ^{24}Mg which has a natural abundance of 78.99 % in an isotope mixture. Magnesium benefits from a low sensitivity to black body radiation [1] and a relatively simple electronic level structure (see fig. 1).

All relevant transitions for laser cooling and clock spectroscopy in magnesium are in the blue or UV range of the electromagnetic spectrum. Laser cooling at 285 nm in the singlet manifold has been well developed [2]. The broad transition linewidth of 78 MHz limits the final temperature in a magneto-optical trap (S-MOT) to approximately 3 mK. The intercombination line with its linewidth of 36 Hz is not suitable for magneto-optical trapping. Nevertheless, we use this transition to optically pump the pre-cooled singlet atoms into the long-lived triplet manifold. Metastable magnesium thus only occurs by laser excitation of the intercombination line as there is no decay channel from the 1P_1 to the triplet manifold via intermediate states like in strontium [3].

Applying a repumping laser to the $^3P_1 \rightarrow ^3D_2$ transition, atoms are optically pumped to the 3P_2 state which is the starting point for our triplet MOT (T-MOT). The $^3P_2 \rightarrow ^3D_3$ cooling transition further cools the atoms to 1 mK. Since the energy splitting of the 3D states is only marginal, a second repumping

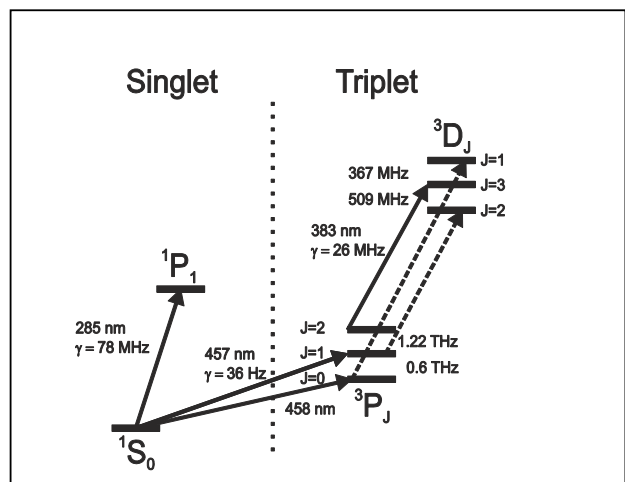


Figure 1. Partial level scheme of ^{24}Mg . The S-MOT is operated on the $^1S_0 \rightarrow ^1P_1$ transition. The intercombination transition $^1S_0 \rightarrow ^3P_1$ is used for transferring the atoms to the triplet manifold. Operating the T-MOT involves three lasers: The cooling laser is acting on the $^3P_2 \rightarrow ^3D_3$ transition, while two additional repumping lasers re-cycle atoms that have decayed to the 3P_0 and 3P_1 states. Clock spectroscopy is performed on the $^1S_0 \rightarrow ^3P_0$ transition.

laser for the 3P_0 state is mandatory to close the MOT cycle. All lasers operate around 383 nm.

Concerning optical trapping of magnesium, it turned out that directly applying laser light at 469 nm (which is the predicted magic wavelength) to the atoms while they are in the 3D_3 state leads to photo ionisation. Hence, we need a far detuned trap for first trapping before we can load the magic wavelength lattice. Recently, we developed a loading scheme for an optical dipole trap (ODT) at 1064 nm for enhancing the transfer efficiency into the dipole trap, which has earlier been limited by the density of the T-MOT [4]. Atoms are continuously pumped from the singlet manifold into the dark 3P_0 state by not applying the relevant repumping laser. The coldest among the 3P_0 atoms are accumulated in the dipole trap thus creating a quasi energy filter for metastable atoms.

In this paper we report about the successful transfer of 3P_0 atoms into an optical lattice at the predicted magic wavelength of 469 nm and the first spectroscopy of the strongly spin-forbidden clock transition $^1S_0 \rightarrow ^3P_0$ at 458 nm. This is a key breakthrough in order to realise a magnesium lattice clock

improving our latest frequency measurement on cold free-falling atoms [5].

II. EXPERIMENTAL SETUP

Atoms are prepared and manipulated in a vacuum chamber made of stainless steel with a background gas pressure below 10^{-9} mBar. The S-MOT is loaded from a Zeeman-slowed thermal beam of magnesium atoms as described in [5]. In contrary to our previous work, the light at 285 nm is nowadays generated by frequency quadrupling a commercial 5 W fibre amplifier laser at 1141 nm. For long-term stability, the frequency doubled laser at 570 nm is locked to an iodine spectroscopy. The main output of the laser feeds a home-built resonant second harmonic generation (SHG) cavity allowing for the generation of up to 350 mW at 285 nm with a linewidth of 6 MHz. An acousto-optic modulator (AOM) splits the UV light into a resonant beam for Zeeman-slowing the thermal atoms and the light further prepared for magneto-optical trapping.

For pumping the atoms from the singlet to the triplet manifold we perform laser excitation on the narrow $^1S_0 \rightarrow ^3P_1$ intercombination line. The transfer laser is a commercial laser system consisting of an amplified diode laser at 914 nm feeding a SHG cavity. The output power at 457 nm is typically 120 mW. In order to address this narrow transition, the laser is frequency-stabilised to a high-finesse cavity with $F = 39000$ providing a laser linewidth of 30 Hz. A detailed description of this laser system can be found in [6].

The T-MOT light at 383 nm is generated by a laser system consisting of three independent lasers for addressing the $^3P_2 \rightarrow ^3D_3$ cooling transition and the two repumping transitions, respectively. Three master oscillator power amplifiers (MOPA) deliver 1 W optical power at 766 nm each feeding independent home-built SHG cavities (see fig. 2). The output power of each SHG is about 100 mW at 383 nm and the lasers have a linewidth of 1 MHz. For frequency stabilisation of the three MOPAs that are far from any magnesium transition and differ several hundreds of GHz in frequency (see fig. 1), we transfer the stability of a reference laser to the MOPA systems via a common transfer cavity [7,8]. Following a suggestion given by Budker et al. [9], we lift the degeneracy of higher order modes inside the cavity by slightly tilting one of the cavity mirrors thus obtaining a mode spacing of 112.5 MHz which is feasible for locking a laser with respect to an atomic transition (the remaining gap can be bridged with AOMs). The length of the cavity is controlled with a piezo-electric transducer (PZT) to which one of the cavity mirrors is attached. Long-term stability is achieved by stabilising the cavity length to an ECDL locked to the ^{39}K D_2 -line at 766 nm via Doppler-free saturation spectroscopy. The MOPAs are stabilised to the transfer cavity using the Pound-Drever-Hall (PDH) method [10]. Frequency modulation sidebands are generated by laser diode current modulation around 20 MHz. Each SHG cavity is then locked to its respective MOPA light using exactly the same modulation sidebands which largely reduces the complexity in electronic stabilisation efforts. A Ti:Sa laser giving 0.9 W of optical power with a maximum

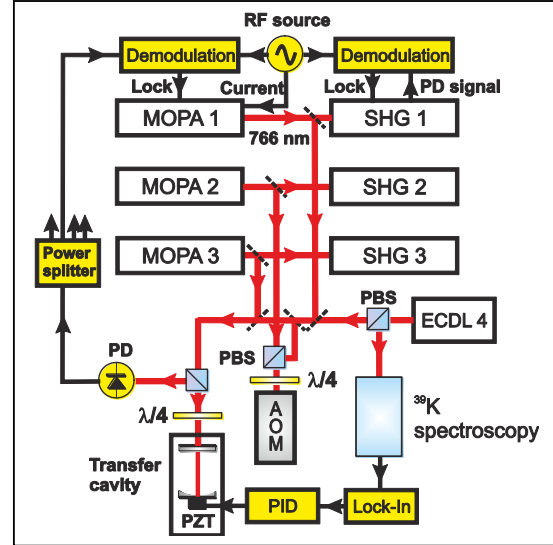


Figure 2. Schematic setup of the laser system used for operation of the T-MOT. The three independent lasers are locked to a common transfer cavity using the PDH scheme. The length of the transfer cavity is stabilised by means of a fourth laser referenced to the D_2 -line of ^{39}K via Doppler-free spectroscopy. The locking scheme is shown in detail only for MOPA 1 for clarity. (PZT: piezo-electric transducer, PBS: polarising beam splitter, PD: photo diode)

tuning range of 930 – 960 nm feeds a commercial SHG cavity providing the light for the optical lattice. Long-term frequency stability of the Ti:Sa laser is obtained by stabilising it to the ultra-stable clock laser at 916 nm by means of another transfer cavity. According to the theoretical prediction of the magic wavelength for magnesium, the SHG output delivers 130 mW fibre-guided light at 469 nm to the experiment for generating the optical lattice. In order to fulfil the power requirements on Lamb-Dicke confinement, this light is enhanced in a linear build-up cavity which is set up in the horizontal plane around the vacuum chamber. Fig. 3 shows the schematic setup of the resonator. The cavity has a total length of 850 mm with a beam waist of 65 μm and consists of a curved mirror ($R = 500$ mm, $T = 3\%$ around 469 nm), a plane mirror being HR-coated for the magic wavelength but AR-coated for the clock laser at 458 nm and a second curved mirror ($R = 350$ mm) having the same coating as the plane one. We operate with this three-mirror folded design due to two constraints on the cavity: (i) the clock laser has to be spatially overlapped with the lattice light for interrogation without being enhanced inside the cavity and (ii) the transmission of the incoupling mirror has to match the light losses per round trip inside the cavity (impedance matching) to ensure the highest possible enhancement factor. Offering a high transmission for 458 nm at the same time represents a hard-to-fulfil requirement on the mirror coating. Finally, the dipole trap beam at 1064 nm emitted by a Ytterbium fibre laser is overlapped with the lattice light in order to transfer the atoms into the optical lattice.

The maximum build-up factor of the cavity is 15, so we obtain a circulating power of 1.5 W by coupling 100 mW of light into the cavity. The corresponding trap depth is $16 E_r$ with E_r being

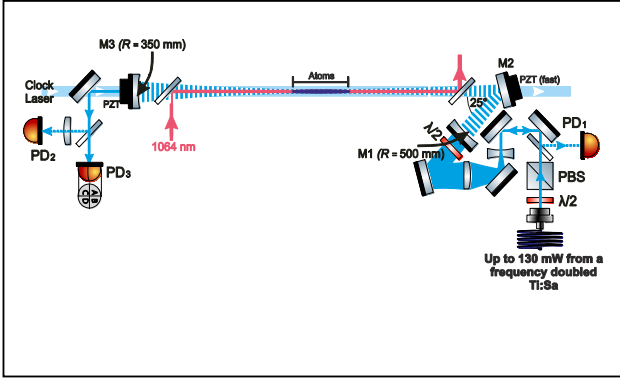


Figure 3. Schematic setup of the enhancement cavity for generation of the optical lattice. The total length of the cavity is 850 mm which is stabilized using the back-reflected light at mirror M1 (photo diode PD1). Using PD2 measuring the light leaking out of the cavity, the intra-cavity power is stabilised while a 4-quadrant photo diode (PD3) stabilises the cavity mode.

the recoil energy (in temperature units E_r is 1.8 μ K). We measured the trap frequencies to be $2\pi \times 150$ kHz which results in a Lamb-Dicke parameter of $\eta = 0.51$. The enhancement and thus the trap depth may be further increased by exchanging the view ports of the vacuum chamber as there might be a coating damage. A photo diode in front of the cavity is used for cavity length stabilisation (PD1) using the PDH scheme. PD2 is used for stabilising the circulating power inside the cavity while a 4-quadrant photo diode controls the cavity mode by giving feedback to two PZTs acting on Mirror 3 (see fig. 3).

The clock laser at 916 nm is guided via a 30 m long phase-stabilised fibre from a separate room to the magnesiumium experiment showing a frequency instability of 5×10^{-16} in 1 s averaging time. The light is amplified in the magnesiumium laboratory and frequency doubled to 458 nm in a commercial SHG cavity with an output power of 100 mW. The clock laser light is further fibre-guided to the experimental chamber and is aligned paraxial with the optical lattice.

III. PREPARATION OF ATOMS

The procedure of preparing metastable 3P_0 atoms in an ODT at 1064 nm is described in detail in [4]. For clarity, the continuous loading scheme we are using is different from stepwise loading of the S-MOT and the T-MOT with subsequent capture in the dipole trap. Instead, during the dipole trap loading, the S-MOT laser, transfer laser, T-MOT lasers and dipole laser are operating continuously, except the repumping laser for the 3P_0 state. Since the ODT has a maximum depth of 260 μ K, we filter out the coldest 3P_0 atoms being captured by the potential. We trap about 10^5 atoms at a temperature of 100 μ K.

In order to trap atoms in the optical lattice, the lattice light is applied additionally to the ODT, while the dipole trap and all other lasers are turned off after a period of 100 ms. Transfer of atoms to the lattice is performed with an efficiency of 10 %. The temperature of atoms in the lattice has been measured to be 10 μ K.

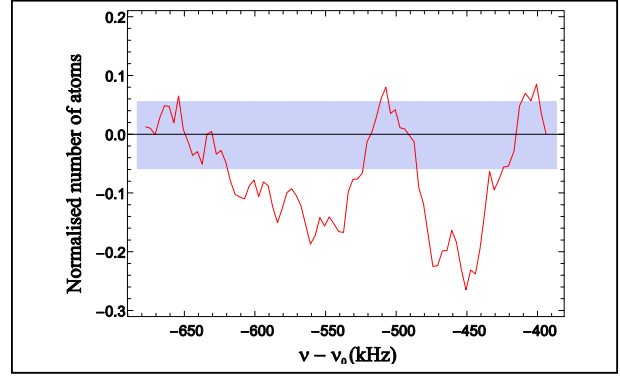


Figure 4. First spectroscopy of the clock transition. The red line is a moving average of five consecutive data points while the blue area indicates the signal standard deviation in absence of the spectroscopy laser. The carrier is observed at a detuning of -460 kHz and the red sideband at a detuning of -550 kHz.

IV. SPECTROSCOPY OF THE $^1S_0 \rightarrow ^3P_0$ TRANSITION

In order to enhance the mHz natural linewidth of the clock transition for spectroscopy, we follow the suggestion of Taichenachev et al. [11] and apply a homogeneous magnetic field during the interrogation pulse thus creating a mixture of the magnetic 3P_1 state and the non-magnetic 3P_0 state. In order to address the transition for the first time, we apply a strong field ($B = 500$ G) causing \sim kHz power broadening of the line. Later on, we will require only a weak magnetic field if the transition frequency is well known.

After 1 s of preparation of atoms in the dipole trap, they are transferred to the optical lattice. In parallel, the static magnetic field is created by switching the Anti-Helmholtz MOT coils to Helmholtz configuration. During the 100 ms spectroscopy pulse, atoms in the 3P_0 state eventually are de-excited to the 1S_0 state depending on the clock laser frequency, so losses in number of atoms would indicate a spectroscopy resonance. For detection the quadrupole field is restored, atoms are released from the lattice and subsequently captured by the T-MOT for fluorescence detection. Detection in the triplet manifold is carried out with a high signal-to-noise ratio since no atoms from the background gas contribute to the signal.

Fig. 4 shows such a recorded spectroscopy sequence. The clock laser frequency was changed in steps of 300 Hz. Each data point is the result of three differential measurements (with and without the clock laser) being averaged. Furthermore, we took a moving average over five such consecutive data points to reduce the signal noise. One can clearly see a carrier signal together with a red sideband. Knowing the frequency of the $^1S_0 \rightarrow ^3P_0$ clock transition without performing an absolute frequency measurement to be $\nu_0 = 655\,058\,646\,681\,860(47)$ Hz due to earlier frequency measurements of the $^1S_0 \rightarrow ^3P_1$ transition [5] and the $^3P_1 \rightarrow ^3P_0$ transition [12] we observe the carrier with 25 % of atoms being de-excited at a detuning of -460 kHz from the expected signal having a FWHM of 40 kHz. Due to the magnetic field of 500 G, a 2nd order Zeeman shift of -534 kHz is expected for the clock transition which is

in moderate agreement with the measurement. The red sideband could be observed at a frequency detuning of -550 kHz with a FWHM of 80 kHz. The broad carrier linewidth may be due to additional homogeneous broadening effects like fluctuations in the magnetic field. The width of the red sideband is subject to inhomogeneous broadening since the width of the second lattice energy band is 50 kHz. However, we do not observe a blue sideband giving rise to the assumption, that atoms occupy mostly the lowest energy band in the 3P_0 lattice potential.

V. SUMMARY & OUTLOOK

We have presented the successful loading of 10^4 metastable atoms in an optical lattice at the predicted magic wavelength of 469 nm. The atoms have a temperature of 10 μ K. Performing magnetic-field-induced spectroscopy, we are able to observe the strongly spin-forbidden $^1S_0 \rightarrow ^3P_0$ clock transition.

In order to increase the signal-to-noise ratio of the spectroscopy signal, we will, as a next step, optically pump the prepared atoms in the 3P_0 state back to the 1S_0 state, while being held by the dipole trap. Transfer to the optical lattice will thus happen in the singlet manifold and remaining metastable atoms will be blown away with resonant beams. Performing clock spectroscopy starting in the 1S_0 state with detection using the T-MOT afterwards promises a significant higher signal-to-noise ratio as no background atoms will contribute to the detection signal.

VI. ACKNOWLEDGMENT

This work was supported by the Sonderforschungsbereich 407 and the Cluster of Excellence "QUEST" (Centre for Quantum-Engineering and Space-Time Research).

REFERENCES

- [1] S. G. Porsev and A. Dereviako, "Multipolar theory of blackbody radiation shift of atomic energy levels and its implications for optical lattice clocks", *Phys. Rev. A*, vol. 74, 020502(R), 2006
- [2] T. E. Mehlstäubler, *et al.*, "Observation of sub-Doppler temperatures in bosonic magnesium", *Phys. Rev. A*, vol. 77, 021402(R), 2008
- [3] N. Poli, *et al.*, "Cooling and trapping of ultracold strontium isotopic mixtures", *Phys. Rev. A*, vol. 71, 061403(R), 2005
- [4] M. Riedmann, *et al.*, "Beating the density limit by continuously loading a dipole trap from millikelvin-hot magnesium atoms", *Phys. Rev. A*, 043416, 2012
- [5] J. Friebe, *et al.*, "Remote frequency measurement of the $^1S_0 \rightarrow ^3P_1$ transition in laser-cooled ^{24}Mg ", *New J. Phys.*, vol. 13, 125010, 2011
- [6] J. Friebe, *et al.*, "Absolute frequency measurement of the magnesium intercombination transition $^1S_0 \rightarrow ^3P_1$ ", *Phys. Rev. A*, vol. 78, 033830, 2008
- [7] P. Bohlouli-Zanjani, K. Afrousheh and J. D. D. Martin, "Optical transfer cavity stabilization using current-modulated injection-locked diode lasers", *Rev. Sci. Instrum.*, vol 77, 093105, 2006
- [8] C. E. Liekhuis-Schmaltz, R. Mantifel, M. Torabifard, I. B. Burgess and J. D. D. Martin, "Injection-locked diode laser current modulation for Pound-Drever-Hall frequency stabilization using transfer cavities", *JOSA B*, vol. 29, issue 6, pp. 1394-1398, 2012
- [9] D. Budker, S. M. Rochester and V. V. Yashchuk, "Obtaining frequency markers of variable separation with a spherical mirror Fabry-Perot interferometer", *Rev. Sci. Instrum.*, vol 71, 2984, 2000
- [10] R. W. P. Drever, *et al.*, "Laser phase and frequency stabilization using an optical resonator", *Appl. Phys. B*, vol. 31, issue 2, pp. 97-105, 1983
- [11] A. V. Taichenachev, *et al.*, "Magnetic field-induced spectroscopy of forbidden optical transitions with application to lattice-based optical atomic clocks", *Phys. Rev. Lett.* vol 96, 083001, 2006
- [12] A. Godone and C. Novero, "The magnesium frequency standard", *Metrologia*, vol. 30, issue 3, 163, 1993

Towards a Mg Lattice Clock: Observation of the 1S_0 - 3P_0 Transition and Determination of the Magic Wavelength

A. P. Kulosa,¹ D. Fim,¹ K. H. Zipfel,¹ S. Rühmann,¹ S. Sauer,¹ N. Jha,¹ K. Gibble,^{1,2} W. Ertmer,¹ E. M. Rasel,¹ M. S. Safronova,^{3,4} U. I. Safronova,⁵ and S. G. Porsev^{3,6}

¹*Institut für Quantenoptik, Leibniz Universität Hannover, Welfengarten 1, 30167 Hannover, Germany*

²*Department of Physics, The Pennsylvania State University, University Park, Pennsylvania 16802, USA*

³*Department of Physics and Astronomy, University of Delaware, Newark, Delaware 19716, USA*

⁴*Joint Quantum Institute, NIST and the University of Maryland, College Park, Maryland 20899, USA*

⁵*Department of Physics, University of Nevada, Reno, Nevada 89557, USA*

⁶*Petersburg Nuclear Physics Institute, Gatchina 188300, Russia*

(Received 5 August 2015; published 9 December 2015)

We optically excite the electronic state $3s3p\ ^3P_0$ in ^{24}Mg atoms, laser cooled and trapped in a magic-wavelength lattice. An applied magnetic field enhances the coupling of the light to the otherwise strictly forbidden transition. We determine the magic wavelength, the quadratic magnetic Zeeman shift, and the transition frequency to be 468.46(21) nm, $-206.6(2.0)$ MHz/T², and 655 058 646 691(101) kHz, respectively. These are compared with theoretical predictions and results from complementary experiments. We also develop a high-precision relativistic structure model for magnesium, give an improved theoretical value for the blackbody radiation shift, and discuss a clock based on bosonic magnesium.

DOI: 10.1103/PhysRevLett.115.240801

PACS numbers: 06.30.Ft, 31.15.ac, 37.10.Jk, 42.62.Fi

The frequencies of optical clocks are currently measured with a fractional accuracy and precision of nearly 10^{-18} [1–4]. A potentially limiting systematic frequency shift of both ion and optical lattice clocks is the ac Stark shift from room-temperature blackbody radiation (BBR) [5,6]. Clock transitions with small BBR sensitivities are an attractive approach to even higher accuracies. Among these are neutral Hg and Mg, In⁺, and especially the Al⁺ ion clock transition, which all have significantly smaller BBR sensitivities than Sr and Yb lattice clocks and Cs microwave clocks.

In this Letter, we report the spectroscopy of the Mg clock transition in a magic-wavelength optical lattice, which gives equal ac Stark shifts of the clock states. We measure the transition frequency [7,8] and its magic wavelength and quadratic Zeeman shift, which were recently predicted [9–12].

Along with our measurements, we developed a more refined atomic structure model to calculate both the magic wavelength as well as the static BBR shift. For less massive atoms, such as Mg, these models are more accurate than for heavier elements like Sr and Yb, and spectroscopy of low-mass elements generally represents an interesting test bed for validating improved theoretical models [13]. Both our theoretical and experimental results for the magic wavelength agree at a level of better than 1% and restrict the value, which was estimated to fall between 466 and 480 nm [9–11]. Our model for Mg predicts a static BBR shift to be 8 and 5 times lower than those measured for Sr and Yb, respectively [14,15]. Apart from the static contribution, the total BBR shift also includes a

dynamic contribution, which is derived from the combination of theoretical calculations and measurements of the 3D_1 state lifetime [5,16]. Reference [17] estimated the dynamic contribution in Mg to be 0.1% for the 3P_0 state, remarkably smaller than those of Yb (1%) and Sr (4%).

For bosonic atoms, optical dipole excitation of the electronic ground state 1S_0 to 3P_0 is strongly suppressed. A magnetic field enhances the dipole coupling, enabling a nanohertz linewidth by mixing the 3P_1 electronic state [12,18]. References [12,19] calculated the associated second-order Zeeman effect for Mg to be $-217(11)$ MHz/T² [equivalent to a fractional frequency shift of $-3.31(17) \times 10^{-7}/\text{T}^2$], a systematic effect that must be evaluated. We precisely measure the magnetic field dependence, which is consistent within the uncertainty of Ref. [12], estimated to be 5% [19]. This second-order Zeeman shift is larger than those of Yb [$-6.6(4)$ MHz/T² or $-1.27(8) \times 10^{-8}/\text{T}^2$ [18]] and Sr [$-23.5(2)$ MHz/T² or $-5.47(47) \times 10^{-8}/\text{T}^2$ [20]].

In this way, we directly measure the transition frequency, which agrees with the difference of the measured frequencies of the 1S_0 - 3P_1 and 3P_0 - 3P_1 transitions [7,8]. Because of its low mass and the short magic wavelength, Mg has a large photon recoil frequency shift $\Delta\nu_R = h/2\lambda_{\text{magic}}^2 m_{\text{Mg}}$, where λ_{magic} is the magic wavelength, as well as greater tunneling. A deeper lattice is therefore required to suppress tunneling [21], as compared to heavier species.

We briefly summarize the steps required for the optical lattice spectroscopy in Fig. 1. A thermal beam of Mg atoms is slowed and loaded into a “singlet”-magneto-optical trap (MOT) using laser light tuned near the 1S_0 - 1P_1

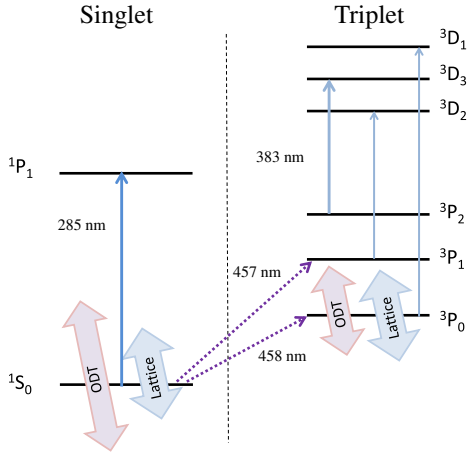


FIG. 1 (color online). Optical transitions in ^{24}Mg relevant for optical lattice spectroscopy. Atoms are continuously loaded into the long-lived electronic state 3P_0 in an optical dipole trap (ODT) at 1064 nm using a dual MOT [23]. Atoms trapped in a MOT using the 1S_0 - 1P_1 transition are optically transferred with 457 nm light to the 3P_1 state and then to 3P_2 . The atoms are further cooled in a MOT with 383 nm light that excites the 3D manifold, and cold atoms are permitted to accumulate in 3P_0 in the ODT. These atoms are optically depumped to the ground state via 3P_1 , and the magic-wavelength optical lattice is adiabatically turned on. The dipole trap and the optical lattice laser beams are depicted by the bold arrows. The 458 nm light interrogates the magnetic-field-enhanced clock transition.

transition. Atoms are optically transferred, after excitation to the 3P_1 state, into a second, simultaneously operated “triplet” 3P_2 - 3D_3 MOT. There, atoms can decay to the 3P_1 state (see Fig. 1) during MOT operation [22] and have to be recycled with light exciting them to the 3D_2 state. This continuous loading scheme yields nearly 10^5 atoms in the 3P_0 state within 1 s at $100 \mu\text{K}$ in a 1064 nm dipole trap as in Ref. [23]. The atoms are then optically pumped to the 3D_2 state for 360 ms and decay to the electronic ground state via the 3P_1 state. Afterwards, a spatially overlapped 1D optical lattice with a waist of $89 \mu\text{m}$ is adiabatically turned on in 100 ms before the dipole trap is rapidly switched off. To select the coldest atoms, the optical lattice intensity is ramped to a lower depth and subsequently increased to a final value for the clock transition spectroscopy. Each of these linear intensity variations is performed within 100 ms. This procedure reproducibly generates about 1000 atoms at $4 \mu\text{K}$.

We generate 160 mW of lattice light near the magic wavelength at $\lambda_{\text{magic}} = 469 \text{ nm}$ with a frequency-doubled Ti:sapphire laser. A horizontal buildup cavity, with a finesse of 80, twines around the vacuum chamber and, with a circulating power of $\sim 2.3 \text{ W}$, produces trap depths of ten recoil energies $h\nu_R$. The cavity length is stabilized to the frequency of the laser with a Pound-Drever-Hall [24] lock driving an electro-optical modulator and a piezo-controlled mirror. An additional feedback loop driving an

acousto-optical modulator (AOM) can set and stabilize the depth of the lattice. The light transmitted through the cavity is used to measure the circulating light intensity in the cavity.

The clock transition spectroscopy is performed with a homebuilt external cavity diode laser stabilized to an ultrastable resonator with finesse $\mathcal{F} = 600000$ at 916 nm, similar to Ref. [25]. The infrared light is fiber guided to the spectroscopy setup, a tapered amplifier chip, and a commercial second-harmonic generation stage. The system generates 10 mW of 458 nm light with a short-term frequency instability as low as 5×10^{-16} in 1 s, inferred with the help of a second ultrastable resonator. The spectroscopy is performed by irradiating the atoms for 100 ms with a pulsed, Gaussian-shaped laser beam with a waist of $300 \mu\text{m}$ and a peak intensity of 7 W/cm^2 . The MOT coils, operated in a Helmholtz configuration, generate a magnetic field of $2.49(1) \text{ G/A}$, determined via optical Zeeman spectroscopy of the $^1S_0(m_J = 0)$ - $^3P_1(m_J = \pm 1)$ transitions, increasing the dipole coupling of 1S_0 and 3P_0 . We normally use a magnetic field of 249 G, which yields a predicted linewidth of $8.07 \mu\text{Hz}$ and a Rabi frequency of 205 Hz [12]. In this way, we resonantly excite up to 1000 atoms to 3P_0 , which are then optically pumped to 3P_2 and detected with 80 ms of fluorescence from the triplet MOT. This detection scheme yields a sensitivity of a few tens of atoms. To obtain the line center and profile of the transition, we record the number of excited atoms as we step the frequency of the 458 nm laser. The initial drift of the laser is determined via spectroscopy of the atoms and compensated with a feedforward of an AOM that shifts the laser frequency to a resonance of our ultrastable cavity. A scan over the resonance typically comprises 30 measurements, each lasting 1.9 s.

The magic wavelength for ^{24}Mg is inferred from measurements of the line center for different lattice depths and several wavelengths. Figure 2(a) shows two sets of measurements of the transition probability (red and blue dots) versus the clock laser frequency and corresponding Gaussian fits (red and blue solid curves) for three depths of a 466.97 nm lattice. The line profiles for different trap depths were measured successively. To evaluate and correct the residual laser drift, the measurement sequence was repeated three times, and the shift of the line centers for a specific trap depth is determined from the Gaussian fits. From the frequencies for a specific lattice depth, we infer the residual clock laser drift, which can be as large as 2–3 kHz within several minutes. The line profiles in Fig. 2(a) are three superposed scans. The linewidth of each profile, on the order of a few kilohertz, is mostly due to tunneling in our shallow optical lattice. According to Ref. [21], the total line broadening is on the order of twice the ground state bandwidth, in agreement with our findings. In our current apparatus, the trap depth was as low as six recoil energies, which gives rise to a carrier width of

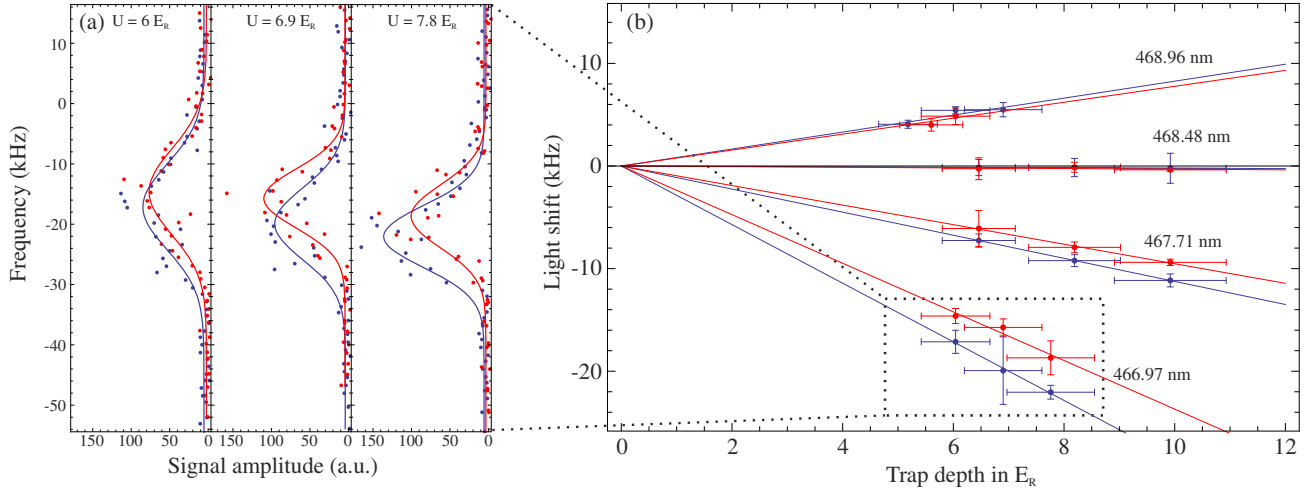


FIG. 2 (color online). (a) Measured and fit line profiles for three depths of a 466.97 nm optical lattice. Two sets of measurements (red and blue dots) are shown with their corresponding Gaussian fits (red and blue solid lines). (b) The observed linear ac Stark shift versus the optical lattice depth for several lattice wavelengths. The frequencies of the line center (dots) from Gaussian fits as in (a) and their corresponding linear regression (solid lines) are depicted. For each measurement set at a lattice wavelength, a single frequency offset accounts for the drift of our ultrastable cavity.

approximately 16 kHz. Figure 2(b) shows the line centers (dots) and the corresponding linear regression (solid lines) of the ac Stark shifts versus the lattice depth for different lattice wavelengths. An offset frequency was subtracted from the linear regressions for each lattice wavelength to account for the laser drift between measurements. The uncertainty of the experimental determination of the lattice depth is about 5% dominated by the uncertainty of the lattice waist. The uncertainty of the ac Stark shift is a combination of the statistical uncertainty of the linear regression and the systematic uncertainty of residual (non-linear) frequency drifts of the clock laser, on the order of a few kilohertz. During the measurements for 466.97 nm, the clock laser was less stable, leading to more noise in the number of detected atoms, larger error bars, and a larger variation of the observed ac Stark shifts. The differences in the linear regression from the two measurement campaigns agree within these uncertainties. Separately, the two data sets yield magic wavelengths of 468.47(22) (blue data) and 468.45(19) nm (red data). Applying a linear regression to the combination of both measurement sets, we determine the magic wavelength of the $^{24}\text{Mg } ^1S_0\text{-}^3P_0$ transition to be 468.46(21) nm and the linear ac Stark shift dependence on the lattice depth and wavelength to be $1.67(12) \text{ kHz}/E_R/\text{nm}$ [equivalent to a fractional frequency shift of $2.55(18) \times 10^{-12}/E_R/\text{nm}$].

The experimentally determined magic wavelength agrees well with our theoretical prediction. We use a state-of-the-art relativistic approach that combines configuration interaction and all-order linearized coupled-cluster methods (CI + all-order). To evaluate the uncertainty of our calculations, we use a combination of the CI and

second-order many-body perturbation theory (CI + MBPT), which does not include all-order corrections to the effective Hamiltonian. The difference of the CI + MBPT and CI + all-order values serves as an estimate of the theoretical accuracy [26–28]. The results are summarized in Table I. Our final recommended value for the theoretical Mg magic wavelength, listed in the “Final” row, uses measured instead of calculated transition energies for the dominant contributions. While our calculated Mg transition

TABLE I. Comparison of CI + MBPT and CI + all-order values for magic wavelengths λ_{magic} in nanometers and static polarizabilities α (in atomic units) of Mg, Sr [28], and Yb [27]. $\Delta\alpha = \alpha(nsnp^3P_0) - \alpha(ns^2^1S_0)$. The “Final” value in the third line uses measured instead of calculated energies of the most important polarizability contributions in the CI + all-order calculation.

Quantity	Method	Mg	Sr	Yb
λ_{magic}	CI + MBPT	468.45	847	789
	CI+all	468.68	820	754
	Final	468.45(23)		
	Exp.	468.46(21)	813.427 ^a	759.354 ^a
$\alpha(^1S_0)$	CI + MBPT	71.257	195.4	138.3
	CI + all	71.251	197.8	140.9
$\alpha(^3P_0)$	CI + MBPT	100.812	482.1	305.9
	CI + all	100.922	458.1	293.2
$\Delta\alpha$	CI + all	29.671	260.3 ^b	152.3
	Exp.		247.379(7)	145.726(3)

^aWe only list six significant figures from the measurements in Refs. [29,30].

^bUsing experimental energies gives 254.4 a.u., and small corrections yield 247.5 a.u.

energies agree with the observed values to a few cm^{-1} , even these small differences affect the magic wavelength in the fourth significant figure. We note that this correction is quite small and the final value differs from the *ab initio* CI + all-order value by only 0.05%.

In Table I, we give CI + MBPT and CI + all-order values for the magic wavelength λ_{magic} . We also give the static ground state $\alpha(ns^2\ ^1S_0)$ and excited clock state $\alpha(nsn\ ^3P_0)$ polarizabilities and their difference $\Delta\alpha$, which is proportional to the static BBR shift [17]. To demonstrate the extremely high accuracy of the theoretical calculations in Mg, we compare the magic wavelength and polarizabilities of Mg, Sr, and Yb in Table I. In our theoretical method, the main difference between Mg, Sr, and Yb are the much larger and more complicated cores of Sr and Yb than of Mg. As a result, core-valence correlations are much smaller in Mg than in Sr and Yb, leading to substantially higher accuracy for the theoretical predictions for Mg. The large differences between CI + MBPT and CI + all-order Sr and Yb values illustrate the significance of higher-order effects in these heavier systems. We note that the difference of the CI + MBPT and CI + all-order values for Sr and Yb is much larger than the difference of the CI + all-order results with experiment for both the magic wavelength and $\Delta\alpha$, confirming the validity of using such a difference as an uncertainty estimate of the Mg theoretical values. The excellent agreement of the CI + MBPT and CI + all-order polarizabilities indicates an uncertainty of the Mg BBR shift of less than 1%.

The second-order Zeeman shift drops out of the determination of the magic wavelength but is a significant correction to our measured transition frequency. Figure 3 shows the measured transition frequency versus the applied magnetic field (squares), a parabolic fit (black curve) of the

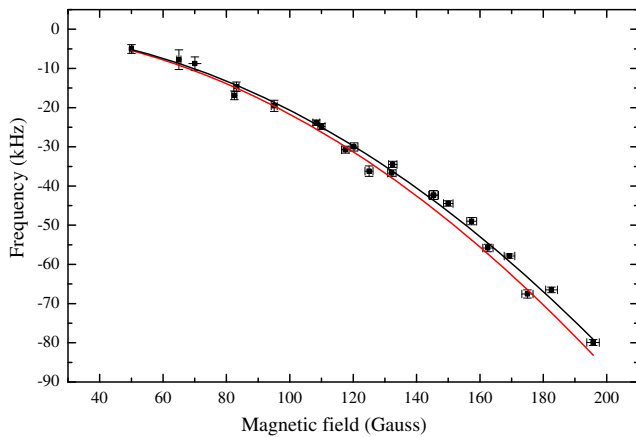


FIG. 3 (color online). Quadratic Zeeman shift of the clock transition versus magnetic field strength (black squares), a parabolic fit (black curve), and the theoretical prediction of Ref. [12] (red curve). The predicted dependence on the magnetic field is $-217(11) \text{ MHz/T}^2$, which agrees with the experimental result of $-206.6(2.0) \text{ MHz/T}^2$.

measurements, and a theoretical prediction by Ref. [12] (red curve). The experimental parabolic coefficient is $-206.6(2.0) \text{ MHz/T}^2$ [equivalent to $-3.15(3) \times 10^{-7}/\text{T}^2$] and agrees within 5% with a theoretical value, which is consistent with its estimated uncertainty [19]. The measurement accuracy of the magnetic field strength, via the Zeeman spectroscopy of the $^1S_0\text{-}^3P_0$ transition, is 1% and limited by our present accuracy in measuring the MOT coils' electrical current.

Our measurements at the magic wavelength, with the correction of the second-order Zeeman shift, yield a direct measurement of the optical transition frequency of 655 058 646 691(101) kHz. The absolute frequency is measured by beating the spectroscopy laser with an optical frequency comb that is stabilized to a 10 MHz GPS frequency reference. The measured transition frequency agrees with the difference of previous spectroscopic measurements of the $^1S_0\text{-}^3P_1$ and $^3P_0\text{-}^3P_1$ transitions of 655 659 923 839 730(48) and 601 277 157 870.0(0.1) Hz to better than 100 kHz, which corresponds to the estimated uncertainty of this measurement [7,8].

In summary, we report the direct optical spectroscopy of the $^1S_0\text{-}^3P_0$ clock transition of laser-cooled bosonic ^{24}Mg in a magic-wavelength optical lattice. Our measurements determine precisely the magic wavelength and confirm the high precision obtained with a new theoretical atomic model of Mg. Our experimental determination of the quadratic Zeeman effect and clock transition frequency agree with a prediction [12] and previous indirect frequency measurements. Lattices with a larger depth of more than 40 recoil energies, accessible with higher laser power and a higher finesse of the enhancement cavity, will display a reduced width of the lowest vibrational band to 20 Hz and thus allow more precise spectroscopic measurements.

The demonstrated agreement of our combination of theory and experimental measurements is an important ingredient for exploring a future bosonic and fermionic Mg optical lattice clock. For bosonic magnesium, atoms can be optically prepared at microkelvin temperatures, which has not yet been demonstrated for the fermionic isotope ^{25}Mg . In our experiment, a dilute atomic cloud of 1000 atoms is distributed over 130 000 lattice sites (~ 0.008 atoms per lattice site), which is a factor of 100 lower density than that reported for other clocks with approximately the same number of atoms [31,32], significantly reducing the limitations from collisional shifts. The quadratic Zeeman shift can be sufficiently controlled [33] by using the suitably narrow Mg transitions for Zeeman spectroscopy, a higher clock laser intensity, and a smaller magnetic field [12]. A clock laser intensity of 7 W/cm^2 yields a Rabi frequency of 20 Hz, with a magnetic field that is 10 times smaller and a corresponding reduction in the uncertainty of the quadratic Zeeman shift. Here, in the context of Sr, Yb, and Hg, Mg can use higher clock laser intensities, because the clock and magic wavelengths are nearly equal, leading to small

differential polarizabilities of the Mg clock states and a naturally smaller clock-laser ac Stark shift. Combining all of these techniques can exploit the small Mg sensitivity to blackbody radiation to make a highly accurate and stable lattice clock and further precisely test atomic models for precision spectroscopy.

We thank A. Bauch and H. Schnatz from Physikalisch Technische Bundesanstalt (PTB) for providing a passive H maser and assistance with frequency measurements during the early stage of the experiment as well as C. Lisdat for helpful discussions. This work was supported in part by Deutsche Forschungsgemeinschaft (DFG) within QUEST, Center for Quantum Engineering and Space-Time Research (A. P. K., S. R., S. S., W. E., and E. M. R.), NASA (K. G.), and U.S. NSF Grants No. PHY-1404156 (M. S. S. and S. G. P.) and No. PHY-1311570 (K. G.). D. F. and K. H. Z. acknowledge financial support from DFG Research Training Group (Graduiertenkolleg) 1729. N. J. is supported by the Marie Curie Initial Training Network FACT (ITN-FACT) Program, call FP7-PEOPLE-2013-ITN.

-
- [1] C. W. Chou, D. B. Hume, J. C. J. Koelemeij, D. J. Wineland, and T. Rosenband, *Phys. Rev. Lett.* **104**, 070802 (2010).
- [2] N. Hinkley, J. A. Sherman, N. B. Phillips, M. Schioppo, N. D. Lemke, K. Beloy, M. Pizzocaro, C. W. Oates, and A. D. Ludlow, *Science* **341**, 1215 (2013).
- [3] B. J. Bloom, T. L. Nicholson, J. R. Williams, S. L. Campbell, M. Bishop, X. Zhang, W. Zhang, S. L. Bromley, and J. Ye, *Nature (London)* **506**, 71 (2014).
- [4] I. Ushijima, M. Takamoto, M. Das, T. Ohkubo, and H. Katori, *Nat. Photonics* **9**, 185 (2015).
- [5] T. Nicholson, S. Campbell, R. Hutson, G. Marti, B. Bloom, R. McNally, W. Zhang, M. Barrett, M. Safronova, G. Strouse, W. Tew, and J. Ye, *Nat. Commun.* **6**, 6896 (2015).
- [6] K. Beloy, N. Hinkley, N. B. Phillips, J. A. Sherman, M. Schioppo, J. Lehman, A. Feldman, L. M. Hanssen, C. W. Oates, and A. D. Ludlow, *Phys. Rev. Lett.* **113**, 260801 (2014).
- [7] A. Godone and C. Novero, *Metrologia* **30**, 163 (1993).
- [8] J. Friebe, M. Riedmann, T. Wübbena, A. Pape, H. Kelkar, W. Ertmer, U. Sterr, S. Weyers, G. Grosche, H. Schnatz, and E. M. Rasel, *New J. Phys.* **13**, 125010 (2011).
- [9] R. Santra, K. V. Christ, and C. H. Greene, *Phys. Rev. A* **69**, 042510 (2004).
- [10] V. D. Ovsyannikov, V. G. Pal'chikov, H. Katori, and M. Takamoto, *Quantum Electron.* **36**, 3 (2006).
- [11] A. Derevianko, B. Obreshkov, and V. A. Dzuba, *Phys. Rev. Lett.* **103**, 133201 (2009).
- [12] A. V. Taichenachev, V. I. Yudin, C. W. Oates, C. W. Hoyt, Z. W. Barber, and L. Hollberg, *Phys. Rev. Lett.* **96**, 083001 (2006).
- [13] J. Mitroy, M. S. Safronova, and C. W. Clark, *J. Phys. B* **43**, 202001 (2010).
- [14] T. Middelmann, S. Falke, C. Lisdat, and U. Sterr, *Phys. Rev. Lett.* **109**, 263004 (2012).
- [15] J. A. Sherman, N. D. Lemke, N. Hinkley, M. Pizzocaro, R. W. Fox, A. D. Ludlow, and C. W. Oates, *Phys. Rev. Lett.* **108**, 153002 (2012).
- [16] K. Beloy, J. A. Sherman, N. D. Lemke, N. Hinkley, C. W. Oates, and A. D. Ludlow, *Phys. Rev. A* **86**, 051404 (2012).
- [17] S. G. Porsev and A. Derevianko, *Phys. Rev. A* **74**, 020502 (R) (2006); **86**, 029904(E) (2012).
- [18] Z. W. Barber, C. W. Hoyt, C. W. Oates, L. Hollberg, A. V. Taichenachev, and V. I. Yudin, *Phys. Rev. Lett.* **96**, 083002 (2006).
- [19] A. V. Taichenachev (private communication).
- [20] P. G. Westergaard, J. Lodewyck, L. Lorini, A. Lecallier, E. A. Burt, M. Zawada, J. Millo, and P. Lemonde, *Phys. Rev. Lett.* **106**, 210801 (2011).
- [21] P. Lemonde and P. Wolf, *Phys. Rev. A* **72**, 033409 (2005).
- [22] P. L. Hansen, K. T. Therkildsen, N. Malossi, B. B. Jensen, E. D. van Ooijen, A. Bruschi, J. H. Müller, J. Hald, and J. W. Thomsen, *Phys. Rev. A* **77**, 062502 (2008).
- [23] M. Riedmann, H. Kelkar, T. Wübbena, A. Pape, A. Kulosa, K. Zipfel, D. Fim, S. Rühmann, J. Friebe, W. Ertmer, and E. Rasel, *Phys. Rev. A* **86**, 043416 (2012).
- [24] R. W. P. Drever, J. L. Hall, F. V. Kowalski, J. Hough, G. M. Ford, A. J. Munley, and H. Ward, *Appl. Phys. B* **31**, 97 (1983).
- [25] A. Pape, O. Terra, J. Friebe, M. Riedmann, T. Wübbena, E. M. Rasel, K. Predehl, T. Legero, B. Lipphardt, H. Schnatz, and G. Grosche, *Opt. Express* **18**, 21477 (2010).
- [26] M. S. Safronova, M. G. Kozlov, and C. W. Clark, *Phys. Rev. Lett.* **107**, 143006 (2011).
- [27] M. S. Safronova, S. G. Porsev, and C. W. Clark, *Phys. Rev. Lett.* **109**, 230802 (2012).
- [28] M. S. Safronova, S. G. Porsev, U. I. Safronova, M. G. Kozlov, and C. W. Clark, *Phys. Rev. A* **87**, 012509 (2013).
- [29] A. D. Ludlow *et al.*, *Science* **319**, 1805 (2008).
- [30] Z. W. Barber, J. E. Stalnaker, N. D. Lemke, N. Poli, C. W. Oates, T. M. Fortier, S. A. Diddams, L. Hollberg, C. W. Hoyt, A. V. Taichenachev, and V. I. Yudin, *Phys. Rev. Lett.* **100**, 103002 (2008).
- [31] A. D. Ludlow, N. D. Lemke, J. A. Sherman, C. W. Oates, G. Quémener, J. von Stecher, and A. M. Rey, *Phys. Rev. A* **84**, 052724 (2011).
- [32] S. Falke, N. Lemke, C. Grebing, B. Lipphardt, S. Weyers, V. Gerginov, N. Huntemann, C. Hagemann, A. Al-Masoudi, S. Häfner, S. Vogt, U. Sterr, and C. Lisdat, *New J. Phys.* **16**, 073023 (2014).
- [33] Other clock spectroscopy schemes can suppress it, as has been explored in Refs. [34–36].
- [34] V. I. Yudin, A. V. Taichenachev, C. W. Oates, Z. W. Barber, N. D. Lemke, A. D. Ludlow, U. Sterr, C. Lisdat, and F. Riehle, *Phys. Rev. A* **82**, 011804(R) (2010).
- [35] T. Zanon-Willette, S. Almonacil, E. de Clercq, A. D. Ludlow, and E. Arimondo, *Phys. Rev. A* **90**, 053427 (2014).
- [36] N. Huntemann, B. Lipphardt, M. Okhapkin, C. Tamm, E. Peik, A. V. Taichenachev, and V. I. Yudin, *Phys. Rev. Lett.* **109**, 213002 (2012).

Bibliography

- [1] A. L. SCHAWLOW,
Spectroscopy in a new light,
Nobel Lecture (1981).
- [2] I. I. RABI, S. MILLMAN, P. KUSCH, and J. R. ZACHARIAS,
The Molecular Beam Resonance Method for Measuring Nuclear Magnetic
Moments,
Phys. Rev. **55**, 526 (1939).
- [3] N. F. RAMSEY,
A New Molecular Beam Resonance Method,
Phys. Rev. **76**, 996 (1949).
- [4] N. F. RAMSEY,
A Molecular Beam Resonance Method with Separated Oscillating Fields,
Phys. Rev. **78**, 695 (1950).
- [5] WWW.NOBELPRIZE.ORG.
- [6] L. ESSEN and J. V. L. PARRY,
An Atomic Standard of Frequency and Time Interval: A Caesium Resonator,
Nature **176**, 280 (1955).
- [7] BUREAU INTERNATIONAL DES POIDS ET MESURES,
SI Brochure: The International System of Units (SI), volume 8th edition,
Organisation Intergouvernementale de la Convention du Mètre, 2006.
- [8] T. W. HÄNSCH and A. L. SCHAWLOW,
Cooling of gases by laser radiation,
Opt. Commun. **13**, 68 (1975).
- [9] D. J. WINELAND, R. DRULLINGER, and F. WALLS,
Radiation-pressure cooling of bound-resonant absorbers,
Phys. Rev. Lett. **40**, 1639 (1978).

-
- [10] A. CLAIRON, S. GHEZALI, G. SANTARELLI, P. LAURENT, E. SIMON, S. LEA, M. BAHOURA, S. WEYERS, and K. SZYMANIEC,
The LPTF preliminary accuracy evaluation of cesium fountain frequency standard,
10th International Conference on European Frequency and Time, 218 (1996).
- [11] S. R. JEFFERTS, D. M. MEEKHOF, J. H. SHIRLEY, T. E. PARKER, and F. LEVI,
Preliminary accuracy evaluation of a cesium fountain primary frequency standard at NIST,
Proceedings of the 1999 Joint Meeting of the European Frequency and Time Forum and the IEEE International Frequency Control Symposium **1**, 12 (1999).
- [12] S. WEYERS, U. HÜBNER, R. SCHRÖDER, C. TAMM, and A. BAUCH,
Uncertainty evaluation of the atomic caesium fountain CSF1 of the PTB,
Metrologia **38**, 343 (2001).
- [13] R. LI, K. GIBBLE, and K. SZYMANIEC,
Improved accuracy of the NPL-CsF2 primary frequency standard: evaluation of distributed cavity phase and microwave lensing frequency shifts,
Metrologia **48**, 283 (2011).
- [14] J. GUENA, M. ABGRALL, D. ROVERA, P. LAURENT, B. CHUPIN, M. LOURS, G. SANTARELLI, P. ROSENBUSCH, M. E. TOBAR, L. RUOXIN, K. GIBBLE, A. CLAIRON, and S. BIZE,
Progress in atomic fountains at LNE-SYRTE,
IEEE Transactions on Ultrasonics, Ferroelectrics and Frequency Control **59**, 391 (2012).
- [15] S. WEYERS, V. GERGINOV, N. NEMITZ, R. LI, and K. GIBBLE,
Distributed cavity phase frequency shifts of the caesium fountain PTB-CSF2,
Metrologia **49**, 82 (2012).
- [16] Evaluation of PTB primary caesium fountain frequency standard CSF2 between MJD 57169 - MJD 57199,
FTP server of the BIPM Time Department, 2015.
- [17] M. TAKAMOTO, F.-L. HONG, R. HIGASHI, and H. KATORI,
An optical lattice clock,
Nature **435**, 321 (2005).
- [18] H. SCHNATZ, B. LIPPARDT, J. HELMCKE, F. RIEHLE, and G. ZINNER,
First Phase-Coherent Frequency Measurement of Visible Radiation,
Phys. Rev. Lett. **76**, 18 (1996).

-
- [19] T. UDEM, A. HUBER, B. GROSS, J. REICHERT, M. PREVEDELLI, M. WEITZ, and T. W. HÄNSCH,
Phase-Coherent Measurement of the Hydrogen $1S-2S$ Transition Frequency with an Optical Frequency Interval Divider Chain,
Phys. Rev. Lett. **79**, 2646 (1997).
- [20] J. REICHERT, R. HOLZWARTH, T. UDEM, and T. W. HÄNSCH,
Measuring the frequency of light with mode-locked lasers,
Opt. Commun. **172**, 59 (1999).
- [21] T. UDEM, R. HOLZWARTH, and T. W. HÄNSCH,
Optical frequency metrology,
Nature **416**, 233 (2002).
- [22] D. J. JONES, S. A. DIDDAMS, J. K. RANKA, A. STENTZ, R. S. WINDELER, J. L. HALL, and S. T. CUNDIFF,
Carrier-Envelope Phase Control of Femtosecond Mode-Locked Lasers and Direct Optical Frequency Synthesis,
Science **288**, 635 (2000).
- [23] R. J. JONES, K. D. MOLL, M. J. THORPE, and J. YE,
Phase-Coherent Frequency Combs in the Vacuum Ultraviolet via High-Harmonic Generation inside a Femtosecond Enhancement Cavity,
Phys. Rev. Lett. **94**, 193201 (2005).
- [24] S. A. DIDDAMS, T. UDEM, J. C. BERGQUIST, E. A. CURTIS, R. E. DRULLINGER, L. HOLLBERG, W. M. ITANO, W. D. LEE, C. W. OATES, K. R. VOGEL, and D. J. WINELAND,
An Optical Clock Based on a Single Trapped $^{199}\text{Hg}^+$ Ion,
Science **293**, 825 (2001).
- [25] W. PAUL,
Electromagnetic traps for charged and neutral particles,
Rev. Mod. Phys. **62**, 531 (1990).
- [26] R. H. DICKE,
The Effect of Collisions upon the Doppler Width of Spectral Lines,
Physical Review **89**, 472 (1953).
- [27] J. C. BERGQUIST, W. M. ITANO, and D. J. WINELAND,
Recoilless optical absorption and Doppler sidebands of a single trapped ion,
Phys. Rev. A **36**, 428 (1987).
- [28] F. DIEDRICH, J. C. BERGQUIST, W. M. ITANO, and D. J. WINELAND,
Laser Cooling to the Zero-Point Energy of Motion,
Phys. Rev. Lett. **62**, 403 (1989).

- [29] K. PYKA, J. KELLER, H. L. PARTNER, R. NIGMATULLIN, T. BURGERMEISTER, D. M. MEIER, K. KUHLMANN, A. RETZKER, M. B. PLENIO, W. H. ZUREK, A. DEL CAMPO, and T. E. MEHLSTÄUBLER, Topological defect formation and spontaneous symmetry breaking in ion Coulomb crystals, *Nat. Comm.* **4** (2013).
- [30] P. S. JESSEN and I. H. DEUTSCH, Optical Lattices, *Adv. At. Mol. Opt. Phys* **37**, 95 (1996).
- [31] T. IDO and H. KATORI, Recoil-Free Spectroscopy of Neutral Sr Atoms in the Lamb-Dicke Regime, *Phys. Rev. Lett.* **91**, 053001 (2003).
- [32] H. KATORI, M. TAKAMOTO, V. G. PAL'CHIKOV, and V. D. OVSIANNIKOV, Ultrastable Optical Clock with Neutral Atoms in an Engineered Light Shift Trap, *Phys. Rev. Lett.* **91**, 173005 (2003).
- [33] R. W. P. DREVER, J. L. HALL, F. V. KOWALSKI, J. HOUGH, G. M. FORD, A. J. MUNLEY, and H. WARD, Laser phase and frequency stabilization using an optical resonator, *Appl. Phys. B* **31**, 97 (1983).
- [34] M. J. THORPE, L. RIPPE, T. M. FORTIER, M. S. KIRCHNER, and T. ROSEN BAND, Frequency stabilization to 6×10^{-16} via spectral-hole burning, *Nat. Photonics* **5**, 688 (2011).
- [35] H. S. MARGOLIS, Optical frequency standards and clocks, *Contemporary Physics* **51**, 37 (2009).
- [36] T. MIDDELMANN, S. FALKE, C. LISDAT, and U. STERR, High Accuracy Correction of Blackbody Radiation Shift in an Optical Lattice Clock, *Phys. Rev. Lett.* **109**, 263004 (2012).
- [37] J. A. SHERMAN, N. D. LEMKE, N. HINKLEY, M. PIZZOCARO, R. W. FOX, A. D. LUDLOW, and C. W. OATES, High-Accuracy Measurement of Atomic Polarizability in an Optical Lattice Clock, *Phys. Rev. Lett.* **108**, 153002 (2012).

-
- [38] B. J. BLOOM, T. L. NICHOLSON, J. R. WILLIAMS, S. L. CAMPBELL, M. BISHOF, X. ZHANG, W. ZHANG, S. L. BROMLEY, and J. YE, An optical lattice clock with accuracy and stability at the 10^{-18} level, *Nature* (2014).
- [39] I. USHIJIMA, M. TAKAMOTO, M. DAS, T. OHKUBO, and H. KATORI, Cryogenic optical lattice clocks, *Nat. Photonics* **9**, 185 (2015).
- [40] T. L. NICHOLSON, S. L. CAMPBELL, R. B. HUTSON, G. E. MARTI, B. J. BLOOM, R. L. MCNALLY, W. ZHANG, M. D. BARRETT, M. S. SAFRONOVA, G. F. STROUSE, W. L. TEW, and J. YE, Systematic evaluation of an atomic clock at 2×10^{-18} total uncertainty, *Nat. Comm.* **6**, 6896 (2015).
- [41] W. H. OSKAY, S. A. DIDDAMS, E. A. DONLEY, T. M. FORTIER, T. P. HEAVNER, L. HOLLBERG, W. M. ITANO, S. R. JEFFERTS, M. J. DELANEY, K. KIM, F. LEVI, T. E. PARKER, and J. C. BERGQUIST, Single-Atom Optical Clock with High Accuracy, *Phys. Rev. Lett.* **97**, 020801 (2006).
- [42] R. E. BEEHLER, R. C. MOCKLER, and J. M. RICHARDSON, Cesium Beam Atomic Time and Frequency Standards, *Metrologia* **1**, 114 (1965).
- [43] A. G. MUNGALL, H. DAAMS, D. MORRIS, and C. C. COSTAIN, Performance and Operation of the NRC Primary Cesium Clock, CsV , *Metrologia* **12**, 129 (1976).
- [44] A. G. MUNGALL, H. DAAMS, and J.-S. BOULANGER, Design, Construction, and Performance of the NRC CsVI Primary Cesium Clocks, *Metrologia* **17**, 123 (1981).
- [45] A. BAUCH, K. DORENWENDT, B. FISCHER, T. HEINDORFF, E. K. MÜLLER, and R. SCHRÖDER, CS2: The PTB's new primary clock, *IEEE Transactions on Instrumentation and Measurement* **36**, 613 (1987).
- [46] A. CLAIRON, P. LAURENT, G. SANTARELLI, S. GHEZALI, S. N. LEA, and M. BAHOURA, A cesium fountain frequency standard: preliminary results, *IEEE Transactions on Instrumentation and Measurement* **44**, 128 (1995).

- [47] V. GERGINOV, N. NEMITZ, S. WEYERS, R. SCHRÖDER, D. GRIEBSCH, and R. WYNANDS,
Uncertainty evaluation of the caesium fountain clock PTB-CSF2,
Metrologia **47**, 65 (2010).
- [48] T. ROSENBAND, D. B. HUME, P. O. SCHMIDT, C. W. CHOU, A. BRUSCH, L. LORINI, W. H. OSKAY, R. E. DRULLINGER, T. M. FORTIER, J. E. STALNAKER, S. A. DIDDAMS, W. C. SWANN, N. R. NEWBURY, W. M. ITANO, D. J. WINELAND, and J. C. BERGQUIST,
Frequency Ratio of Al⁺ and Hg⁺ Single-Ion Optical Clocks; Metrology at the 17th Decimal Place,
Science **319**, 1808 (2008).
- [49] J. STENGER, C. TAMM, N. HAVERKAMP, S. WEYERS, and H. R. TELLE,
Absolute frequency measurement of the 435.5-nm ¹⁷¹Yb⁺-clock transition with a Kerr-lens mode-locked femtosecond laser,
Opt. Lett. **26**, 1589 (2001).
- [50] C. W. CHOU, D. B. HUME, J. C. J. KOELEMENIJ, D. J. WINELAND, and T. ROSENBAND,
Frequency Comparison of Two High-Accuracy Al⁺ Optical Clocks,
Phys. Rev. Lett. **104**, 070802 (2010).
- [51] X. BAILLARD et al.,
Optical Lattice Clock with Spin-polarized ⁸⁷Sr Atoms,
Quantum Communications Realized **6780** (2007).
- [52] N. POLI, Z. W. BARBER, N. LEMKE, C. W. OATES, L. S. MA, J. E. STALNAKER, T. M. FORTIER, S. A. DIDDAMS, L. HOLLBERG, J. C. BERGQUIST, A. BRUSCH, S. JEFFERTS, T. HEAVNER, and T. PARKER,
Frequency evaluation of the doubly forbidden ¹S₀ → ³P₀ transition in bosonic ¹⁷⁴Yb,
Phys. Rev. A **77**, 050501(R) (2008).
- [53] N. D. LEMKE, A. D. LUDLOW, Z. W. BARBER, T. M. FORTIER, S. A. DIDDAMS, Y. JIANG, S. R. JEFFERTS, T. P. HEAVNER, T. E. PARKER, and C. W. OATES,
Spin-1/2 Optical Lattice Clock,
Phys. Rev. Lett. **103**, 063001 (2009).
- [54] S. FALKE, H. SCHNATZ, J. S. R. V. WINFRED, T. MIDDELMANN, S. VOGT, S. WEYERS, B. LIPPARDT, G. GROSCHE, F. RIEHLE, U. STERR, and C. LISDAT,
The ⁸⁷Sr optical frequency standard at PTB,
Metrologia **48**, 399 (2011).

- [55] S. FALKE, N. LEMKE, C. GREBING, B. LIPPHARDT, S. WEYERS, V. GERGINOV, N. HUNTEMANN, C. HAGEMANN, A. AL-MASOUDI, S. HÄFNER, S. VOGT, U. STERR, and C. LISDAT, A strontium lattice clock with 3×10^{-17} inaccuracy and its frequency, *New J. Phys.* **16**, 073023 (2014).
- [56] J. FRIEBE, A. PAPE, M. RIEDMANN, K. MOLDENHAUER, T. MEHLSTÄUBLER, N. REHBEIN, C. LISDAT, E. M. RASEL, W. ERTMER, H. SCHNATZ, B. LIPPHARDT, and G. GROSCHE, Absolute frequency measurement of the magnesium intercombination transition $^1S_0 \rightarrow ^3P_1$, *Phys. Rev. A* **78**, 033830 (2008).
- [57] J. FRIEBE, M. RIEDMANN, T. WÜBBENA, A. PAPE, H. KELKAR, W. ERTMER, U. STERR, S. WEYERS, G. GROSCHE, H. SCHNATZ, and E. M. RASEL, Remote frequency measurement of the $^1S_0 \rightarrow ^3P_1$ transition in laser-cooled ^{24}Mg , *New J. Phys.* **13**, 125010 (2011).
- [58] C. W. CHOU, D. B. HUME, T. ROSENBAND, and D. J. WINELAND, Optical Clocks and Relativity, *Science* **329**, 1630 (2010).
- [59] J. W. THOMSEN, Nonlinear Dispersion with Narrow Linewidth Atoms in an Optical Cavity, 2015, Colloquium for the Research Training Group (RTG) 1729.
- [60] R. BONDARESCU, M. BONDARESCU, G. HETÉNYI, L. BOSCHI, P. JETZER, and J. BALAKRISHNA, Geophysical applicability of atomic clocks: direct continental geoid mapping, *Geophys. J. Int.* **191**, 78 (2012).
- [61] E. MAI and J. MÜLLER, General remarks on the potential use of atomic clocks in relativistic geodesy, *ZfV - Zeitschrift für Geodäsie, Geoinformation und Landmanagement* **138**, 257 (2013).
- [62] SONDERFORSCHUNGSBEREICH (SFB) 1128 GEO-Q, <http://www.geoq.uni-hannover.de/mission.html>.
- [63] S. G. PORSEV and A. DEREVIANKO, Multipolar theory of blackbody radiation shift of atomic energy levels and its implications for optical lattice clocks,

- Phys. Rev. A* **74**, 020502(R) (2006).
- [64] M. RIEDMANN,
Optisches Speichern von Magnesium,
PhD thesis, Leibniz Universität Hannover, 2011.
- [65] M. RIEDMANN, H. KELKAR, T. WÜBBENA, A. PAPE, A. KULOSA,
K. ZIPFEL, D. FIM, S. RÜHMANN, J. FRIEBE, W. ERTMER, and
E. RASEL,
Beating the density limit by continuously loading a dipole trap from
milliKelvin-hot magnesium atoms,
Phys. Rev. A **86**, 043416 (2012).
- [66] T. W. WÜBBENA,
*Spektroskopie des $^1S_0 \rightarrow ^3P_0$ Uhrenübergangs von ^{24}Mg in einem optischen
Gitter bei der vorhergesagten magischen Wellenlänge*,
PhD thesis, Leibniz Universität Hannover, 2012.
- [67] A. V. TAICHENACHEV, V. I. YUDIN, C. W. OATES, C. W. HOYT, Z. W.
BARBER, and L. HOLLBERG,
Magnetic Field-Induced Spectroscopy of Forbidden Optical Transitions with
Application to Lattice-Based Optical Atomic Clocks,
Phys. Rev. Lett. **96**, 083001 (2006).
- [68] Z. W. BARBER, C. W. HOYT, C. W. OATES, and L. HOLLBERG,
Direct Excitation of the Forbidden Clock Transition in Neutral ^{174}Yb Atoms
Confined to an Optical Lattice,
Phys. Rev. Lett. **96**, 083002 (2006).
- [69] Y. LIN, Q. WANG, Y. LI, B. LIN, S. WANG, F. MENG, Y. ZHAO, J. CAO,
E. ZANG, T. LI, and Z. FANG,
Magnetic Field Induced Spectroscopy of ^{88}Sr Atoms Probed with a 10 Hz
Linewidth Laser,
Chin. Phys. Lett. **30**, 014206 (2013).
- [70] K. MOLDENHAUER,
*Sub-Doppler-Kühlung und magnetische Speicherung von Magnesiumatomen
bei Temperaturen unter 1 mK*,
PhD thesis, Leibniz Universität Hannover, 2008.
- [71] T. MEHLSTÄUBLER,
Neuartige Kühlmethode für einen optischen Magnesium-Frequenzstandard,
PhD thesis, Leibniz Universität Hannover, 2005.

-
- [72] J. FRIEBE,
Ein optischer Frequenzstandard mit lasergekühlten Magnesiumatomen,
PhD thesis, Leibniz Universität Hannover, 2010.
- [73] N. REHBEIN,
Realisierung neuer Laserkühlverfahren und Spektroskopielaser für einen optischen Magnesium-Frequenzstandard,
PhD thesis, Leibniz Universität Hannover, 2006.
- [74] C. J. FOOT,
Atomic Physics,
Oxford University Press, 2005.
- [75] P. V. D. S. HAROLD J. METCALF,
Laser cooling and Trapping,
Springer, 1999.
- [76] T. MAYER-KUCKUK,
Atomphysik,
Teubner Studienbücher, 1980.
- [77] J. S. COURSEY, D. J. SCHWAB, J. J. TSAI, and R. A. DRAGOSSET,
NIST Standard Reference Data 144, Atomic Weights and Isotopic Compositions.
- [78] W. DEMTRÖDER,
Experimentalphysik 4: Kern-, Teilchen- und Astrophysik,
Springer, 2005.
- [79] W. DEMTRÖDER,
Experimentalphysik 3: Atome, Moleküle und Festkörper,
Springer, 2005.
- [80] G. AUDI, A. H. WAPSTRA, and C. THIBAULT,
The AME2003 atomic mass evolution (II). Tables, graphs and references,
Nucl. Phys. A **729**, 337 (2003).
- [81] C. WIEMAN and T. W. HÄNSCH,
Doppler-Free Laser Polarization Spectroscopy,
Phys. Rev. Lett. **36**, 1170 (1976).
- [82] J. FRIEBE,
Effiziente Erzeugung von ultraviolettem Licht mit neuartigen Kristallstrukturen,
Diplomarbeit, Institut für Quantenoptik, Universität Hannover, 2005.

-
- [83] W. DEMTRÖDER,
Laserspektroskopie 1,
Springer, 2011.
- [84] P. L. HANSEN, K. T. THERKILDSSEN, N. MALOSI, B. B. JENSEN, E. D. VAN OOIJEN, A. BRUSCH, J. H. MÜLLER, J. HALD, and J. W. THOMSEN,
Measurement of the $3s3p^3P_1$ lifetime in magnesium using a magneto-optical trap,
Phys. Rev. A **77**, 062502 (2008).
- [85] D. BUDKER, S. M. ROCHESTER, and V. V. YASHCHUK,
Obtaining frequency markers of variable separation with a spherical mirror Fabry-Perot interferometer,
Rev. Sci. Instrum. **71**, 2984 (2000).
- [86] A. P. KULOSA, J. FRIEBE, M. P. RIEDMANN, A. PAPE, T. W. WÜBBENA, D. B. FIM, S. RÜHMANN, K. H. ZIPFEL, H. KELKAR, W. ERTMER, and E. M. RASEL,
An ultraviolet laser system for laser cooling and trapping of metastable magnesium,
arXiv:1201.3856 (2012).
- [87] A. VOSKREBENZEV,
Aufbau und Test eines Lasersystems zur Kühlung metastabiler Magnesiumatome,
Diplomarbeit, Leibniz Universität Hannover, 2007.
- [88] C. Y. YANG, P. HALDER, O. APPEL, D. HANSEN, and A. HEMMERICH,
Continuous loading of 1S_0 calcium atoms into an optical dipole trap,
Phys. Rev. A **76**, 033418 (2007).
- [89] A. BRUSCH, R. L. TARGAT, X. BAILLARD, M. FOUCHÉ, and P. LEMONDE,
Hyperpolarizability Effects in a Sr Optical Lattice Clock,
Phys. Rev. Lett. **96**, 103003 (2006).
- [90] M. S. SAFRONOVA,
Private communication, 2011.
- [91] K. ZIPFEL,
Realisierung eines Überhöhungsresonators für die optische Speicherung von Magnesium,
Masterarbeit, Leibniz Universität Hannover, 2011.

-
- [92] A. PAPE, O. TERRA, J. FRIEBE, M. RIEDMANN, T. WÜBBENA, E. M. RASEL, K. PREDEHL, T. LEGERO, B. LIPPHARDT, H. SCHNATZ, and G. GROSCHE,
Long-distance remote comparison of ultrastable optical frequencies with 10^{-15} instability in fractions of a second,
Opt. Express **18**, 21477 (2010).
- [93] A. PAPE,
Hochstabiler Lokaloszillator für einen optischen Magnesium-Frequenzstandard,
PhD thesis, Leibniz Universität Hannover, 2012.
- [94] F. RIEHLE,
Frequency Standards,
WILEY-VCH Verlag GmbH & Co. KGaA, 2004.
- [95] C. J. BORDÉ, C. SALOMON, S. AVRILLIER, A. VAN LERBERGHE, C. BRÉANT, D. BASSI, and G. SCOLES,
Optical Ramsey fringes with traveling waves,
Phys. Rev. A **30**, 1836 (1984).
- [96] N. BEVERINI, S. D. PASCALIS, E. MACCIONI, D. PEREIRA, F. STRUMIA, G. VISSANI, Y. Z. WANG, and C. NOVERO,
Evidence for laser cooling in a magnesium atomic beam,
Opt. Lett. **14**, 350 (1989).
- [97] T. E. MEHLSTÄUBLER, J. KEUPP, A. DOUILLET, N. REHBEIN, E. M. RASEL, and W. ERTMER,
Modelling three-dimensional-quench cooling for alkaline-earth atoms,
J. Opt. B: Quantum Semiclass. Opt. **5**, S183 (2003).
- [98] T. IDO, T. H. LOFTUS, M. M. BOYD, A. D. LUDLOW, K. W. HOLMAN, and J. YE,
Precision Spectroscopy and Density-Dependent Frequency Shifts in Ultracold Sr,
Phys. Rev. Lett **94**, 153001 (2005).
- [99] C. W. HOYT, Z. W. BARBER, C. W. OATES, T. M. FORTIER, S. A. DIDDAMS, and L. HOLLBERG,
Observation and Absolute Frequency Measurement of the 1S_0 - 3P_0 Optical Clock Transition in Neutral Ytterbium,
Phys. Rev. Lett. **95**, 083003 (2005).
- [100] D. J. WINELAND and W. M. ITANO,
Laser cooling of atoms,

- Phys. Rev. A* **20**, 1521 (1979).
- [101] R. LOUDON,
The Quantum Theory of Light,
Oxford Science Publications, 1991.
- [102] J. ESCHNER, G. MORIGI, F. SCHMIDT-KALER, and R. BLATT,
Laser cooling of trapped ions,
J. Opt. Soc. Am. B **20**, 1003 (2003).
- [103] W. NOLTING,
Grundkurs Theoretische Physik 5/1,
Springer-Verlag Berlin-Heidelberg, 2009.
- [104] D. LEIBFRIED, R. BLATT, C. MONROE, and D. J. WINELAND,
Quantum dynamics of single trapped ions,
Rev. Mod. Phys. **75**, 281 (2003).
- [105] D. J. WINELAND, C. MONROE, W. M. ITANO, D. LEIBFRIED, B. E. KING, and D. M. MEEKHOF,
Experimental Issues in Coherent Quantum-State Manipulation of Trapped Atomic Ions,
J. Res. Natl. Stand. Technol. **103**, 259 (1998).
- [106] D. J. WINELAND, W. M. ITANO, J. C. BERGQUIST, and R. G. HULET,
Laser-cooling limits and single-ion spectroscopy,
Phys. Rev. A **36**, 2220 (1987).
- [107] R. GRIMM, M. WEIDEMÜLLER, and Y. B. OVCHINNIKOV,
Optical Dipole Traps for Neutral Atoms,
Adv. At. Mol. Opt. Phys **42**, 95 (2000).
- [108] L. YI, S. MEJRI, J. J. MCFERRAN, Y. L. COQ, and S. BIZE,
Optical Lattice Trapping of ^{199}Hg and Determination of the Magic Wavelength for the Ultraviolet $^1S_0 \leftrightarrow ^3P_0$ Clock Transition,
Phys. Rev. Lett. **106**, 073005 (2011).
- [109] S. BLATT, J. W. THOMSEN, G. K. CAMPBELL, A. D. LUDLOW, M. D. SWALLOWS, M. J. MARTIN, M. M. BOYD, and J. YE,
Rabi spectroscopy and excitation inhomogeneity in a one-dimensional optical lattice clock,
Phys. Rev. A **80**, 052703 (2009).
- [110] M. S. SAFRONOVA,
Private communication, 2015.

-
- [111] V. D. OVSIANNIKOV, V. G. PAL'CHIKOV, A. V. TAICHENACHEV, V. I. YUDIN, H. KATORI, and M. TAKAMOTO,
Magic-wave-induced 1S_0 - 3P_0 transition in even isotopes of alkaline-earth-metal-like atoms,
Phys. Rev. A **75** (2007).
- [112] R. SANTRA, K. V. CHRIST, and C. H. GREENE,
Properties of metastable alkaline-earth-metal atoms calculated using an accurate effective core potential,
Phys. Rev. A **69**, 042510 (2004).
- [113] K. ZIPFEL,
Untersuchungen zur Realisierung des optischen Speicherns von Magnesium, Bachelorarbeit, Leibniz Universität Hannover, 2009.
- [114] M. TAKAMOTO and H. KATORI,
Spectroscopy of the 1S_0 - 3P_0 Clock Transition of ^{87}Sr in an Optical Lattice,
Phys. Rev. Lett. **91**, 223001 (2003).
- [115] S. SAUER,
Optische Manipulation von Magnesiumatomen,
Master's thesis, Leibniz Universität Hannover, 2014.
- [116] P. LEMONDE and P. WOLF,
Optical lattice clock with atoms confined in a shallow trap,
Phys. Rev. A **72**, 033409 (2005).
- [117] H. IBERG and H. LÜTH,
Festkörperphysik - Eine Einführung in die Grundlagen,
Springer-Verlag Berlin Heidelberg New York, 1981.
- [118] S. NOSCHESI, L. PASQUINI, and L. REICHEL,
Tridiagonal Toeplitz matrices: Properties and novel applications,
Numer. Linear Algebra Appl. **20**, 302 (2013).
- [119] I. V. HERTEL and C.-P. SCHULZ,
Atome, Moleküle und optische Physik 2,
Springer-Verlag Berlin Heidelberg, 2010.
- [120] P. WOLF,
Private communication, 2014.
- [121] A. GODONE and C. NOVERO,
The Magnesium Frequency Standard,
Metrologia **30**, 163 (1993).

-
- [122] J. LODEWYCK,
Private communication, 2015.
- [123] N. HINKLEY, J. A. SHERMAN, N. B. PHILLIPS, M. SCHIOPPO, N. D. LEMKE, K. BELOY, M. PIZZOCARO, C. W. OATES, and A. D. LUDLOW,
An Atomic Clock with 10^{-18} Instability,
Science **341**, 6151 (2013).
- [124] A. V. TAICHENACHEV,
Private communication, 2015.
- [125] P. G. WESTERGAARD, J. LODEWYCK, L. LORINI, A. LECALLIER, E. A. BURT, M. ZAWADA, J. MILLO, and P. LEMONDE,
Lattice-Induced Frequency Shifts in Sr Optical Lattice Clocks at the 10^{-17} Level,
Phys. Rev. Lett. **106**, 210801 (2011).
- [126] K. W. MADISON, M. C. FISCHER, R. B. DIENER, Q. NIU, and M. G. RAIZEN,
Dynamical Bloch Band Suppression in an Optical Lattice,
Phys. Rev. Lett. **81**, 5093 (1998).
- [127] I. BLOCH,
Ultracold quantum gases in optical lattice,
Nature Physics **1**, 23 (2005).
- [128] D. FIM,
PhD thesis, Leibniz Universität Hannover, in preparation.
- [129] D. MESCHEDE,
Optik, Licht und Laser,
Teubner, 2005.
- [130] J. HEINZE, 2015,
Bachelor thesis, in preparation.
- [131] Z. W. BARBER, J. E. STALNAKER, N. D. LEMKE, N. POLI, C. W. OATES, T. M. FORTIER, S. A. DIDDAMS, L. HOLLBERG, C. W. HOYT, A. V. TAICHENACHEV, and V. I. YUDIN,
Optical Lattice Induced Light Shifts in an Yb Atomic Clock,
Phys. Rev. Lett. **100**, 103002 (2008).
- [132] V. KAUFMAN and W. C. MARTIN,
Wavelengths and Energy Level Classifications of Magnesium Spectra for All Stages of Ionization (Mg I through Mg XII),

- J. Phys. Chem. Ref. Data* **20**, 83 (1991).
- [133] D. E. KELLEHER and L. I. PODOBEDOVA,
Atomic Transition Probabilities of Sodium and Magnesium. A Critical Com-
pilation,
J. Phys. Chem. Ref. Data **37**, 267 (2008).
- [134] K. BELOY, J. A. SHERMAN, N. D. LEMKE, N. HINKLEY, C. W. OATES,
and A. D. LUDLOW,
Determination of the $5d6s\ ^3D_1$ state lifetime and blackbody-radiation clock
shift in Yb,
Phys. Rev. A **86**, 051404 (2012).
- [135] S. G. PORSEV and A. DEREVIANKO,
Erratum: Multipolar theory of blackbody radiation shift of atomic energy
levels and its implications for optical lattice clocks [Phys. Rev. A 74,
020502(R) (2006)],
Phys. Rev. A **86**, 029904(E) (2012).
- [136] N. HUNTEMANN, B. LIPPHARDT, M. OKHAPKIN, C. TAMM, E. PEIK,
A. V. TAICHENACHEV, and V. I. YUDIN,
Generalized Ramsey Excitation Scheme with Suppressed Light Shift,
Phys. Rev. Lett **109**, 213002 (2012).
- [137] T. ZANON-WILLETTE, S. ALMONACIL, E. DE CLERCQ, A. D. LUDLOW,
and E. ARIMONDO,
Quantum engineering of atomic phase-shifts in optical clocks,
Phys. Rev. A **90**, 053427 (2014).
- [138] G. K. CAMPBELL, A. D. LUDLOW, S. BLATT, J. W. THOMSEN, M. J.
MARTIN, M. H. G. DE MIRANDA, T. ZELEVINSKY, M. M. BOYD,
J. YE, S. A. DIDDAMS, T. P. HEAVNER, T. E. PARKER, and S. R.
JEFFERTS,
The absolute frequency of the ^{87}Sr clock transition,
Metrologia **45**, 539 (2008).
- [139] C. LISDAT, J. S. R. V. WINFRED, T. MIDDELMANN, F. RIEHLE, and
U. STERR,
Collisional Losses, Decoherence, and Frequency Shifts in Optical Lattice
Clocks with Bosons,
Phys. Rev. Lett **103**, 090801 (2009).
- [140] T. AKATSUKA, M. TAKAMOTO, and H. KATORI,
Optical lattice clocks with non-interacting bosons and fermions,
Nature Physics **4**, 954 (2008).

-
- [141] M. M. BOYD, T. ZELEVINSKY, A. D. LUDLOW, S. BLATT, T. ZANON-WILLETTE, S. M. FOREMAN, and J. YE,
Nuclear spin effects in optical lattice clocks,
Phys. Rev. A **76**, 022510 (2007).
- [142] A. D. LUDLOW, M. M. BOYD, J. YE, E. PEIK, and P. O. SCHMIDT,
Optical Atomic Clocks,
Rev. Mod. Phys. **87**, 637 (2015).
- [143] M. TAKAMOTO, F.-L. HONG, R. HIGASHI, Y. FUJII, M. IMAE, and H. KATORI,
Improved Frequency Measurement of a One-Dimensional Optical Lattice Clock with a Spin-Polarized Fermionic ^{87}Sr Isotope,
J. Phys. Soc. Jpn. **75**, 104302 (2006).
- [144] E. L. HAZLETT, Y. ZHANG, R. W. STITES, K. GIBBLE, and K. M. O'HARA,
 s -Wave Collisional Frequency Shift of a Fermion Clock,
Phys. Rev. Lett. **110**, 160801 (2013).
- [145] K. BONGS et al.,
Development of a strontium optical lattice clock for the SOC mission on the ISS,
arXiv:1503.08457 (2015).
- [146] J. DALIBARD and C. COHEN-TANNOUDJI,
Laser cooling below the Doppler limit by polarization gradients: simple theoretical models,
J. Opt. Soc. Am. B **6**, 2023 (1989).
- [147] T. BINNEWIES, G. WILPERS, U. STERR, F. RIEHLE, J. HELMCKE, T. E. MEHLSTÄUBLER, E. M. RASEL, and W. ERTMER,
Doppler Cooling and Trapping on Forbidden Transitions,
Phys. Rev. Lett. **87**, 123002 (2001).
- [148] N. REHBEIN, T. E. MEHLSTÄUBLER, J. KEUPP, K. MOLDENHAUER, E. M. RASEL, W. ERTMER, A. DOUILLET, V. MICHELS, S. G. PORSEV, A. DEREVIANKO, C. F. FISCHER, G. I. TACHIEV, and V. G. PAL'CHIKOV,
Optical quenching of metastable magnesium,
Phys. Rev. A **76**, 043406 (2007).
- [149] A. GODONE, E. BAVA, and G. GIUSFREDI,
Isotopic Shift in the $^3\text{P}_1$ - $^3\text{P}_0$ Mg Transition,
Z. Phys. A-Atoms and Nuclei **318**, 131 (1984).

-
- [150] U. STERR, K. SENGSTOCK, J. H. MÜLLER, and W. ERTMER,
High-Resolution Isotope Shift Measurement of the Mg I 1S_0 - 3P_1 Intercombination Transition,
Appl. Phys. B **56**, 62 (1993).
- [151] M. McDONALD, B. H. MCGUYER, G. Z. IWATA, and T. ZELEVINSKY,
Thermometry via Light Shifts in Optical Lattices,
Phys. Rev. Lett. **114**, 023001 (2015).
- [152] J. WEINER, V. S. BAGNATO, S. ZILIO, and P. S. JULIENNE,
Experiments and theory in cold and ultracold collisions,
Rev. Mod. Phys. **71**, 1 (1999).
- [153] T. P. DINNEEN, K. R. VOGEL, E. ARIMONDO, J. L. HALL, and A. GALLAGHER,
Cold collisions of Sr*-Sr in a magneto-optical trap,
Phys. Rev. A **59**, 1216 (1999).

LIST OF FIGURES

1.1	Principle of optical clocks	4
1.2	Fractional uncertainties of atomic frequency standards	5
2.1	Horizontal cut through the experimental chamber	9
2.2	Calibration of the magnetic field coils	11
3.1	Relevant level scheme of ^{24}Mg	16
3.2	Generated laser power at 285 nm	18
3.3	Beat measurement between the triplet-MOT cooling laser and RP 2	20
3.4	Reduced schematic setup of the laser system at 383 nm	21
3.5	Loading curve of the triplet-MOT	22
3.6	Schematic of the lattice setup	24
3.7	Interrogation of the clock transition	25
3.8	Schematic of the clock laser setup	27
4.1	Illustration of the Lamb-Dicke regime	32
4.2	Radiation spectrum in harmonic confinement	36
4.3	Possible transitions in the Lamb-Dicke regime	38
4.4	Optical lattice potential	41
4.5	Polarizabilities of the clock states	43
4.6	Inhomogeneous broadening due to a lattice AC Stark shift	44
4.7	Effect of radial motion on the blue sideband	45
4.8	Effective frequency spectrum in lattice spectroscopy	46
4.9	Excited state population as a function of temperature and tilting angle	48
4.10	Energy dispersion as a function of lattice quasimomentum	49
4.11	Band widths as a function of trap depth	50
4.12	Scheme of optical spectroscopy of Bloch bands	51
4.13	Simulation of the carrier spectrum	52
4.14	Simulation of the carrier spectrum featuring an AC Stark shift	53
5.1	Frequency scan of the $^1S_0 \rightarrow ^3P_0$ clock transition	58

5.2	AC Stark shift for different lattice wavelengths	60
5.3	Measurement of differential ac Stark shift	61
5.4	Measurement of the quadratic Zeeman shift	62
5.5	Carrier spectroscopy for different trap depths	65
5.6	Carrier spectroscopy for different ramping depths	67
5.7	Carrier spectroscopy at different lattice wavelengths	70
5.8	Determination of the magic wavelength	72
6.1	Purification scheme of higher-order bands	79
A.1	Decay rate of the triplet-MOT for different cooling laser powers . . .	88
A.2	Decay rate of the triplet-MOT for different cooling laser detunings .	88
A.3	Temperature measurement of the triplet-MOT	89
B.1	Fitting of the carrier line shape	91

LIST OF TABLES

4.1	Trap depths and corresponding ground state band widths	52
5.1	Comparison of isotopic recoil energies	59
5.2	Comparison of atomic species	63
5.3	Evaluation of the carrier resonance characteristics	71
6.1	Maximum lattice depth for different waist/power configurations . .	77

ACKNOWLEDGEMENTS

An dieser Stelle möchte ich mich bei allen Menschen bedanken, die mich während meiner Doktorarbeit am Institut für Quantenoptik begleitet oder betreut haben und auf die eine oder andere Art und Weise das Entstehen dieses Dokuments ermöglicht haben.

Mein erster Dank gebührt meinem Doktorvater, Prof. Dr. Ernst Rasel, der mich während meiner Promotionszeit gefördert, aber auch gefordert hat. Er hat mich mit offenen Armen in seine Arbeitsgruppe aufgenommen und mir eine Ausbildung ermöglicht, die außerordentlich facetten- und lehrreich war. Ich blicke dankbar auf eine sehr wertvolle Zeit zurück und möchte keinen Moment davon missen: die guten Momente, wo wir uns gemeinsam über Erreichtes freuen konnten, aber auch Momente, die zäh und unerfreulich waren, man jedoch bei ihm immer eine offene Tür vorgefunden hat und ermunternde Gespräche führen konnte.

Prof. Dr. Wolfgang Ertmer danke ich für die freundliche Übernahme des Korreferats dieser Doktorarbeit. Sein steter Einsatz für die Physik am Standort Hannover hat es ermöglicht, dass wir in einem exzellenten Forschungsumfeld arbeiten können, das auch in Zukunft weiter expandieren darf und jungen Forschern eine einzigartige Perspektive bieten wird. Ihm sei auch gedankt, dass er für "sein altes" Magnesium-Experiment stets großes Interesse hat und wir gemeinsam mit ihm zahlreiche und gute Diskussionen führen konnten.

I gratefully acknowledge Prof. Dr. Kurt Gible for reviewing this thesis. I first met Kurt Gible during a summer school in Bad Honnef, when I was a young graduate student and way too shy to start a discussion with a renown scientist of his kind. In my ongoing life as a PhD student, having discarded most of my shyness, I appreciate a lot that he always gave me the feeling to meet each other eye-to-eye while discussing about physics, although he mostly had been right. During his time in Hannover, I learned a lot from him. His way of thinking and working truly has been an inspiration for me. I am glad that he has always been available for my questions and needs for discussion, even though there is a time delay of six hours between Penn State and Hannover. As Kurt's German is constantly improving: Hab vielen Dank für alles!

Ich danke Prof. Dr. Bernd Weferling, dass er mich gegen Ende meines Studiums

dazu ermutigt hat, meinen Weg zu gehen. Es war mir eine große Freude, ihm während seiner Saturday Morning Lecture an der Leibniz Uni assistieren zu dürfen. Seine Art, die Menschen für die Astrophysik zu begeistern, ist einmalig. Ohne seine gedanklichen Anstöße und Ratschläge wäre diese Arbeit wohl niemals entstanden.

Dr. Rüdiger Scholz danke ich dafür, dass er im Jahr 2008 einem wissenschaftsinteressierten Studenten die Tür in das Institut für Quantenoptik geöffnet hat. Dank ihm konnte ich damals bereits meine Examensarbeit in diesem Institut verfassen und einen Weg einschlagen, der es absolut lohnenswert war, ihn zu gehen. Darüber hinaus freut es mich sehr, dass wir gemeinsam mit unserer Institutsband musikalischen Schwung in die alljährliche Weihnachtsfeier bringen können.

Ein ganz großer Dank gebührt dem Magnesium-Team für eine wahnsinnig spannende Zeit. Gemeinsam haben wir Höhen und Tiefen durchlebt und sind unseren Zielen aber immer stetig näher gekommen. Ich danke Steffen Rühmann, Dominika Fim, Klaus Zipfel, Nandan Jha und Steffen Sauer für eine einzigartige Zusammenarbeit und ihren Beitrag zu den Ergebnissen dieser Doktorarbeit. Meinen ehemaligen Kollegen Dr. Temmo Wübbena, Dr. André Pape, Dr. Matthias Riedmann, Dr. Jan Friebe und Dr. Hrishikesh Kelkar danke ich dafür, dass sie mich damals in das Experiment eingeführt haben und dass ich von ihnen lernen durfte. Unseren Studenten Waldemar Friesen, Joscha Heinze, Daniel Holzwart, Birte Lampmann, Sina Loriani, Lennart Wissel, Dennis Schröter, Tim Fischer, Oliver Kranz, Daniel Steinmeyer, Timotheus Alig, Andreas Sawadsky und Sina Malobabic, meinen SOCHiWis Christian Bick, Andreas Noack und Nils Wenzlaff, sowie unseren FWJlern Leonie Theis und Malte Brinkmann, die ich alle in meiner Doktorandenzeit erleben durfte, danke ich für ihren großartigen Einsatz am Experiment. Es war mir eine Ehre, mit diesem wunderbaren Team zusammenarbeiten zu dürfen!

Allen anderen Kollegen im Institut, besonders den Mitgliedern der AG Rasel, AG Ertmer/Klempt und AG Ospelkaus, sei an dieser Stelle für ihre Freundlichkeit und großzügige Hilfsbereitschaft gedankt, die ein einzigartiges Umfeld schaffen, in dem ich gerne gearbeitet habe. Ich durfte viele, wunderbare Menschen kennen lernen, denen ich für die gemeinsame Zeit sehr dankbar bin.

In Fragen zu Elektronik habe ich in Dr. Kai-Martin Knaak und Dr. Thijs Wendrich immer kompetente Ansprechpartner gehabt, die es nie überdrüssig waren, mir diese zu beantworten. Ich danke ihnen, dass sie sich für mich die Zeit genommen haben und mit ihren Entwicklungen das Arbeiten im Labor bereichert haben.

Einen herzlichen Dank möchte ich an das Sekretariat des Instituts aussprechen. Frau Göldner-Pauer, Frau Hünitzsch, Frau Faber, Frau Pfennig und Frau Koberstein leisten einen großen Beitrag zum reibungslosen Arbeitsablauf in unserem Haus und verstehen es mit ihrer Ruhe und Geduld wie kein Anderer, nervöse Doktoranden zu entschleunigen. Ich danke Ihnen, dass ich mich mit meinen organisatorischen Fragen und Anliegen immer an Sie wenden durfte und Sie mir stets weiterhelfen konnten!

Im gleichen Zuge möchte ich mich auch bei den Mitarbeitern des QUEST-Büros

für eine kompetente Anlaufstelle für unterschiedlichste Fragen bedanken: Frau Thiele-Bode, Herr Wanner und insbesondere Frau Ohlendorf, die mich im Rahmen meiner Promotion an der QUEST-Leibniz-Forschungsschule exzellent "gepampert" hat, wie sie selbst so schön sagt.

Ein großer Dank gilt auch der Feinmechanik-Werkstatt unseres Instituts. Fritz Witzlau leistet mit seinem Team eine großartige Arbeit beim Umsetzen unserer Planungen und Zeichnungen. Ganz besonders möchte ich Alexander Vocino für das Bearbeiten unseres SOC-Uhrenlaser-Prototypen danken, den ich immer mit kleinen Feinschliffen belästigen durfte und der sehr geduldig ein tolles Endprodukt geschaffen hat. Ebenso danke ich Matthias Scholz, der so freundlich war, meine laktosehaltigen H₂O-Bestellungen für unsere Arbeitsgruppen über sich ergehen zu lassen.

Dem Graduiertenkolleg 1729 der Leibniz Universität Hannover danke ich für die Möglichkeit, unsere Forschungsergebnisse auf der "2015 Joint Conference of the IEEE International Frequency Control Symposium & European Frequency and Time Forum" in Denver (USA) präsentieren zu können. Stellvertretend möchte ich mich bei Frau Zander für die Organisation dieser Dienstreise bedanken, die für mich eine wertvolle Erfahrung darstellt.

Für das Korrekturlesen dieser Doktorarbeit möchte ich mich ganz herzlich bei Steffen Rühmann, Dominika Fim, Klaus Zipfel, Nandan Jha, Steffen Sauer, Felix Kösel und Ernst Rasel bedanken. Ihre Verbesserungsvorschläge und Anmerkungen waren mir eine große Hilfe beim Erstellen der finalen Version.

Herrn Prof. Dr. Klemens Hammerer danke ich, dass er freundlicherweise den Vorsitz meiner Prüfungskommission übernommen hat.

All meinen Freunden, die mir eine große Stütze in der vergangenen Zeit waren, spreche ich einen herzlichen Dank aus. Ihr habt mir zugehört, Mut zu gesprochen und wart mir wertvolle Begleiter. Ich möchte Euch nicht missen!

Mein größter Dank gilt meinen Eltern, Waltraut und Dieter, die mir mein Studium ermöglicht haben und, seit ich denken kann, mir immer mit gutem Rat zur Seite standen. Ihr habt Euch mit mir gefreut, aber mich auch stets ertragen und wieder aufgerichtet, wenn Rückschläge mich geknickt haben. Dafür danke ich Euch über alles! Ich liebe Euch!

LIST OF PUBLICATIONS

- *Towards a Mg Lattice Clock: Observation of the 1S_0 - 3P_0 Transition and Determination of the Magic Wavelength*
A. P. Kulosa, D. Fim, K. H. Zipfel, S. Rühmann, S. Sauer, N. Jha, K. Gibble, W. Ertmer, E. M. Rasel, M. S. Safronova, U. I. Safronova, S. G. Porsev
Phys. Rev. Lett. **115**, 240801 (2015)
DOI: 10.1103/PhysRevLett.115.240801
- *First spectroscopy of the $^1S_0 \rightarrow ^3P_0$ transition in Lamb-Dicke confined magnesium atoms*
A. P. Kulosa, S. Rühmann, K. H. Zipfel, D. B. Fim, T. W. Wübbena, W. Ertmer and E. M. Rasel
Joint European Frequency and Time Forum & International Frequency Control Symposium (EFTF/IFC), 101-104 (2013)
DOI: 10.1109/EFTF-IFC.2013.6702235
- *Beating the density limit by continuously loading a dipole trap from millikelvin-hot magnesium atoms*
M. Riedmann, H. Kelkar, T. Wübbena, A. Pape, A. Kulosa, K. Zipfel, D. Fim, S. Rühmann, J. Friebe, W. Ertmer, and E. Rasel
Phys. Rev. A **86**, 043416 (2012)
DOI: 10.1103/PhysRevA.86.043416
- *An ultraviolet laser system for laser cooling and trapping of metastable magnesium*
A. P. Kulosa, J. Friebe, M. P. Riedmann, A. Pape, T. W. Wübbena, D. B. Fim, S. Rühmann, K. H. Zipfel, H. Kelkar, W. Ertmer, E. M. Rasel
arXiv:1201.3856v2 (2012)
- *The Space Optical Clocks Project: Development of high-performance transportable and breadboard optical clocks and advanced subsystems*
S. Schiller, A. Görlitz, A. Y. Nevsky, S. Alighanbari, S. Vasilyev, C. Abou-Jaoudeh, G. Mura, T. Franzen, U. Sterr, S. Falke, Ch. Lisdat, E.-M. Rasel,

A. Kulosa, S. Bize, J. Lodewyck, G. M. Tino, N. Poli, M. Schioppo, K. Bongs, Y. Singh, P. Gill, G. Barwood, Y. Ovchinnikov, J. Stuhler, W. Kaenders, C. Braxmaier, R. Holzwarth, A. Donati, S. Lecomte, D. Calonico, F. Levi
European Frequency and Time Forum (EFTF), 412-418 (2012)
DOI: 10.1109/EFTF.2012.6502414

- *Towards Neutral-atom Space Optical Clocks (SOC2): Development of high-performance transportable and breadboard optical clocks and advanced sub-systems*
S. Schiller, A. Görlitz, A. Y. Nevsky, S. Alighanbari, S. Vasilyev, C. Abou-Jaoudeh, G. Mura, T. Franzen, U. Sterr, S. Falke, Ch. Lisdat, E.-M. Rasel, A. Kulosa, S. Bize, J. Lodewyck, G. M. Tino, N. Poli, M. Schioppo, K. Bongs, Y. Singh, P. Gill, G. Barwood, Y. Ovchinnikov, J. Stuhler, W. Kaenders, C. Braxmaier, R. Holzwarth, A. Donati, S. Lecomte, D. Calonico, F. Levi
"Let's Embrace Space, Vol. II", European Commission Brussels, (2012)
DOI: 10.2769/31208
- *Aufbau eines Lasersystems zur Detektion und Manipulation von Atomen*
André Philipp Kulosa
Staatsexamensarbeit, Leibniz Universität Hannover (2009)

CURRICULUM VITAE

Personal data

Name: André Philipp Kulosa
Born: September 26, 1984 in Alfeld/Leine (Germany)
Nationality: German

Doctoral studies

08/2009 - today PhD student in the group of Prof. Dr. Ernst M. Rasel at the Institut für Quantenoptik of Leibniz Universität Hannover

University education

12/2008 - 06/2009 Staatsexamensarbeit in the group of Prof. Dr. Jan Arlt at the Institut für Quantenoptik of Leibniz Universität Hannover
10/2004 - 07/2009 Lehramt an Gymnasien (Staatsexamen), Mathematik und Physik at Leibniz Universität Hannover

Community service

10/2003 - 08/2004 Leineberglandklinik Alfeld/Leine

School education

08/1996 - 07/2003 Gymnasium Alfeld/Leine, Abitur 07/2003

